Wet steam drying: Microwave-assisted droplet evaporation in open-cell ceramic foams

von der Fakultät Maschinenwesen
der Technische Universität Dresden
zur Erlangung des akademischen Grades

Doktoringenieur (Dr.-Ing.)

vorgelegte Dissertation
von

M.Sc. Jesus Nain Camacho Hernandez

geboren am 9 Mai 1990 in Toluca, Mexiko

Tag der Einreichung: 04.07.2023

Tag der Verteidigung: 28.11.2023

Gutachter: Prof. Dr.-Ing. habil. Dr. h.c. Uwe Hampel

Prof. Dr.-Ing. John Jelonnek

Prof. Dr.-Ing. Markus Schubert

Vorsitzender der Promotionskommission: Prof. Dr. rer. nat. habil. Alexander Michaelis

Dresden, 2023

Acknowledgements

Abstract

In many energy and process engineering systems where fluids are processed, droplet-laden gas flows may occur. As droplets are often detrimental to the system's operation, they are required to be removed. According to the state-of-the-art, industrial droplet removal is achieved through a sequential arrangement of several separators followed by droplet collection and discharge. This results in a high-quality gas stream, yet at the expense of bulky and expensive systems that are difficult to retrofit to existing facilities. In addition, the multiple sequential separators produce high pressure drops, further increasing operating costs. Alternatively, a single droplet separation stage and in situ evaporation would provide compact solutions for facilities. However, compact engineering solutions for the removal of entrained droplets are difficult to achieve with conventional flow control and conduction heat transfer approaches such as Joule heating. Joule heating requires a well-defined and homogeneous electrical resistance to ensure uniform heating, which is technically challenging to apply in fine separators and thus compact removal devices are hence often costly and ineffective. Therefore, it becomes necessary to investigate alternative heating approaches to overcome these challenges, such as volumetric heating using microwaves.

The research conducted in this thesis aims to analyze the potential of a compact microwave solution approach for droplet removal. The compactness of the approach relies on a novel fine separator structure enhanced by microwave-heat transfer for efficient in-flow droplet evaporation. The investigation targets at fundamental studies of the combined effect of droplet flow filtering and heat transfer from numerical calculations and experimentation.

As novel fine separators, solid open-cell foams are a promising alternative for the separation of liquid droplets suspended in gas flows at comparably low pressure drops. Using susceptors, such as dielectric materials, for the skeleton and exposing them to microwaves is an efficient way for using them as heating elements. Silicon carbide (SiC) based open-cell foam samples were considered for the study as they are good susceptor materials. First, pore-scale fluid numerical simulations on representative foam models were used to obtain a deeper insight into the effects of pore size and pore density on the droplet retention time within foams. Numerical findings were reported considering the pressure gradient and the residence time distribution of droplets under different superficial flow velocities, droplet sizes, porosities and pore densities. Next, the temperature-dependent permittivity of SiC-based foam materials were determined by the cavity perturbation technique using a waveguide resonator at a microwave frequency of 2.45 GHz up to 200 °C. The permittivity was of particular interest as it is a crucial parameter for predicting and designing systems utilizing microwave heating. Along the permittivity measurements, electromagnetic wave propagation simulations were used to derive novel mixing relations describing the effective permittivity of foams while considering their skeletal morphology. The derived relations facilitate an efficient and reliable estimation of the effective permittivity of open-cell foams, producing good agreement to experimental data. Using the foams dielectric properties and the fluid characteristics of droplet-laden streams, a microwave applicator was designed to concentrate the electric field on the open-cell foams. The applicator was constructed for carrying experimental studies on droplet evaporation removal under different flow velocities, microwave power and different SiC-based foams. Measurements of

droplet size, velocity, number density and flux at the inlet and outlet streams of the applicator were performed using a 2D-phase Doppler interferometer.

Eventually, it was found from the experimental data analysis that the application of open-cell ceramic foams as filter medium reduced 99.9 % of the volumetric flow of droplets, while additional microwave exposure increases the reduction to 99.99 %. In addition, microwave-heated foams prevent droplet re-entrainment and structure-borne liquid accumulation within foams, thus avoiding water clogging and flooding. Hence, open-cell foams can be used as fine droplet separators as long as microwave heating may effectively evaporate accumulations of liquid. An important factor in designing future devices based on this microwave heating approach is the temperature, as it changes the arcing breakdown voltage of the gas, thus limiting the microwave input power and droplet flow velocity. Although more investigations are needed to develop an applicable and optimal product, the results presented in this thesis provide a first insight into the viability of using microwave heating and fine filtering as a compact solution for droplet removal.

Kurzfassung

In den meisten energie- und verfahrenstechnischen Anlagen, in denen Flüssigkeiten verarbeitet werden, können tropfenbeladene Gasströme auftreten. Da die Tröpfchen oft den Betrieb der Anlage negativ beeinträchtigen, müssen sie entfernt werden. Nach dem Stand der Technik wird die Tropfenabscheidung in der Industrie durch eine sequentielle Anordnung mehrerer Abscheider mit anschließender Tropfenabscheidung und -ableitung erreicht. Das Ergebnis ist ein qualitativ hochwertiger Gasstrom, allerdings auf Kosten großer und teurer Systeme, die hohe Druckverluste erzeugen und die Modernisierung bestehender Anlagen erschweren. Eine Alternative wäre eine einzige Tropfenabscheiderstufe und eine In-situ-Verdampfung, welche eine kompakte Lösung für Anlagen darstellen würde. Allerdings sind kompakte technische Lösungen zur Entfernung mitgeführter Tröpfchen schwer umzusetzen, wenn herkömmliche Strömungskontroll- und Beheizungskonzepte wie Joule-Heizung verwendet werden. Die Joule-Heizung erfordert einen genau definierten und homogenen elektrischen Widerstand, um eine gleichmäßige Erwärmung zu gewährleisten, was in Feinabscheidern eine technische Herausforderung darstellt, sodass kompakte Abscheideanlagen oft kostspielig und ineffektiv sind. Daher ist es notwendig, alternative Heizmethoden zu untersuchen, um diese Schwierigkeiten zu überwinden. Dabei stellt die volumetrische Erwärmung mittels Mikrowellen ein geeignetes Konzept dar.

Ziel dieser Arbeit war es, das Potenzial einer kompakten Mikrowellenlösung für die Tröpfchenentfernung zu analysieren. Die Kompaktheit des Ansatzes beruht auf neuartigen Feinabscheiderstrukturen, die durch Mikrowellen-Wärmeübertragung zu einer effizienten Tröpfchenverdampfung beitragen. Die Untersuchung zielt auf grundlegende Studien des Zusammenwirkens von Tropfenabscheidung und Wärmeübertragung anhand von numerischen Berechnungen und Experimenten ab.

Als neuartige Feinabscheider sind offenzellige Feststoffschäume eine vielversprechende Alternative für die Abscheidung von Flüssigkeitstropfen in Gasströmen bei vergleichsweise geringen Druckverlusten. Die Verwendung von Suszeptoren, wie z. B. dielektrischen Materialien, für das Gerüst und die Bestrahlung mit Mikrowellen ist ein effizienter Weg, um sie als Heizelemente zu nutzen. Für die Studie wurden offenzellige Schaumstoffproben auf Siliziumkarbidbasis (SiC) in Betracht gezogen, da diese gute Suszeptoren sind. Zunächst wurden numerische Strömungssimulationen auf Porenskala an repräsentativen Schaummodellen durchgeführt, um einen tieferen Einblick in die Auswirkungen von Porengröße und Porendichte auf die Tröpfchenverweilzeit in Schäumen zu erhalten. Die numerischen Ergebnisse wurden unter Berücksichtigung des Druckabfalls und der Verweilzeitverteilung von Tröpfchen bei unterschiedlichen Strömungsgeschwindigkeiten, Tröpfchengrößen, Porositäten und Porendichten dargestellt. Anschließend wurde die temperaturabhängige Dielektrizitätskonstante von Schäumen auf SiC-Basis mit Hilfe der Kavitätstörungsmethode unter Verwendung eines Hohlleiterresonators bei einer Mikrowellenfrequenz von 2,45 GHz bis zu 200 °C bestimmt. Die Permittivität ist von besonderem Interesse, da sie Aufschluss über die Dielektrizitätskonstante und den Verlustfaktor des Materials gibt, die für die Vorhersage und das Design von mikrowellenbeheizten Systemen wesentliche Parameter darstellen. Neben den Messungen der Permittivität wurden elektromagnetische Wellenausbreitungssimulationen verwendet, um

neue Mischungsbeziehungen abzuleiten, die die effektive Permittivität von Schäumen unter Berücksichtigung ihrer Skelettmorphologie beschreiben. Die abgeleiteten Beziehungen ermöglichen eine effiziente und zuverlässige Abschätzung der effektiven Permittivität von offenzelligen Schäumen und stimmen gut mit den experimentellen Daten überein. Mit Hilfe der dielektrischen Eigenschaften der Schäume und der Flüssigkeitseigenschaften der tröpfchenbeladenen Ströme wurde ein Mikrowellenapplikator entwickelt. Der Applikator ist so konzipiert, dass er das elektrische Feld auf die offenzelligen Schäume konzentriert. Der Applikator wurde konstruiert, um experimentelle Untersuchungen zur Tropfenverdampfung bei unterschiedlichen Strömungsgeschwindigkeiten, Mikrowellenleistungen und verschiedenen SiC-Schäumen durchzuführen. Mit einem 2D-Phasen-Doppler-Interferometer wurden Tröpfchengröße, -geschwindigkeit, -dichte und -fluss des Tröpfchenstroms am Einlass und Auslass des Applikators gemessen.

Die Analyse der experimentellen Daten ergab, dass die Anwendung offenzelliger Keramikschäume als Filtermedium den Volumenstrom der Tröpfchen um 99,9 % reduziert, während eine zusätzliche Mikrowelleneinwirkung die Reduzierung auf 99,99 % erhöht. Darüber hinaus verhindern mikrowellenerhitzte Schäume den Mitriss von Tröpfchen und die Ansammlung von Flüssigkeit in der Schaumstruktur. Daher können offenzellige Schäume als feine Tropfenabscheider eingesetzt werden, solange die Mikrowellenerwärmung Flüssigkeitsansammlungen effektiv verdampfen kann. Ein wichtiger Faktor bei der Entwicklung zukünftiger Geräte, die auf diesem Mikrowellenerwärmungsansatz basieren, ist die Temperatur, da sie die Lichtbogen-Durchbruchsspannung des Gas-Schaum-Mediums verändert und damit die Mikrowellen-Eingangsleistung und die Tröpfchengeschwindigkeit begrenzt. Obwohl weitere Untersuchungen erforderlich sind, um ein anwendbares und optimales Produkt zu entwickeln, geben die in dieser Arbeit vorgestellten Ergebnisse einen ersten Einblick in die Machbarkeit der Mikrowellenerwärmung zur Feinfilterung als kompakte Lösung zur Tropfenentfernung.

Table of contents

Nomenclature

Abbreviations

BSD	Back-Scattered electron Detector
EMA	Effective Medium Approximation
EM	Electromagnetic
FVM	Finite Volume Method
CFD	Computational Fluid Dynamics
DEM	Differential Effective Medium
ISM	Industrial, Scientific and Medical
LTNE	Local Thermal Non-Equilibrium
PDI	Phase Doppler Interferometer
MRCV	Mean Representative Cubic Volume
MSR	Moisture Separator Reheater
MUT	Material Under Test
OCF	Open-Cell Foams
PCA	Periodic Cubic enclosure Arrangement
PU	Polyurethane
RANS	Reynolds-Averaged Navier–Stokes
RH	Relative Humidity
RMSE	Root-Mean-Square Error
RLC	Resistance - Inductance - Capacitance
RNG	Renormalization Group
RTD	Residence Time Distribution
RSF	Relative Span Factor
SEM	Scanning Electron Microscopy
SiC	Silicon Carbide
SiSiC	Silicon-infiltrated Silicon Carbide
SBSiC	Silica-Bonded Silicon Carbide
SSiC	Pressureless Sintered Silicon Carbide
SS	Stainless Steel
VNA	Vector Network Analyzer
WAM	Weighted Arithmetic Mean
μCT	Micro-focus Computed Tomography

Latin Symbols

A	Prandtl number / -
C	Darcy coefficient / -
C_D	Drag coefficient / -
C_p	Heat capacity / $\mathrm{J \cdot K^{-1}}$
d	Diameter / m

D	Weibull distribution shape parameter / -	
D_P	Penetration depth / m	
d_{10}	Droplets arithmetic mean diameter / m	
$d_{\text{V}0.9}$	Accumulated d_d corresponding to 90 % of the total sprayed volume / m	
E	Electric field strength / $\text{V} \cdot \text{m}^{-1}$	
E_splash	Droplet impact energy normal to the surface (splashing energy) / J	
F	Force / $\text{kg} \cdot \text{m} \cdot \text{s}^{-1}$	
f	Rosance frequency / Hz	
g	Correlation complex-parameter / -	
H	Enthalpy / J	
h	Volumetric heat transfer coefficient / $\text{W} \cdot \text{m}^{-3} \cdot \text{K}^{-1}$	
h_0	Water accumulation film height / m	
j	Complex operator, i.e. $j = \sqrt{-1}$ / -	
K	Forchheimer coefficient / -	
k	Heat conductivity $\text{W} \cdot \text{m}^{-1} \cdot \text{K}^{-1}$	
k'	Normalized heat conductivity / -	
k_0	Wavenumber / m^{-1}	
κ_c	Von Kármán constant / -	
Kn	Knudsen number / -	
L	Length (model length between ports) / m	
L_PCA	Side length of the PCA / m	
L_c	Characteristic length / m	
L_cyl	Length of cylinder / m	
L_z	Foam height length / m	
M	Mass gas flow / $\text{kg} \cdot \text{s}^{-1}$	
M_d	Molar mass / $\text{kg} \cdot \text{mol}^{-1}$	
m	Mass / kg	
N	Total number of splashed droplets / -	
n	Refractive index / -	
Oh	Ohnesorge number / -	
P	Porosity / -	
P_w	Power density / $\text{W} \cdot \text{m}^{-2}$	
p	Pressure / $\text{N} \cdot \text{m}^{-2}$	
p_{dip}	Induced dipole moment / $\text{C} \cdot \text{m}$	
Q	Quality factor / -	
Q_MW	Thermal energy generated from microwave exposure / $\text{J} \cdot \text{s}^{-1}$	
Re	Reynolds number / -	
Re_KC	Kozeny-Carman Reynolds number / -	
RP_c	Standardized number of peaks at a surface / m^{-1}	
R_{pk}	Average height of the protruding peaks / m	
RS_m	Surface characteristic slope morphology / °	
R_z	Height profile / m	

S	Source mass term / kg ·
S_v	Specific surface area / $m^2 \cdot kg^{-1}$
St	Stokes number / -
SR	Susceptibility ratio / -
S_{11}	Reflected scattering parameter / -
S_{21}	Transmitted scattering parameter / -
t	Time / s
Tr_s	Threshold criteria value / -
U	Flow velocity / $m^3 \cdot s^{-1}$
U_{GS}	Superficial gas velocity / $m \cdot s^{-1}$
u	Velocity / $m \cdot s^{-1}$
V	Volume / m^3
We	Weber number / -
x	Inclusion size parameter / -
y^+	Wall-thickness parameter / -
z	Impedance / $V \cdot A^{-1}$

Greek Symbols

α	Polarizability / $C \cdot m^2 \cdot A^{-1}$
λ	Wavelength / m
κ	Dilatation viscosity / $N \cdot s \cdot m^{-2}$
δ	Volume fraction / -
δ_c	Dielectric dissipation factor / -
δ_{ij}	Kronecker delta / -
ε	Relative permittivity (dielectric) / -
ε_{st}	Relative permittivity at zero frequency / -
ε_∞	Relative permittivity at infinite frequency / -
ε'	Relative dielectric constant / -
ε''	Relative dielectric loss / -
ε_0	The permittivity of free space, i.e. $\varepsilon_0 = 8.84 x 10^{-12}$ / $F \cdot m^{-1}$
ε_w	Wiener permittivity bounds / -
ε_{HS}	Hashin-Shtrikman permittivity bounds / -
ϵ	Turbulent dissipation rate / $J \cdot s^{-1} \cdot m^{-3}$
μ	Relative permeability / -
μ_0	The permeability of free space, i.e. $\mu_0 = 1.25 x 10^{-6}$ / $H \cdot m^{-1}$
δ	Loss angle / -
θ	Contact angle / °
Φ	Volumetric flux / $m^3 \cdot m^{-2}$
τ	Mean residence time / s
τ	Relaxation time / s
$\bar{\tau}$	Viscous stress tensor / $N \cdot m^{-2}$

μ	Viscosity / $N \cdot s \cdot m^{-2}$
ν	Dynamic viscosity / $N \cdot s \cdot m^{-2}$
$\varepsilon_W^{\pm}$	Wiener bounds / -
ρ	Density / $kg \cdot m^{-3}$
σ	Surface tension / $N \cdot m^{-1}$
ω	Angular frequency / $rad \cdot s^{-1}$
Ψ	Weight parameter / -

Subscripts

b	Boiling
c	Ceramic
cell	Foam's cell
cyl	Cylinder
d	Droplet
e	Equivalent
eff	Effective
ext	Exterior
f	Fluid
g	Gas
incl	Inclusion
max	Maximum
min	Minimum
Re	Real part
Im	Imaginary part
P	Platonic skeleton
p	Particle
pore	Pore
s	Solid
sp	Sphere
st	Strut
l	Liquid
S	Splashing criteria
v	Vapor
vol	Volumetric
10	Arithmetic mean
V01	10 % of sprayed volume
V05	50 % of sprayed volume
V09	90 % of sprayed volume

Chapter 1

Introduction

1.1 Background and motivation

Steam is a popular choice for heating in various industries because of the large amount of energy it can store, which allows it to be used both as a source of electricity generation and as a heat source. Yet, steam has many practical applications beyond just producing electricity. Its use in drying and heating processes is particularly important in industrial settings, as it can be a very efficient and cost-effective means of transferring heat energy. In addition, steam is commonly used in cooking and food preparation, as well as in the cleaning and sterilizing equipment and surfaces. Its ability to drive turbines and other mechanical equipment also makes it a valuable power source for transportation and other applications [1]. However, efficiency and process safety are compromised in many industries if droplet-laden wet steam arises instead of dry steam. This condition is particularly relevant as turbulence-induced liquid shear stress in long pipe lengths causes some droplets to be carried away by the steam, thus becoming embedded in the same flow pattern as the vapor. This phenomenon is known as "entrainment" and emerges mainly through three mechanisms:

- Incomplete evaporation of liquid: during evaporation, when the vapor bubbles caused by evaporation rise and break the surface of the liquid water, they produce water ligaments, and as a result, a few droplets of water usually escape from the boilers. The water ligaments separate from the surface and break into smaller droplets carried away by the steam currents.

- Local condensation: despite being insulated, the steam carried by pipes constantly loses energy, which causes subcooled walls to form. On subcooled walls, where the steam reaches saturation temperature, the decrease in heat causes the steam to undergo condensation and form small droplets. The coalescence of the small droplets gives rise to larger droplets, which are eventually entrained by steam.

- Depressurization: Dynamic flash evaporators eject liquid into a section with low pressure. As the pressure decreases, the liquid starts to produce bubbles by nucleation. These bubbles burst and break the liquid jet, resulting in the atomization of many droplets. The droplets then decelerate and become small until they are all vaporized. However, if depressurization occurs, droplets do not evaporate entirely and are carried along with the flashing jet [2].

Droplet entrainment is a frequently occurring event and the risk of droplet entrainment increases in the presence of mechanical and chemical factors. Mechanical factors include those related to equipment and fluid loading rates. On the other hand, chemical factors are associated with the quality of the water used to generate the steam, as it may contain foaming agents as well as other contaminants [3]. Entrainment poses a significant risk to plants, as it can lead to harmful – sometimes catastrophically – effects (see Table 1.1), resulting in financial and safety repercussions.

Droplet entrainment is a concern for any process, but it is particularly problematic in the power and chemical industries. It can increase energy costs, degrade equipment performance, and raise environmental and health concerns. Exemplarily, this holds for the following applications:

- Chemical and petrochemical industry: In general, it is estimated that nearly 3 % of the total world energy demand and 50 % of the entire process industry energy demand is consumed by distillation [5]. In rectification and distillation columns, incomplete evaporation of the feed results in droplet entrainment. These droplets carry a significant number of high boilers to the upper parts of the column, drastically reducing the overall separation efficiency of the columns.

- Power industry: In the energy sector, turbines are commonly used to generate electricity. Erosion in the steam turbine's low-pressure stages is due to water droplets in the wet steam. This water, after condensation occurs, is deposited on the trailing edges of the diaphragm blades and then swept off from the trailing edges by the expanding steam. The relatively large, slow-moving water droplets strike the back of the moving blade tips leading to significant abrasion or chemical deposition at turbine blades and other structures [6,7], resulting in a decrease of over 5% of its generating capacity and increasing maintenance costs and safety hazards.

Table 1.1. Detrimental effects from droplet entrainment.

Effect	Description
Hydraulic water hammer	In thermodynamic working cycles, pockets of condensed steam can accumulate in pipe fittings. When the steam encounters the pockets, it condenses, and the space it occupies becomes a vacuum temporarily. The condensate walls surge towards the vacuum, colliding with each other and causing the pipe section to collapse. The over-pressurization can exceed 6.9 MPa, which may cause deformation, leakage and even pipe rupture [4].
Erosion and destruction	This impact of droplets gives rise to highly localized surface stress, which promotes the gradual breakdown of materials.
Deposits of water treatment chemicals	Water treatment chemicals in wet steam can degrade heat transfers by forming deposits in heat exchangers.
Contamination and product purity	In processes using steam injection, traces of treated water in the steam can contaminate process products. In addition, droplet emissions to the environment may sometimes exceed acceptable levels of contaminants.
Poor heat transfer	When water droplets are entrained in a steam flow to deliver a heat load to a device, they can cause a reduction in the amount of latent heat that is transported and transferred. Thus, reducing equipment efficiency.

Considering rising energy costs and safety concerns, droplet removal has become the primary approach to improve steam quality. Droplet removal from steam is a well-developed field of engineering. Mechanical separation often requires several stages to remove droplets of all sizes. In addition, droplet removal is typically carried out using bulky devices with complex geometries producing high-pressure drops to achieve optimal liquid separation and discharge. As the mechanical separation of droplets depends on the droplet size, droplet separators are divided into coarse and fine droplet separators. The main limitation of both types of separators

(but especially for the fine droplet separators) is the accumulation of liquid, which drastically reduces their performance.

Moreover, droplet removal from high-velocity steam involves a considerable waste of energy, as the sensible heat of the removed droplets is taken out of the system. For such a case, steam drying is an option for removing liquid from gases while saving energy. It comprises droplet capture and post-evaporation, providing a solution that increases energy efficiency and reduces the operation and maintenance costs of industrial processes. Post-evaporation's primary advantage is avoiding liquid accumulation, as the saturated liquid is evaporated rather than collected for drainage. Post-evaporation applied to steam drying is called reheating and is commonly performed, for example, in a moisture separator reheater (MSR). In addition, the amount of energy wasted by removing condensed liquid in the form of droplets from steam turbines depends on the mass flow and dryness factor of the wet steam. Steam turbines typically operate within a wide mass flow range of 1000 kg/h to 10000 kg/h. For example, the SST-900 Siemens turbine operates with steam at 165 bar and 565 °C [8]. The total energy per kilogram required to convert water into superheated steam and feed an SST-900 turbine is 3475.9 kJ/kg, and condensed liquid retains 1669.7 kJ/kg. For instance, removing droplets from steam that contains only 0.96 % dryness and flows at a rate of 1000 kg/h can result in the loss of up to 18.5 kW of power due to the heat load carried by the droplets. However, this loss can be mitigated by re-evaporation of the condensed liquid, which requires 9.9 kW. As a result, the net savings are as maximum of 8.6 kW.

The advantages offered by post-evaporation have motivated this work to reconsider technologies for fine droplet separators, including the study of their energy-intensive performance, to improve their design. In general, in this work, the following mechanisms have been studied:

1. Residence time of droplets in fine droplet separators.
2. Permittivity characterization of open-cell foams.
3. Application of microwaves for heating fine droplet separators.

The droplet residence time describes how much time a droplet has spent in a section of a volume, regardless of the main flow features. As the residence time increases, droplets receive more heat, and fewer overheating temperatures are required for post-evaporation. While steam wetness has been observed to be reduced by this approach (e.g. by using multi-pass recirculation [9]), its principle involves overheating once again. Another possible approach that may generate longer droplet residence time is to increase the number of changes in flow direction by placing several impedimental structures and increasing the path lengths. In this way, the persistence of moisture entrainment is enhanced and the number of droplets that are directly impacted and captured rises. Therefore, the design comprises high-residence times of droplets within fine droplet separators while producing post-evaporation of the retained liquid.

1.2 Aim of the work

This thesis provides a comprehensive study on hydrodynamics, microwave heating and droplet evaporation for a post-evaporation device based on a simple and easy-to-control compact flow contactor design. This compact solution is beneficial for revamping existing facilities that are currently difficult to set up with conventional flow control and heat transfer systems. A scheme of the innovative approach is shown in Figure 1.1, showing a common steam pipe with saturated steam in an annular flow regimen, characterized by a liquid film flowing on the channel wall and the entrained droplets at the core. Removal of the liquid film is easily achieved by steam traps (discharging condensate under varying pressures or loads). As the liquid film flow is removed, the flow regimen changes from annular to dispersed (or mist) flow. In the next stage, the droplets will reach the section of microwave drying, where droplets are captured and post-evaporated. Finally, it is obtained a flow with high steam quality.
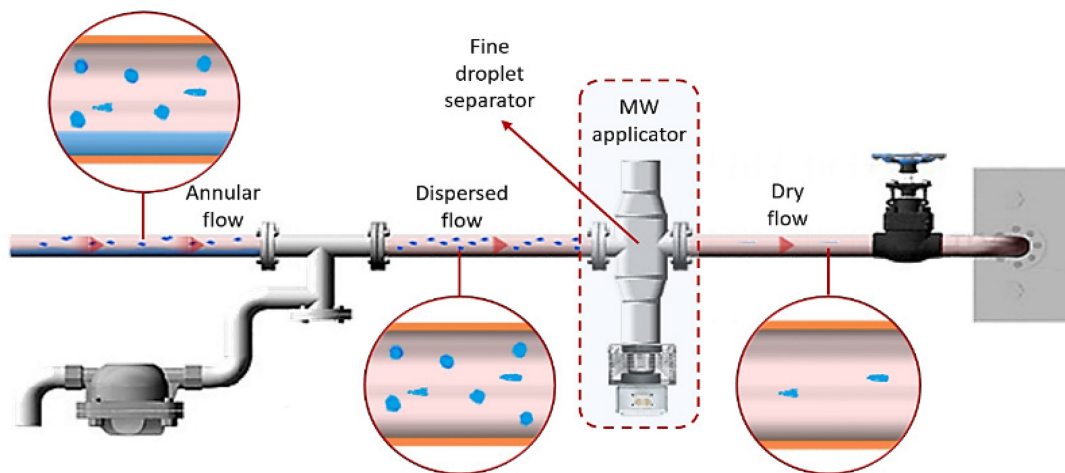
Figure 1.1. Schematic view of the microwave steam dryer for droplet post-evaporation.

1.3 Outline of the thesis

Chapter 2 summarizes the state-of-the-art of droplet removal and post-evaporation. Firstly, the droplet flow and its main hydrodynamic characteristics are presented. The droplet production mechanism and the factors influencing entrainment are also described. Droplet separation principles and technologies are discussed, considering the current state-of-the-art for steam lines. Moreover, open-cell foams are examined on their application as fine droplet separators by covering topics such as modeling of droplet capture and pressure drop. Then droplet re-evaporation is introduced as an alternative approach for improving steam quality, for which microwave heating is suggested. Finally, the state-of-the-art of microwave heating of dielectric materials is summarized and open questions are discussed to formulate the motivation for the objectives of this thesis.

Chapter 3: First, a representative SiC-based foam morphology and composition is presented. Next, tomography data of the foam are used to construct representative 3D models, serving for structural characterization and numerical modelling intended for computational fluid dynamics calculations. Calculations of single phase flow are performed, and the results are compared with pressure gradient measurements for model validation. Then, insight into droplets flowing

within foams is presented by using discrete droplet flow numerical calculations. Data are analyzed and reported describing the residence time of the droplets and the percentage of droplet removal (in terms of escaped droplets).

Chapter 4: The cavity perturbation technique is discussed and applied to obtain the effective permittivity of ceramic open-cell foams samples. Next, a brief literature survey on the mixing relations is provided and employed for the effective permittivity description of the foams.

Chapter 5: To complement the work on permittivity estimations of foams, this study also includes numerical calculations on various morphological models representing skeletal foam structures. A comparison of the numerical results is presented and is further used for deriving novel mixing relations. Lastly, comparisons of the derived mixing relations to common relations from literature are reported.

Chapter 6 gives an overview of the properties of foams that are used to estimate their heating and energy dissipation. Then, the procedure to numerically design a compact microwave applicator intended for droplet removal is disclosed. The main results from simulations are presented and discussed regarding the applicator design. Next, the concept of an experimental setup and the experimental procedure are presented. Results such as droplet size, velocity and volumetric flux of droplets are presented for the microwave applicator over a representative range of operating conditions. The trends observed in the data as well as the experimental limitations are discussed in this section. Lastly, the droplet removal efficiency of the microwave-heated foams approach employed in this work is reported.

Chapter 7 provides a summary of conclusions and recommendations for future work.

Chapter 2

State-of-the-art and theoretical
background

2.1 Droplet entrainment

Flow regimes are essentially descriptions of flow structure and phase distributions. The flow regime in pipes is determined by operational conditions and pipe design, e.g. flow rates, fluid densities and viscosities, tube diameter and inclination, as well as wall roughness. One way of predicting flow regimes is to employ a flow regime map. An example is shown in Figure 2.1.
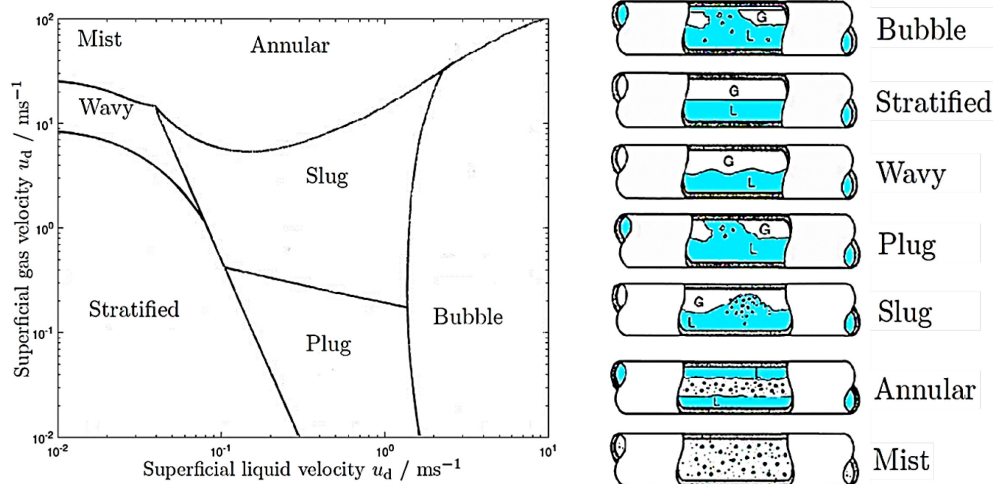

Figure 2.1. Flow regime map (left) and visual representation (right) in a 50 mm diameter horizontal pipe [10,11].

At low liquid velocities but high gas velocities, droplet entrainment starts. Droplet entrainment is a phenomenon in which droplets are carried along by gas or vapor with a terminal velocity very close to the continuous phase velocity ($u_d \approx U$). Droplet entrainment is found to occur in annular and mist flow regimes. In annular flows, an annulus-shaped liquid film flows on the wall of the pipe, and a gas flow occupies the remaining core space. As a result of momentum transfer from the gas phase to the liquid film, a portion of the liquid mass on the surface is dislodged from the film, producing ligaments (as depicted in Figure 2.2). Ligaments primarily break up into droplets due to the action of the inertial forces of the gas flow to the liquid surface tension. Liquid breakup is related to the Weber number We. We describes the ratio of inertial forces to surface tension forces and is defined as

$$We = \frac{\rho U^2 L_c}{\sigma_{lv}},\qquad(1)$$

where ρ is the density, U is the flow rate, L_c is the characteristic length and σ_{lv} the liquid-vapor surface tension. In case of ligament breakup, ρ is that of the liquid and L_c is related to the film thickness [12]. Instabilities in liquid films and ligaments that lead to breakup are assessed through a critical Weber number We_c, i.e. $We > We_c$. The droplet diameter produced during ligament breakup can be described as a function of a characteristic length (i.e. diameter of the ligaments) and the Ohnesorge number Oh. Oh describes the ratio of viscous forces to surface tension forces and is defined as

$$Oh = \frac{\mu}{\sqrt{\rho \sigma_{lv} L_c}}. \tag{2}$$

Larger droplets formed by primary breakup are subject to secondary atomization due to aerodynamic/shear instabilities generating smaller droplets, as shown in Figure 2.2. When the velocity of the liquid is low compared to that of the gas, or when a liquid film is removed from the annular flow due to liquid traps, mist flow can occur, which disperses droplets throughout the gas phase. The difficulty in removing droplets in the mist flow is the primary cause of the problems discussed in Chapter 1.

Figure 2.2. Droplet formation from wave instability of thin liquid films.

Entrainment of droplets is an effect of the motion of particles, which is determined by the equation of motion

$$\frac{\partial u_d}{\partial t} = \frac{F}{m_d}, \tag{3}$$

where u_d is the droplet velocity, m_d is the mass of the droplets and F is the sum of forces acting on the droplets. The mechanisms of acting forces in down-flow droplets, such as drag force, gravity force, Saffman force, Magnus force, and buoyancy force, have been extensively studied and reported in literature [13,14]. Additionally, general expressions using the Reynolds number Re have been developed [13] to predict further droplet lift. Re describes the ratio of inertial forces to viscous forces and is defined as

$$Re = \frac{\rho U L_c}{\mu}. \tag{4}$$

The Reynolds number of the droplets are obtained by using the droplet diameter d_d as the characteristic length, i.e. $L_c = d_d$. In general, it has been found that it is possible to reliably predict droplet entrainment conditions using only the most significant acting forces, such as the

drag force. It was also found that to entrain the droplets when $U_{\mathrm{g}} < 2.5\ \mathrm{ms}^{-1}$, the Reynolds number Re of the gas must generally be 1000 times larger than that of the liquid [13]. Another fundamental property of entrainment is the movement of the droplets following the gas streamlines. This characteristic makes separating droplets from the steam difficult as the droplets follow the same flow pattern.

2.2 Droplet separators

Typically, in steam facilities, steam valves are installed. Those valves are a type of automatic valve that filters out condensates. Problems begin when droplet carryover becomes excessively high and end-of-line steam traps cannot eliminate most droplets. In such cases, mechanical separation techniques coupled with reheating (droplet re-evaporation) may be employed to ensure the efficient removal of droplets. According to the state-of-the-art [15-20], the droplet separation mechanisms are inertial, direct, diffusional and gravitational deposition, as illustrated in Figure 2.3. Of all these separation principles, the gravitational deposition is the only one that does not require additional objects to induce contact with the droplets, as it is sufficient to provide a container of adequate length for the droplets to fall. For the other deposition mechanisms, structures with a high specific surface area are placed within the flow channel. As a result, the flow direction is modified (see streamlines in Figure 2.3). As the number of times the flow direction changes, droplet impacting and subsequent deposition becomes more frequent. Inertial deposition occurs for larger droplets that cannot follow the bent streamlines due to their inertia. Eventually, those collide with the walls and are drained off. Effective separation of smaller droplets requires separator structures with very high specific surface area, as such small droplets interact more via direct and diffusion impingement. However, the introduction of small structures that alter the flow direction so many times results in a modification of the flow regime, producing high-pressure drops.
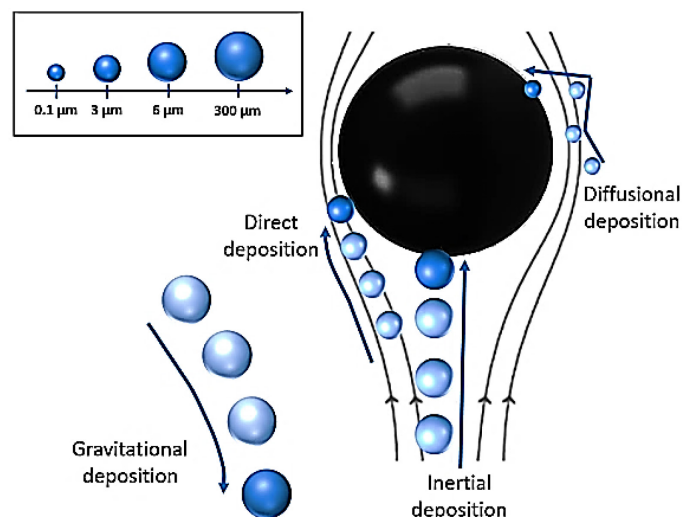

Figure 2.3. Illustration of droplet deposition mechanisms.

As the principle of separation differs with the droplet diameter, separation is commonly divided into primary and secondary. Primary separation (1st stage) uses the principle of changes in flow direction due to the density difference between liquid and gas. Equipment such as vanes, baffles, and centrifuges are examples of primary separation devices [19-24]. Secondary separation (2nd stage) focuses on capturing moisture in the form of mist ($d_d < 1$ µm) that is carried by large amounts of steam. This 2nd stage uses size inclusion, Brownian motion, and contact surfaces for impaction [23-25]. Effective separation of smaller droplets requires separator structures with very high specific surface area, as such small droplets interact more via diffusion than inertial impaction. This is achieved with separation screens, knit meshes and corrugated plates followed by conventional liquid recirculation or post-evaporation. An exemplified summary of separator devices is given in Table 2.1.

Table 2.1. Characteristics of droplet separators.

Stage	Separation mechanism	Separator example	Droplet size / µm	Pressure drop / Pa	Flow regimen
1st	Gravitational deposition	Cyclone	> 10	735 – 1000	Turbulent
1st	Inertial Interception	Vane	> 6	245 – 500	Transition / Laminar
2nd	Direct Interception	Wire/Knit mesh	> 0.3	24.5 – 500	Laminar
2nd	Diffusional deposition	Mist eliminators	< 0.3	300 – 600	Laminar

Droplet removal, also known as gas drying, is achieved by using separators of various designs, typically requiring bulky separators and recirculation lines, which can hardly be retrofitted into existing plants. For such, re-condensation of steam is likely, which again lowers the efficiency. Moreover, pure mechanical separation, especially of fine droplets, is problematic if a high steam quality is required. A crucial factor to consider in droplet removal is the Stokes number St, which indicates the ratio of inertial forces to viscous forces acting on a droplet in a gas flow. Fine droplets with low St ($St \ll 1$) follow the stream easily and are difficult to separate by impaction [26]. In addition, progressive wetting of small structures results in the formation of structure-borne liquid accumulations. The incapacity to effectively remove the liquid accumulations in fine separators results in droplet re-entrainment due to gas shear forces, thereby diminishing the quality of the produced steam. Usually, this is encountered by the sequential arrangement of several separators (see Figure 2.4), but this approach has the disadvantage of further increasing the pressure drop as well as requiring additional space for the separators.
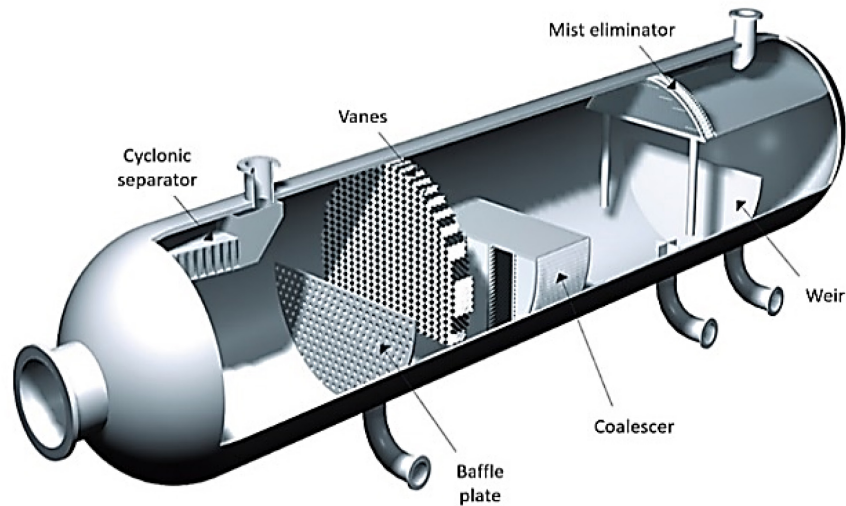
Figure 2.4. Industrial droplet separator [27].

The build-up of liquid films, which slowly drain out of the separator structure, occurs mainly in the so-called fine separators. Therefore, post-evaporation has the most significant effect on improving vapor quality in these fine separators.

2.3 Open-cell solid foams used as fine droplet separators

As for the challenges of finding a fine droplet separator to carry out in situ post-evaporation, open-cell solid foams are considered in this work instead of the usual separators, e.g. wire meshes and mist eliminators. However, open-cell foams have not been reported in the state-of-the-art as droplet separators (except for a recently published paper resulting from this research work [28]). With porosities ranging from 0.8 to 0.95, open-cell solid foams are heterogeneous mixtures consisting of a rigid thermally conductive network permeable to fluids. The solid network is known as the skeleton and is confined in a continuous medium, e.g. air or water. Structural elements of open-cell foams are pores, cells, struts, and joints, as illustrated in Figure 2.5. The cells are cavities interconnected through pores, which allow fluids to flow through the skeleton.
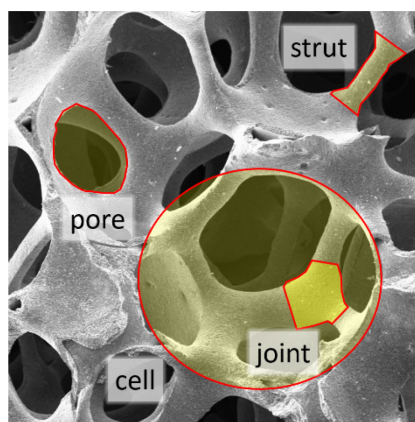

Figure 2.5. Internal structure of open-cell ceramic foams.

Depending on the solid material and manufacturing process, the cross-sectional shapes of the struts can be round, triangular-concave, or triangular-flat. The shape of the skeleton influences the formation of water films from droplet deposition. Round struts are more likely to form films of constant thickness, while for the other types of struts, this thickness is irregular to attain the minimum free energy on the surface [29]. The thickness of the water film that can form on the surface of the foam structural elements is a parameter that needs to be considered, as it determines the outcome of droplet impingement, i.e. deposition or splashing. In liquid deposition, the total mass of the droplet remains attached to the surface, while in liquid splashing, a rim of fluid sprays smaller droplets out of the surface as it expands. Such droplet-wall interactions are known to depend on the impact regime. The most common method of distinguishing between deposition and splashing is by a threshold criterion Tr_S, proposed by Stow [30] and confirmed by Mundo et al. [31]. Tr_S is obtained from studying the impact of droplets on dry rigid surfaces. The threshold expression in terms of We (the droplet splashes when $We > We_S$) is given as

$$We_S = Tr_S{}^{2/\alpha} Re^{2(1-\beta/\alpha)},$$ (5)

where α and β are empirically derived splashing parameters. The threshold criterion was later extended by Roisman et al. [32] to account for rough and porous ceramic surfaces. Also, Roisman's studies showed that wetting angle and surface material do not influence the splashing threshold. Instead, it depends on the initial inertial forces described in the We expression and the surface characteristics as

$$We_S = 10.5\left(R_{pk}/RS_m\right)^{-0.7},$$ (6)

where R_{pk} is the average height of the protruding peaks above the roughness core profile and RS_m is the mean width of the roughness profile element. On the other hand, when considering a wetted surface containing a liquid film of constant thickness, the splashing threshold criterion is commonly expressed [33,34] as

$$We_S = E_{splash}{}^2\left(\min\left(\frac{h_0}{d_d}, 1\right) + \frac{1}{\sqrt{Re}}\right),$$ (7)

where h_0 is the film height (for dry surfaces $h_0 = 0$) and E_{splash} is the droplet impact energy normal to the surface. Note that Equation 7 is reduced to Equation 5 for $h_0 = 0$ and $E_{splash} = Tr_S$, which coincides with the splashing parameters ($\alpha = 1$, $\beta = 5/4$) as suggested by Mundo et al. [31] for dry surfaces.

While it is possible to predict the outcome of droplet impingement on surfaces, estimating the droplet capture efficiency can be challenging due to the complicated morphologies of foam skeletons (see Figure 2.5). Numerical approaches, which can take the structure into account,

are important in understanding the impact of surface morphologies on droplet capture efficiency.

Two approaches are usually employed to represent an open-cell foam. The first uses idealized geometric models to represent the foam topology, such as skeletons composed of cells made of packed regular (e.g. Gibson–Ashby cells and tetrakaidecahedron) or irregular (e.g. prisms and Weaire-Phelean cell) polyhedrals [35-38]. The second approach considers the real foam structures reconstructed from tomographic scans. Both approaches have been used to create 3D foam models [28,39,40] and to investigate the characteristics of fluids within foams using numerical calculations. In general, simulations considering real foam structure produces better results than using idealized models. However, the accuracy of the results is contingent upon the spatial resolution used during the volume scan, as well as the refinement level of the simulation mesh. Achieving a high level of refinement comes at the cost of increased imaging and simulation expenses. Depending on the phenomenon to be studied, the necessary scale level is defined, which can be either molecular, microscopic, or macroscopic. Understanding the internal structure of foams at the microscopic scale necessitates the use of techniques that can resolve the individual features within the foams. However, these techniques are not arbitrary and are constrained by the characteristic dimensions of the fluid and foam continuum. Firstly, to consider a fluid as a continuum, the length scale of the fluid must be larger than the mean free path (ℓ) of its molecules. Flow through the skeleton pores must be much higher than the mean free path of these molecules. The Knudsen number Kn describes the ratio of the mean free path of the fluid molecules to a characteristic physical length scale of the system. In particular, Kn is used to determine whether the flow is in the free molecular regime ($Kn > 1$), or in the continuum regime ($Kn < 0.01$) [41]. Second, to consider a porous media as a continuum, the average intrinsic properties related to the geometrical skeleton morphology of a given volume subset of the porous domain should be equal to those obtained macroscopically. The concept of the representative element volume can be used to ensure that the results of a study are not influenced by the size of the domain being analyzed. The representative element volume is the minimum volume of a material that, when studied, will yield macroscopical results. The representative volume may have any geometric shape. That of a cube is known as the Mean Representative Cubic Volume element (MRCV). The MRCV defines the smallest representative rectangular cuboid within foams. As the cell and strut dimensions of the foams vary widely, it is often preferred to use the foam porosity P, which describes the ratio of the volume of voids to the total volume of the foam as the property for determining the MRCV [36,38]. In other words, by taking an element of volume equal to or greater than the MRCV, the flow hydrodynamics in porous media can be investigated, therefore allowing studying its droplet capture performance.

2.4 Hydrodynamics in porous media

2.4.1 Pressure gradient in porous media

Commonly, the open-cell pressure gradient ∇p is a macroscopic quantitative measure providing information on the foam porosity and fluid velocity. An empirical equation known as the Darcy-Forchheimer equation correlates ∇p to the flow velocity normal to the cross-sectional area of the flow u_{f}, the fluid viscosity μ_{f}, the fluid density ρ_{f} and two empirical parameters known as Darcy's permeability C and the Forchheimer coefficient K according to

$$\nabla p = u_{\text{f}} \frac{\mu_{\text{f}}}{K} + C \rho_{\text{f}} |u_{\text{f}}| u_{\text{f}} \,. \tag{8}$$

The Darcy-Forchheimer relation uses C and K, which are determined experimentally for a wide range of flow rates but are not associated with any characteristics of the porous media. The Ergun relation, on the other hand, does consider the porous media to be composed of spheres with specific pore diameter d_{pore} and porosity P, which are applied to the laminar drag term and an inertial term as

$$\frac{1}{K} = \alpha \frac{(1-P)^2}{P^3 d_{\text{pore}}^2} \text{ and } C = \frac{\beta}{K} \frac{d_{\text{pore}}}{(1-P)} \,. \tag{9}$$

The well-known Ergun equation suggests the values $\alpha = 150$ and $\beta = 1.75$. Although the Ergun relationship is very accurate for porous media composed of spherical particles, it does not provide accurate predictions of the overall ∇p in open-cell foams. Therefore, various other published relations have been proposed [42], in which the Ergun model is associated with a specific porous property (e.g. equivalent pore diameter) using equivalent and simpler geometrical elements such as spheres or cylinders.

2.4.2 Flow and turbulence modeling

Another approach is to determine hydrodynamic properties (e.g. pressure drop) by using Computational Fluid Dynamics (CFD) simulations [36,38,39]. This approach enables the handling of complex geometrical models derived from tomographic data, such as computed tomography or magnetic resonance imaging. The high accuracy of the 3D volume data obtained allows for the creation of realistic flow domains, while flow modeling is based on the Navier-Stokes equations of continuity and conservation of inertial momentum, which for single-phase compressible flows are given by

$$\frac{\partial \rho}{\partial t} + \nabla \cdot (\rho u) = S \,, \tag{10}$$

$$\frac{du}{dt} + u(\nabla \cdot u) = \frac{1}{\rho} (\nabla \cdot \bar{\tau} - \Delta p) + g \,, \tag{11}$$

where S is a source mass term, g the gravitational acceleration and $\bar{\tau}$ the summation of the viscous stress tensor and the turbulence stress tensor. For a Newtonian fluid, the stress tensor is a linear function of the rate of strain defined as

$$\bar{\tau} = \left[\mu \left(\frac{\partial u_i}{\partial x_j} + \frac{\partial u_j}{\partial x_i} \right) - \left(\frac{2}{3} \mu - \kappa \right) \delta_{ij} \left(\frac{\partial u_\kappa}{\partial x_\kappa} \right) \right], \tag{12}$$

where κ is the dilatation viscosity and δ_{ij} is the Kronecker delta. Turbulence is produced by increasing the flow velocity (high Reynolds number) inside the cells and the pores of the foams. The previous expression of the Reynolds number given in Equation 4 does not sufficiently describe the flow regime in porous media. The work of Carman et. al. [43] on flow covering both laminar and turbulent flow conditions in granular packed beds, served to define a more acceptable expression for describing flow regimes in porous media through a modified Kozeny-Carman Reynolds number Re_{KC} [44] defined as

$$Re_{KC} = \frac{\rho u_f}{(1 - P) S_v \mu_f}, \tag{13}$$

where S_v is the specific surface area. The macroscopic flow regimes, "viscous and inertia regimes" were considered to describe both the turbulent ($Re_1 > 100$) [44] and the laminar ($Re_1 < 100$) flow in the pores. The direct numerical calculation approach can describe turbulence. However, using these equations is computationally expensive. Thus, it is typically only used for problems with laminar flow due to the wide range of characteristic spatial and temporal scales [45]. In accordance with the current state-of-the-art, there are various alternative modeling approaches to compute turbulent flows, e.g. by using turbulence models based on the Reynolds averaging technique, which decomposes the mean $\bar{u}$ and fluctuating u' components of the velocity ($u = \bar{u} + u'$). The application of this approach to the Navier-Stokes mass and momentum equations results in the so-called Reynolds-averaged Navier-Stokes (RANS) equations, which in Cartesian and tensor form are expressed as

$$\frac{\partial u_i}{\partial t} + \frac{\partial}{\partial x_j}(u_i u_j) = -\frac{1}{\rho}\left[\frac{\partial p}{\partial x_i} + \frac{\partial}{\partial x_j}\left(\mu \left(\frac{\partial u_i}{\partial x_j} + \frac{\partial u_j}{\partial x_i} - \frac{2\delta_{ij}}{3}\frac{\partial u_i}{\partial x_i} \right) \right) + \frac{\partial}{\partial x_j}\left(-\rho \overline{u_1 u_j} \right) \right], \tag{14}$$

$$-\rho \overline{u_1 u_j} = \mu_t \left(\frac{\partial \overline{u_1}}{\partial x_j} + \frac{\partial \overline{u_j}}{\partial x_i} \right) - \frac{2\delta_{ij}}{3}\left(\frac{\rho u_i u_i}{2} \right) - \frac{2\delta_{ij}}{3}\mu_t \frac{\partial \overline{u_k}}{\partial x_k}, \tag{15}$$

where μ_t is the eddy (or turbulent) viscosity and $-\rho \overline{u_1 u_j}$ is the Reynolds stresses, and $-\rho \overline{u_1 u_j}$ serves as a coupling between the mean and fluctuation components of the velocity. It is important to note that no analytical relations exist between the mean velocity and the Reynolds stresses. To account for this, the Reynolds stresses equation is closed using an additional equation known as the Boussinesq hypothesis, given by Equation 15. This hypothesis postulates that the Reynolds stresses are proportional to the mean deformation rates. Several statistical models are based on this turbulent viscosity hypothesis, of which two-equation models (e.g. standard $k - \epsilon$, RNG $k - \epsilon$, Realizable $k - \epsilon$ and $k - \omega$) have been used in the literature for the numerical modeling of flow in porous media [36,38,46] and for the description

of droplet motion [47]. Such two-phase or multiphase flow model equations must be solved separately for each phase and be joined at the phase boundary, which might be moveable and deformable.

2.4.3 Droplet modeling for numerical calculations

For numerical calculations, droplets are handled as a dispersed flow. For that, it is crucial to consider the spectrum of length scales and time scales associated with the microscopic physics of the droplet motion, which has an important effect on the interaction between particles and turbulence [48]. The possible interactions are classified as one-, two- and four-way coupling.

In the one-way coupling, also known as sparse flow, the fluid affects the movement of the droplets through the drag force, but the droplets have a negligible effect on the turbulence. For this consideration, the droplet volume fraction must be less than $1x10^{-5}$. For the two-way coupling, also called dilute flow, the drag force and fluid-particle interactions are considered between the droplets and the turbulence energy dissipation rate. Finally, in the four-way coupling, known as dense flow, particle-particle collisions and drag forces are considered between the droplets and flow turbulence.

Currently, mathematical approaches are divided according to the integration of the continuous phase and interactions with the dispersed phase into the so-called Euler-Lagrange and Euler-Euler [48,49] approaches. In the Euler-Lagrange approach, the fluid phase is modeled as a continuum using the RANS equations. Meanwhile, the dispersed phase is solved separately by tracking a large number of individual particles. However, there are certain limitations to this approach. For instance, droplets must be much smaller than the computational mesh cells to be accurately tracked. Additionally, the droplet phase must occupy a low volume fraction, generally below 10 %, to avoid droplet-droplet collisions. Nonetheless, a high mass fraction ($\dot{m}_\mathrm{d} \geq \dot{m}_\mathrm{f}$) is quite acceptable [33]. In the Euler-Euler approach, all phases are treated as continuous phases by solving the momentum and continuity equations for each phase. The volume fraction of the dispersed phase determines the range of applicability of both approaches. The Euler-Lagrange approach offers additional capabilities from the Lagrangian framework, including the ability to track the individual history of droplets. Droplet information concerning the number of size-weighted droplets impacting a wall segment is crucial for assessing the efficiency of droplet capture and separation in open-cell foams, as suggested by the studies carried out for instance by Thiago et al. [36] and James et al. [50].

Simulations involving dispersed flow exhibit an increased computational burden and complicated spray models to predict the atomization of the liquid films [51]. In turn, water droplets are introduced into the computational domain at a prescribed distance from the test section, most commonly using an Eulerian-Lagrangian approach. This technique results in time-averaged droplet flow distributions, which can be transformed into spatial droplet distributions by dividing the number of droplets in each size range by the range's mean droplet velocity. The size range is mathematically represented by using a droplet size distribution such as the Rosin-Rammler or log-normal distribution, which according to Tarek et al. [52], affects the numerical performance of simulations. As the diameter of the droplets tends to zero, the Rosin-Rammler distribution becomes less reliable in representing the spray distribution of small droplets. This type of distribution is the most frequently used for droplet injection, especially if the effects of such small droplets are negligible.

The Rosin-Rammler distribution function is defined as

$$Y_{\mathrm{d}} = 1 - \exp\left[-\left(\frac{d_{\mathrm{d}}}{d_{\mathrm{n}}}\right)^{n_{\mathrm{d}}}\right], \qquad (16)$$

where Y_{d} is the mass fraction of a given d_{d}. d_{n} is a constant diameter size, and n_{d} is the distribution parameter. This distribution usually represents droplets with high sphericity Ψ_{d}. The sphericity of free-moving droplets depends on droplet size, surface tension and inertial forces, therefore, is described by the Weber number. Experiments have shown that droplets with smaller sizes moving at low speeds tend to be more spherical. Droplets with $\Psi_{\mathrm{d}} \approx 1$ are related to $We < 3.58$ [25]. While non-spherical droplets and ligaments [11] are difficult to measure experimentally, they can still be quantified by calculating the difference between the total droplet mass flux and the mass flux of spherical droplets. Modeling of droplet phase transitions such as droplet vaporization is predicted either by gradient diffusion for the evaporation rate (droplet temperature is above the dew point and below the boiling point) or by a boiling rate (droplet temperature reaches the boiling point).

Accordingly, the separation efficiency is defined by the droplet mass flow at the exit of the computational test section divided by the inlet droplet mass flow. The separation efficiency incorporates all phenomena affecting the droplet mass, including phase transitions and re-entrainment of droplets. Apart from the separation efficiency, the residence time distribution (RTD) of droplets is of importance to describe how much time a droplet of a specific size has spent in a section of a volume (test section) regardless of the main flow features (e.g. dead spaces, circulation, flow profile, impingement, re-entrainment). Experimentally, RTDs are obtained by adding tracers to the flow and measuring the number of tracers or their concentration crossing at the inlet and outlet of a test volume section [53]. RTDs can be obtained from computed spatial flow field distributions [54,55] and generally agree with experimental data [56]. Finally, RTDs are represented either by a residence time distribution function or graphically using a histogram plot.

2.5 Droplet re-evaporation

The costliest method for removing moisture from vapor is through reheating. Its major advantage is avoiding liquid accumulation, as the saturated liquid is evaporated rather than collected for drainage. As mentioned in Section 1.1, reheating is commonly performed in a moisture separator reheater (MSR). Commonly, the components of an MSR incorporate a steam inlet, a mechanical droplet separator, double-stage heat exchanger tubes and a steam outlet [57]. Mechanical droplet separators, such as corrugated plates, present a removal efficiency of at least 60 % (at $d_{\mathrm{d}} > 10\,\mu\mathrm{m}$, $u_{\mathrm{d}} > 4\,\mathrm{ms}^{-1}$) [58], therefore, often leave residual moisture content, which is the reason for using them as a pre-stage of reheating. The heated tubes are aimed to evaporate liquid but not entrained droplets. Due to the fast movement of droplets and their short residence time, efficient droplet evaporation necessitates excessively long ducts and high overheating for efficient evaporation of droplets. Another reason for using mechanical droplet separation before reheating is that it offers extra protection to the downstream components, e.g. preventing pipes from corrosion and erosion [59]. Simultaneous application of mechanical droplet separation and in situ evaporation would provide compact solutions for

facilities that overcome liquid accumulations in fine droplet separators. However, heating fine separators (i.e. mist eliminators and wire/knit meshes) is inefficient due to the high thermal resistance of their thin solid structures. In addition, Joule heating requires a well-defined and homogeneous electrical resistance to ensure uniform heating, which is technically challenging in fine separators. Alternatively, volumetric heating using microwaves could overcome these challenges.

2.6 Microwave heating

Microwaves cover the electromagnetic (EM) frequency spectrum between 300 MHz and 300 GHz, corresponding to wavelengths λ in the range of 1 m to 1 mm in vacuum. However, to avoid interferences with radio signals and telecommunications, the industrial, scientific and medical (ISM) applications are only allowed to operate on frequencies of 433 MHz, 915 MHz, 2.45 GHz, 5.8 GHz, or 24.15 GHz. Microwave heating is based on the principle that when radiation propagates through materials, part of its energy is dissipated and absorbed by the material. The resulting local absorbed power density P_w is proportional to the square of the electric field strength E as

$$P_w = 0.5\pi f \varepsilon_0 \varepsilon_r'' E^2 \,, \tag{17}$$

where ε_0 is the dielectric permittivity of free space and ε_r'' is the imaginary part of the relative effective permittivity. The relative permittivity ε_r ($\varepsilon_r = \varepsilon_r' - j\varepsilon_r''$) is a complex quantity in which the real part is known as the dielectric constant ε_r' that describes the ability of a dielectric material to store electric energy in an electric field. In addition, the dielectric constant also represents the wave impedance of the space occupied by the material. The imaginary part ε_r'' is the dielectric loss, which is a measure of the potential of a material to absorb microwave radiation and is related to the dielectric constant through the expression $\varepsilon'' = \varepsilon' \tan\delta$, where $\tan\delta$ is the loss tangent. In general, the dielectric characteristics depend on temperature, frequency of the EM radiation, and loss mechanisms of the material. These loss mechanisms can be broadly divided into polarization losses and conductive losses. [60]. These quantities can be used to estimate the penetration depth of microwaves into materials. The penetration depth D_P is the distance after which the microwave power drops by a factor of $1/e$ (i.e. $\sim 37\,\%$) of the input power and is given as

$$D_P = \frac{1}{\mathrm{Re}\left(j2\pi f \sqrt{\varepsilon_r \mu_r \varepsilon_0 \mu_0}\sqrt{1 - j\dfrac{\sigma}{2\pi f \varepsilon_r \varepsilon_0}}\right)} \,, \tag{18}$$

where μ_0 is the permeability of free space, μ_r is the relative permeability and σ is the electrical conductivity. Thus, the power a material absorbs is significantly influenced by the depth to which microwaves penetrate. Therefore, to apply volumetric heating by using microwaves, the penetration depth must be greater than the thickness of the material being heated. The dielectric loss may also allow a good dissipation of the microwaves and the spatial arrangement of the electric field may be strongly concentrated within the material.

Microwave technology has been studied and implemented over the past decades to intensify existing commercial processes due to its short start-up, selective heating, and the ability of microwaves to propagate through solid media [61]. The latter makes the use of microwave-transparent and insulating materials possible, providing operation in controlled mediums of different pressures, compositions, or phases, e.g. liquid-gas. Microwave heating systems typically consist of three main components: a microwave energy source, a load, a transmission line and an applicator. Extensive research in recent years on optimizing microwave applicators for efficient energy delivery has also reduced the capital cost of the technology and increased the safety of microwave systems. Microwave energy has the potential to be used as a process technology for droplet evaporation in steam lines. However, there are still many challenges that need to be overcome in order to make this a truly viable option. One of the main challenges is the development of new equipment on a larger scale that can be used for preparing and testing fine droplet separator materials using microwaves. Optimizing the design of microwave heating systems and effectively controlling the heating process can be achieved by accurately estimating the permittivity of ceramic foams. Accurate permittivity determination can lead to more efficient and effective microwave heating of ceramics with improved performance and better outcomes.

2.6.1 Dielectric properties of ceramic foams

Ceramic materials are often used in microwave heating applications because they are dielectric, meaning they are not good at conducting electricity. As a result, ceramics typically are classified as lossy insulators. Despite their low electrical conductivity, ceramics are highly susceptible to generating electrostatic fields, which is reflected in their high dielectric constant [60]. However, it is essential to carefully consider the trade-off between the high relative permittivity and the high losses when selecting materials for microwave heating. High losses can also lead to increased power consumption and reduced heating efficiency. The two main loss mechanisms for lossy insulators as ceramics are dipolar losses and conduction losses, with dipolar losses being the dominant one. When materials containing dipoles are exposed to an external electric field, the dipoles reorient themselves with the oscillating electric field. Consequently, forces such as inertia, elastic and molecular forces oppose this motion, causing an increase in friction and kinetic energy, thus rapidly increasing the temperature of materials [62]. The electromagnetic characteristics of any material including foams are described by the Maxwell equations, which in phasor form [63] are given as

$$\nabla \times \vec{E} = -j2\pi f \mu \vec{H} \,, \tag{19}$$

$$\nabla \times \vec{H} = j2\pi f \varepsilon \vec{E} + \sigma \vec{E} \,, \tag{20}$$

$$\nabla \cdot \varepsilon \vec{E} = \rho_{\text{charge}} \,, \tag{21}$$

$$\nabla \cdot \mu \vec{H} = 0 \,, \tag{22}$$

where ρ_{charge} is the charge density and E, H are the electric and magnetic fields, respectively. The solution of Maxwell's equations along with appropriate boundary conditions, produce the electric field distribution throughout the foam. This can then be used to calculate the power

dissipated in the foam and the resulting heating. However, it is hardly possible to fully describe the skeletons based on a spatial morphological function due to their complex morphologies and variability for each segment and composition. Thus, samples are often characterized experimentally through non-resonant methods, which are based on microwave propagation, or resonant methods, which are based on microwave resonance [64]. Although characterizing samples allows for accurately determining their dielectric properties, manufacturing numerous samples can pose a challenge when testing multiple parameters. This is especially the case for open-cell foams, which exhibit significant variability in materials and porosities. Instead, a practical approach that produces acceptable estimations of foams permittivity is to consider the condition where the structural elements (e.g. pores, cells, struts and joints) of open-cell foams are much smaller than the wavelength of an incident microwave radiation. When this condition is met, foams tend to behave as homogeneous or effective media and can therefore be macroscopically described using an effective permittivity ε_{eff}. This approach is known as the Effective Medium Approximation (EMA) [65].

2.6.2 Estimations of the effective permittivity of foams

The EMA approximation is a technique that is commonly used to model the properties of composite materials, such as foams, at the macroscopic scale. The EMA approach assumes that the composite material can be treated as a homogeneous medium with the inclusions distributed uniformly throughout a continuum medium. In high-porosity open-cell foams, the foam skeleton structure is considered as the inclusion, and the phase filling the voids acts as the continuum medium. This allows for calculating the effective permittivity and permeability of the composite material, which can then be used to solve electromagnetic problems at the macroscopic scale. However, it is important to note that the accuracy of the EMA approach depends on the assumption of homogeneity. If the composite material does not behave as a homogeneous medium, the estimates obtained using the EMA approach may not be accurate. As highlighted before, the foam structural elements must be much smaller than the radiation wavelength propagating through them. Some authors have studied and defined an inclusion size parameter X with which it is possible to define a threshold size at which the EMA approach is valid [66,67]. Yet, it has only been applied to microstructures given as spherical particles and not to complex structural elements such as those found in foams. Following the EMA approach, the corresponding ε_{eff} of foams depends on macroscopic properties such as the volume fraction and the bulk permittivity of host ($\delta_{host}, \varepsilon_{host}$) and inclusions ($\delta_{incl}, \varepsilon_{incl}$), as well as on the inclusion's microstructure. The microstructure of inclusion elements other than spheres and ellipsoids has proven to be very difficult to describe. There is no known way to do so analytically other than by using numerical calculations [68,69]. To determine the polarizability of microstructural elements, it is essential to calculate their electrostatic field, normalize it to that of a sphere, and then utilize the Clausius-Mossotti formula to relate it to the permittivity [68,70,71]. However, unlike the classical polarizability, which is a static concept, it can also be expressed as a complex number that involves a damping velocity response (or relaxation time) of the induced dipole moment in time-dependent fields [71]. This methodology of calculating the effective permittivity in terms of polarizability is accurate. However, significant numerical effort is required for geometrically-defined structural elements that remain constant across multiple samples. Meanwhile, for complex geometries such as foams, this approach is impractical. Instead, two approaches are followed for estimating ε_{eff} of complex foams:

1. Mixing relations such as those based on EMA approach [70,72] or probability distribution relations [73,74] are used to estimate the effective permittivity. Phenomenologically, the EMA relations consider inclusions of a mixture as spherical or ellipsoidal particles embedded in a continuous medium. Thus, reliable predictions from EMA relations can only be obtained if the real microstructure resembles features of the microstructure considered by the relation. As for the probability distribution relations, they can be separated into weighted means of bounds and general power means. Micromechanical bounds (e.g. Wiener bounds and Hashin–Shtrikman bounds, see Table 2.2 impose strict limitations on the effective properties of mixtures. Therefore, as permittivity is restricted, it is feasible to use relations based on volume-fraction-weighted means to fit the experimental data. The Wiener bounds restrict the maximum and minimum possible permittivity of an anisotropic mixture. In contrast, Hashin–Shtrikman bounds similarly restrict the maximum (inclusions with a series arrangement) and minimum (inclusions with a parallel arrangement) possible permittivity of isotropic mixtures. On the other hand, the power means do not require the prior calculation of any micromechanical bounds. Note that all probability distribution relations use a fitting parameter, which has no physical meaning, connecting it to the microstructure of the mixture [73], while EMA relations provide information on the microstructure. Moreover, it is interesting to point out that EMA and probability distribution relations can be used as cross-property relations [74], connecting the effective values of one property to those of another. Considering the thermal-electrical analogy of networks as an equivalent to open-cell foams, a relation can be used to estimate the effective permittivity or effective thermal conductivity. The EMA relations and probability distribution relations are depicted in Table 2.3.

Table 2.2. Micromechanical bounds of mixtures.

Bound name	Bound constraints	Expression
Wiener bounds $\varepsilon_B = \varepsilon_W$	Upper Wiener bound	$\varepsilon_W^+ = (1 - \delta_{incl})\varepsilon_{host} + \delta_{incl}\varepsilon_{incl}$
	Lower Wiener bound	$\varepsilon_W^- = \left(\dfrac{(1 - \delta_{incl})}{\varepsilon_{host}} + \dfrac{\delta_{incl}}{\varepsilon_{incl}}\right)^{-1}$
Hashin–Shtrikman bounds $\varepsilon_B = \varepsilon_{HS}$	Upper Wiener bound	$\varepsilon_{HS}^+ = (1 - \delta_{incl})\varepsilon_{host} + \delta_{incl}\varepsilon_{incl} - \dfrac{(1 - \delta_{incl})\delta_{incl}(\varepsilon_{host} - \varepsilon_{incl})^2}{3\varepsilon_{host} - (1 - \delta_{incl})(\varepsilon_{host} - \varepsilon_{incl})}$
	Lower Wiener bound	$\varepsilon_{HS}^+ = (1 - \delta_{incl})\varepsilon_{host} + \delta_{incl}\varepsilon_{incl} - \dfrac{(1 - \delta_{incl})\delta_{incl}(\varepsilon_{host} - \varepsilon_{incl})^2}{3\varepsilon_{incl} + \delta_{incl}(\varepsilon_{host} - \varepsilon_{incl})}$

Table 2.3. Mixture relations (b is the dimensional parameter, which is set as 3 for spherical inclusions).

Mixture relation	Expression
EMA relations	
Maxwell-Garnett (M-G) (Maxwell-type relation, non-symmetric)	$\dfrac{\varepsilon_{\text{eff}} - \varepsilon_{\text{host}}}{\varepsilon_{\text{eff}} + (b-1)\varepsilon_{\text{host}}} = \displaystyle\sum_{\text{incl}=1}^{N} \delta_{\text{incl}} \dfrac{\varepsilon_{\text{incl}} - \varepsilon_{\text{host}}}{\varepsilon_{\text{incl}} + (b-1)\varepsilon_{\text{host}}}$
Bruggeman-Landauer (B-L) (self-consistent relation, symmetric)	$\displaystyle\sum_{\text{incl}=1}^{N} \delta_{\text{incl}} \dfrac{\varepsilon_{\text{incl}} - \varepsilon_{\text{eff}}}{\varepsilon_{\text{incl}} + (b-1)\varepsilon_{\text{eff}}} = 0$
Differential Effective Medium (DEM) (Bruggeman relation. non-symmetric)	$\dfrac{\varepsilon_{\text{eff}} - \varepsilon_{\text{incl}}}{\varepsilon_{\text{host}} - \varepsilon_{\text{incl}}} \left(\dfrac{\varepsilon_{\text{host}}}{\varepsilon_{\text{eff}}}\right)^{\frac{1}{d}} = 1 - \delta_{\text{incl}}$
Exponential relation (Exp)	$\dfrac{\varepsilon_{\text{eff}}}{\varepsilon_{\text{host}}} = \exp(-\Psi_{\text{exp}}\delta_{\text{incl}})$
Pabst-Gregorová exponential relation (P-G)	$\dfrac{\varepsilon_{\text{eff}}}{\varepsilon_{\text{host}}} = \exp\left(-\Psi_{\text{P-G}}\dfrac{\delta_{\text{incl}}}{1 - \delta_{\text{incl}}}\right)$
Probability distribution relations	
Weighted arithmetic (Aritm) mean of upper and lower Wiener bounds	$\varepsilon_{\text{eff}} = (1 - \Psi_{\text{arth}})\varepsilon_{\text{B}}^{+} + \Psi_{\text{arth}}\varepsilon_{\text{B}}^{-}$
Weighted harmonic (Harm) mean of upper and lower Wiener bounds	$\varepsilon_{\text{eff}} = \left[\dfrac{(1 - \Psi_{\text{harm}})}{\varepsilon_{\text{B}}^{+}} + \dfrac{\Psi_{\text{harm}}}{\varepsilon_{\text{B}}^{-}}\right]^{-1}$
Weighted geometric (Geom) mean of upper and lower Wiener bounds	$\varepsilon_{\text{eff}} = \exp\left[(1 - \Psi_{\text{geom}})\ln(\varepsilon_{\text{B}}^{+}) + \Psi_{\text{geom}}\ln(\varepsilon_{\text{B}}^{-})\right]$
General sigmoidal (Sigm) mean of upper and lower Wiener bounds	$\varepsilon_{\text{eff}} = (1 - \Upsilon_{0,\text{N}})[(1 - \delta_{\text{incl}})(\varepsilon_{\text{B}}^{+})^{N} + \delta_{\text{incl}}(\varepsilon_{\text{B}}^{+})^{N}]^{1/N}$ $+ \Upsilon_{0,\text{N}}\{\exp[(1 - \delta_{\text{incl}})\ln(\varepsilon_{\text{B}}^{+}) + \delta_{\text{incl}}\ln(\varepsilon_{\text{B}}^{-})]\}$ where $\Upsilon_{0,\text{N}} = \begin{cases} 1 & \text{if } N = 0 \\ 0 & \text{otherwise} \end{cases}$
General power (Power) mean of the upper and lower Wiener bounds	$\varepsilon_{\text{eff}} = (1 - \Upsilon_{0,\text{n}})[(1 - \delta_{\text{incl}})(\varepsilon_{\text{host}})^{n} + \delta_{\text{incl}}(\varepsilon_{\text{incl}})^{n}]^{1/n}$ $+ \Upsilon_{0,\text{N}}\{\exp[(1 - \delta_{\text{incl}})\ln(\varepsilon_{\text{host}}) + \delta_{\text{incl}}\ln(\varepsilon_{\text{incl}})]\}$ where $\Upsilon_{0,\text{n}} = \begin{cases} 1 & \text{if } n = 0 \\ 0 & \text{otherwise} \end{cases}$

2. Numerical approaches involve a mesh or voxel representation of the microstructure of the foam's skeleton obtained from either reconstructed tomographic scans or computer-generated representative skeletons. The model structures are subsequently applied in a simulation environment to perform numerical electromagnetic calculations to obtain their corresponding effective permittivity [75]. Thus, the accuracy depends on the spatial resolution and the mesh refinement. This approach provides better estimates of the effective permittivity than by using relations, however, it is at the expense of imaging and simulation costs.

2.6.3 Microwave applicators

A microwave applicator is a structure, either hollow or filled with a dielectric material, that is enclosed by metal walls to contain microwaves within. The applicator receives the radiation from a microwave source and conducts them to a material under test (MUT) for heating. In simple terms, it can be expressed as a highly conducting waveguide that can be open at both ends (two-way traveling wave), or short-circuited at one (one-way traveling wave) or both ends (microwave resonant cavity). There are two main categories of microwave applicators based on the type of field they use to heat the MUT: electric and magnetic fields. The choice of the applicator will depend on the properties of the MUT and the desired heating characteristics. The heating of materials with high dielectric loss factors, low thermal conductivity, non-magnetic properties and high-water content, has been of significant interest in designing electric field applicators for food processing. These materials exhibit a higher probability of developing localized hot spots or thermal runaway [76]. A thermal runaway is an event that occurs when the loss factor increases with temperature, leading to the localized or complete destruction of the MUT. The selection and design of a microwave applicator thus depend on providing uniform power absorption and preferably placing the MUT at a location with a maximum electric field for effective volumetric heating. Efforts to minimize the unnecessary fields and to maximize the useful field in the MUT are a fundamental part of the design process. This is commonly achieved by using different arrangements of microwave transparent (total transmission, non-heated), reflective (good conductors, non-heated) and absorber (partial to total absorption, heated) materials. Formerly, the design of applicators was done by using some design guidelines, however, since the introduction of software capable of numerical calculations, the design has focused mainly on optimizing the geometry parameters of actual applicators [76-78].

Standing waves can occur in microwave applicators when the microwaves interferes with its own reflection. This occurs when microwaves encounter the inner walls of the applicator, which reflect some or all of the microwave back in the opposite direction. If the reflected wave interferes constructively with the incident wave, it can produce a standing wave pattern, which appears as a series of high and low amplitude areas within the applicator, known as nodes and antinodes, respectively. The distance between two adjacent nodes or antinodes is equal to half of the wavelength of the standing wave, and the dimensions of the applicator determine the number of these nodes and antinodes within the applicator. The dimensions of the microwave applicator restrict the maximum wavelength λ_{max} that can be accommodated within the applicator. Consequently, this restriction affects the propagation of transverse wave and determines the modes (i.e. the unique distribution of fields) that can exist within the applicator. Optimizing the dimensions of a microwave applicator is crucial to maximize its performance. The quality factor Q_{factor} describes the ratio of energy stored to energy losses per cycle of the electromagnetic field. Q_{factor} is useful in applicator designs as it can be measured for the empty (unloaded) applicator and with the MUT inside (loaded). The quality factor can be related to equivalent components of electrical circuits by using the parallel RLC (resistance R – inductance L – capacitance C) resonant circuit theory [79] as $Q_{\mathrm{factor}} = R\sqrt{L/C}$, allowing the analysis of impedance matching of microwave components to the applicator for maximum power transfer.

2.6.4 Efficiency comparison on heat generation using microwaves generators and other common heating technologies

Applying microwave technology for droplet removal within steam pipes would garner significant interest, particularly in the chemical, petrochemical, and pharmaceutical industries. However, concerns regarding energy efficiency and technical limitations persist. In contrast to heat pump-based systems, which can attain coefficients of performance (COP) exceeding 1 by relocating heat rather than generating it directly, microwave generators might not consistently present the most energy-efficient alternative. The COP represents the ratio of heating or cooling output to electrical energy input, indicating a system's efficiency. While Joule heating, also known as resistance heating, possesses a COP of 1 [80].

The factor contributing to the COP of microwaves to be typically less than 1 is the process of converting electricity into microwaves and subsequently transforming microwave energy into heat within materials. This conversion highly depends on the material susceptibility to effectively absorb microwaves and produce heat. In contrast, the generation of heat in Joule heating and heat pump systems is not reliant on the properties of the materials being heated. Additionally, it is important to note that concept of COP does not account for the heat transfer from the heat source to the material being heated. It should be noted that the overall efficiency of microwave heating can be significantly higher when compared to other heating systems, especially when heating materials with low thermal conductivity. This is primarily due to the possibility of volumetric heating, which can greatly reduce process time compared to conventional heating methods that rely on convective or contact heat transfer, where the efficiency depends on the thermal conductivity of the material. Therefore, a comprehensive analysis of the overall energy efficiency of the process is necessary to accurately evaluate and compare different heating systems.

While Joule heating can be applied to heat moisture separator reheaters, it is not an adequate solution for re-evaporating droplets from high-velocity flows. These systems still require lengthy ducts and substantial overheating for efficient evaporation of rapidly moving droplets (as discussed in section 2.5). Additionally, the possible use of Joule heating in state-of-the-art fine droplet separators, do also encounters challenges, such as non-uniform heating and eventual water clogging due to non-homogeneous electrical resistances.

In the context of heat pumps, there are currently no known examples of heat pumps integrated with effective internal fluidic heating for steam pipelines. However, instances of pipe dryers or dehumidifiers utilizing heat pumps can be found in other applications, such as for textile processing. These heat pump systems operate by circulating hot, dry air through the pipes to eliminate moisture in fabrics [81].

Although the microwave technology has advantages for enhancing droplet evaporation, it should be considered that microwaves exhibit limited conversion efficiency from electrical energy to microwaves. The conversion efficiency from electricity to microwaves can vary depending on the specific technology used. For instance, magnetrons have demonstrated conversion efficiencies ranging from 50 % to 65 % at 2.45 GHz [82, 83] and 78 % to 80% at 915 MHz [84, 85]. Alternatively, solid-state microwave sources can achieve even higher conversion efficiencies reaching up to 55 to 74 % [84, 86] at 2.45 GHz and 75% at 915 MHz

[84]. Note, that using a lower microwave frequency not only helps increase the penetration depth of the alternating current into the material, but it also can improve the energy conversion efficiency of the microwave generator. It is important to note that these values depend on several factors, including the specific design of the microwave source and the operating conditions. Despite these limitations, there are several compelling reasons to consider using microwave technologies, including the trend towards increased electrification of industrial processes and the potential for waste heat recovery.

A key consideration for the efficient use of waste heat recovery in microwave generators is the heat generated by the generators themselves. Both magnetrons and solid-state generators produce significant amounts of heat during operation, which must be dissipated by a cooling fluid. Low energy efficiencies in microwave generators are primarily due to energy losses in the form of heat. However, a potential solution to this issue is to repurpose the absorbed heat of the cooling fluid by using a heat exchanger. These heat exchangers can transfer the microwave waste heat to other process streams where heating is needed, resulting in lower energy consumption for the overall system. For instance, if the process involves a distillation column, the recovered waste heat can be applied to preheat the feed stream entering the column.

Given the current state-of-the-art equipment for droplet re-evaporation, it is worth noting that moisture separation reheaters can be subject to energy disadvantages due to their large size. Specifically, these disadvantages can result in significant heat losses and higher waste heat generation under certain process flows and temperatures. Therefore, a comprehensive analysis of the overall energetic efficiency of the process including the droplet separation stages is necessary to compare different heating methods, and to identify situations where microwave heating may offer superior energy efficiency.

Another critical aspect to consider is the feasibility of using microwave technology for large-scale applications, which require the delivery of power levels in the order of megawatts. In the case of magnetrons, the power output is typically limited by the size of the generator and the available cooling surface of the anode. For solid-state microwave generators, the power output is restricted by heat removal in the amplifier, leading to thermal runaway that can impact the integrity of the generator at high power levels.

One solution to overcome these challenges is the use of multiple microwave generators coupled to the applicator through separate ports. In addition, decreasing the microwave frequency is another potential solution to overcome the technical hurdles associated with upscaling microwave systems. Lower-frequency microwaves can provide higher energy efficiencies and output power. For instance, there are currently microwave generators on the market that can produce output power levels up to 100 kW at 915 MHz [87], demonstrating the feasibility of using microwave technology for large-scale processes.

2.7 Objectives of this thesis

As pointed out in the introduction, attempts to apply microwave heating for the re-evaporation of gas entrained droplets have not been previously reported. So, this study aims to investigate and provide knowledge and insight into this approach. This work comprises a novel application of microwave heating and the study of open-cell ceramic foams as fine droplet separators and

evaporators. Although this technology holds benefits for the energy and process engineering, there will be no progress until the right tools are available for development and production. For this purpose, the design of a microwave system is required, consisting of a microwave applicator for fine droplet separators. The aim of this thesis thus is directed toward the study and design of such a microwave system.

To the best of knowledge, this thesis is the first attempt to systematically study the possibilities of applying controlled microwave heating for droplet evaporation by using open-cell ceramic foams. For this purpose, the following objectives were derived and will be addressed in the remaining four chapters of this thesis:

1. To characterize the morphology of open-cell foams, to analyze the **residence time of entrained droplets** within them as well as to describe the **separation efficiency** in terms of the gas flow velocity.

2. To characterize and analyze the **dielectric properties** of different ceramic foams focusing on comparing the experiments and estimations through numerical calculations and mixing relations.

3. Based on the results of the first and second objectives, to **design** and **build** a microwave applicator along with the necessary components to heat ceramic foams.

4. To examine **volumetric flux, size distribution** and **velocity** of droplets in experiments using the microwave applicator.

Chapter 3

Hydraulic and morphological characterization of open-cell foams

As indicated in the previous chapter, open-cell foams are materials with the potential for use as fine droplet separators. However, their effectiveness to capture droplets has not been reported so far, not even that they have been used as droplet separators. The characterization and performance of various ceramic foams as droplet separators is evaluated in this chapter.

Parts of this chapter have been published in:

3.1 Foam analysis and mesh construction

SiSiC foam samples (blocks: $40 \times 40 \times 25$ mm) were manufactured by IKTS Fraunhofer (Dresden, Germany) using the replica method according to the Schwartzwalder process [88]. The samples featured nominal linear pore densities of 20 and 45 ppi (pores per inch). Notably, the pore density was provided as the mean ppi-value and is a measure of the interface density [89], which corresponds to the inverse of the mean chord length. Scanning Electron Microscopy (SEM) was utilized to visually examine the samples, revealing hollow struts of convex triangular cross-sectional shape (see Figure 3.1 left). These characteristics are the result of the manufacturing route applied for producing foams with porosities higher than 0.8 [90]. Additionally, crystalline structures were observed at the foam surface, indicating surface roughness.
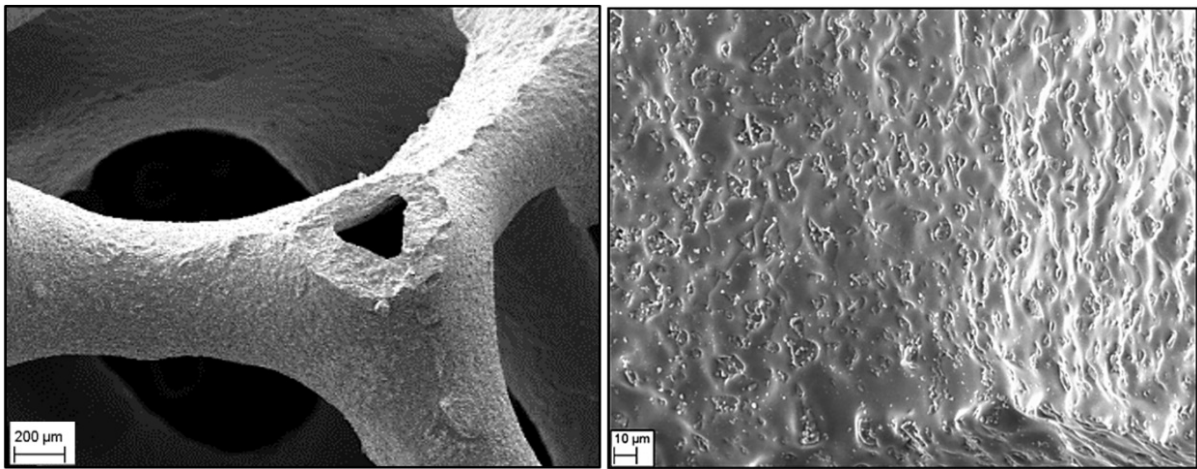
Figure 3.1. SEM images of a 20 ppi SiSiC open-cell foam, showing (left) convex triangular strut shape and (right) crystals attached to the skeleton surface.

An analysis of the samples using a Backscattered Electron Detector (BSD) revealed the elemental distribution on the surface as shown in Figure 3.2 and reported in Table 3.1. Based on the weight compound composition analysis, it was determined that most of the surface is composed of SiC, followed by elemental Si and a minor proportion of SiO_2. Moreover, measurements of the background scattering distribution indicate that the crystalline structures present on the surface of the foam are almost entirely composed of SiC crystalline polytypes.
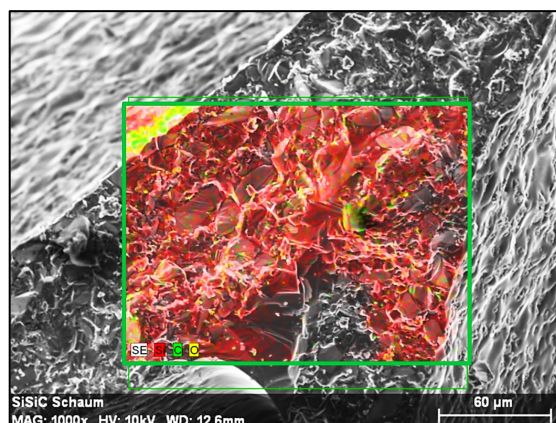
Figure 3.2. SEM backscattered electron image of the surface of a SiSiC open-cell foam, showing the elemental distribution represented by red, green and yellow colors for Si, C and O, respectively.

Table 3.1. Elemental weight composition of the surface of a SiSiC open-cell foam acquired from an SEM analysis using BSD and calculated compound composition.

Element	Weight composition / %	Uncertainty / %
C	20.14	4.66
O	1.80	0.66
Si	78.06	3.19
Compound	Calculated weight composition / %	Uncertainty / %
SiC	67.1	6.21
SiO_2	3.4	0.11
Si	29.5	3.60

The foam morphology of the samples (as illustrated in Figure 3.3) was extracted using X-ray microcomputed tomography (µCT) to create a series of 2D digital cross-sectional images, which were then assembled into stacks. Each stack had a size of $30 \times 45 \times 25$ mm^3 and a pixel resolution of 56 µm, corresponding to $536 \times 803 \times 446$ voxels. The cross-sectional images were composed of 16-bit greyscale value images, resulting from measurements of the attenuated photon intensity caused by the foam skeleton and air background, as exemplified in Figure 3.3.
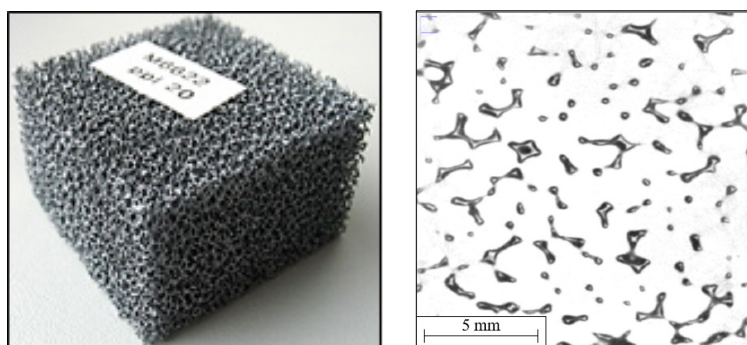
Figure 3.3. (left) a 20 ppi SiSiC open-cell foam sample and (right) corresponding 2D cross-sectional image.
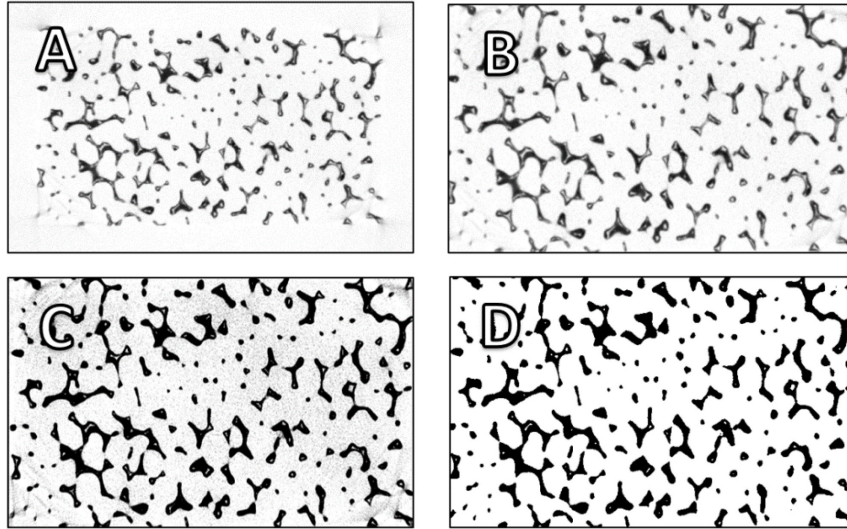
Figure 3.4. Image postprocessing: (A) 2D cross-sectional image obtained using μCT from a 20 ppi SiSiC sample, (B) image after contrast-stretched enhancement and borders cutting, (C) edge sharpened image, and (D) corrected images consisting of a set of binary values.

The images present undesirable defects and aberrations, such as double edges, streaking, beam hardening effects, and noise caused by X-ray scattering (see Figure 3.4A). Therefore, images were post-processed for correction using ImageJ and Matlab software. Initially, the images were cropped to the borders (see Figure 3.4B). Then, the image intensity was adjusted to enhance contrast through stretching, with a maximum of 25 % of the pixels allowed to become saturated. Stretching [91] works by applying a linear scaling function to the image pixel intensity bin-values $Pixel_{\text{Int}}$ based on the lowest and highest pixel bin-values, e.g. $0 - 65535$ bins for 16-bit images. Therefore, rounding a scaling function to the nearest integer is performed as

$$Pixel_{\text{Int,out}} = \left\lfloor \left(\frac{Pixel_{\text{Int,in}} - \min(Pixel_{\text{Int}})}{\max(Pixel_{\text{Int}}) - \min(Pixel_{\text{Int}})} \right)(2^{q_{bit}} - 1) + \frac{1}{2} \right\rfloor, \qquad (23)$$

where q_{bit} is the q-bit image number, i.e. $q_{\text{bit}} = 16$ for a 16-bit image. As a result, the contrast-stretched image effectively spreads out the information contained in the original histogram to the full 16-bit range while keeping graininess to a minimum. The image contrast enhancement was followed by edge sharpening using an unsharp mask filter [91], which uses Gaussian blur to produce an unsharpened image, which is then subtracted and rescaled from the original. The Gaussian blur standard deviation was set to a radius of 1 pixel (corresponding to a 5×5 kernel) for the standard deviation sigma decay to exp(-0.5) ~ 61 % and a weight strength of the high-pass filter of 0.60 (see Figure 3.4C). Those values were chosen to provide a sharpened output image dominated by the pixels inside the image with noise suppression. Finally, all images in the stack were segmented by converting them into binary using the Otsu's method [92] for obtaining a grey-value threshold level. All pixels with a value greater than or equal to the threshold were replaced by a value of 1 and the rest are set to 0, corresponding to the solid and void space, respectively. The result is a stack of 8-bit images (as shown in Figure 3.4D) corresponding to the morphology of the scanned samples.

As shown in Figure 3.1, the resulting images include hollow struts, which constitute a void volume that is not hydraulically accessible. Consequently, a particle analysis algorithm was utilized to remove them [91]. The particle analysis algorithm generates images corresponding to the strut cavities. The generated images corresponding to the strut cavities are then subtracted from the original images, to obtain 2D cross-sectional images that filled the strut cavities. With the images now composed exclusively of the closed ceramic skeleton and air, it was possible to determine the size distribution of pores, struts and cells, as well as the foam porosity. The size distributions of cells and struts were obtained by using the Local Thickness approach. It calculates the diameter of the maximal inscribed sphere that fits into struts and cells [88]. Then, the pore size distribution was calculated from the algorithm implemented by Rabbani et al. [89] for pore volume segmentation by using an automated watershed algorithm. The sample porosity P_{sample} was determined using the skeleton volume fraction also known as bone volume fraction [90]. This method is voxel-based and consists of counting the number of foreground voxels, corresponding to the foam's voids divided by the total number of voxels in the image. Results and graphical examples of the segmentation are shown in Table 3.2 and Figure 3.5.
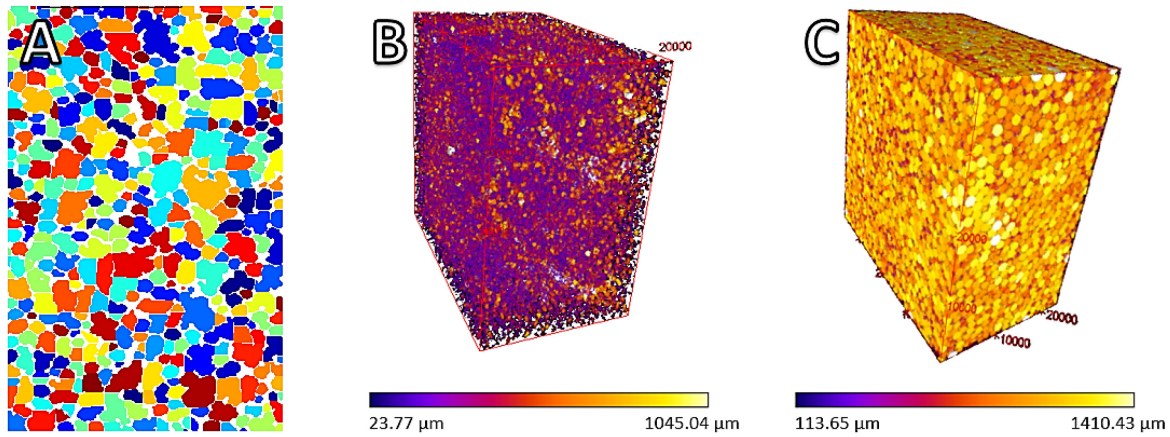
Figure 3.5. Image segmentation: image containing (A) 2D colored separated pores, (B) 3D colored-range diameter of segmented spheres inscribed into struts, (C) colored-range diameter of segmented spheres inscribed in cells.

Table 3.2. Structural foam properties.

Pore density / ppi	d_p / mm	d_{st} / mm	d_{cell} / mm	P_{manuf} / -	P_{sample} / -	P_{mesh} / -
20	1.62 ± 0.74	0.39 ± 0.15	2.39 ± 0.39	0.87	0.87	0.84
45	0.67 ± 0.29	0.17 ± 0.09	1.04 ± 0.14	0.85	0.86	0.82

In order to perform CFD simulations at computationally feasible costs, it is necessary first to define a representative elementary volume for the foam, such as the MRCV. To determine the minimum MRCV size, an intrinsic property related to the geometrical structure, such as the porosity, is computed over a range of increasing subvolumes. The MRCV is obtained once the local porosity matches the macroscopic porosity P_{sample}, and does no longer vary with increasing the element size. The sample was divided into three cuboidal segments to produce three MRCV with the same side length L_{MRCV} as shown in Figure 3.6. The results of the porosity of the segments as a function of the normalized cubic-volume length to the sphere cell

diameter $L_{\mathrm{MRCV}}/d_{\mathrm{cell}}$ are illustrated in Figure 3.6. In Figure 3.6 it is observed that at $L_{\mathrm{MRCV}}/d_{\mathrm{cell}} > 6$ the porosity stabilizes within ± 5 % of the P_{sample}, corresponding to L_{MRCV} values of 14.34 and 6.24 for the 20 and 45 ppi foams, respectively. Therefore, the domain size for the simulation was selected for L_{MRCV} as 15 and 10 mm for the 20 and 45 ppi foams, respectively. This working size allows simulations of the flow within foams at computationally feasible costs. Next, 3D surface meshes of the foams were generated by applying the marching cube algorithm [91], followed by surface simplification using discretized isosurfaces by utilizing an edge-collapse decimation algorithm [92], while preserving boundaries, topologies, and the normal directions of the mesh skeleton surface. The obtained meshes were then post-processed for smoothing by using a Laplacian operator [93] to close mesh open holes using flat-filling and flattering of sharpened spikes. Figure 3.7 shows a visual example of the resulting meshes. Finally, the porosities of the meshes P_{mesh} were determined and were found to be slightly smaller than P_{manuf} and P_{sample}, which is likely attributed to losses in the topological morphology due to filled strut cavities, mesh decimation and smoothing.
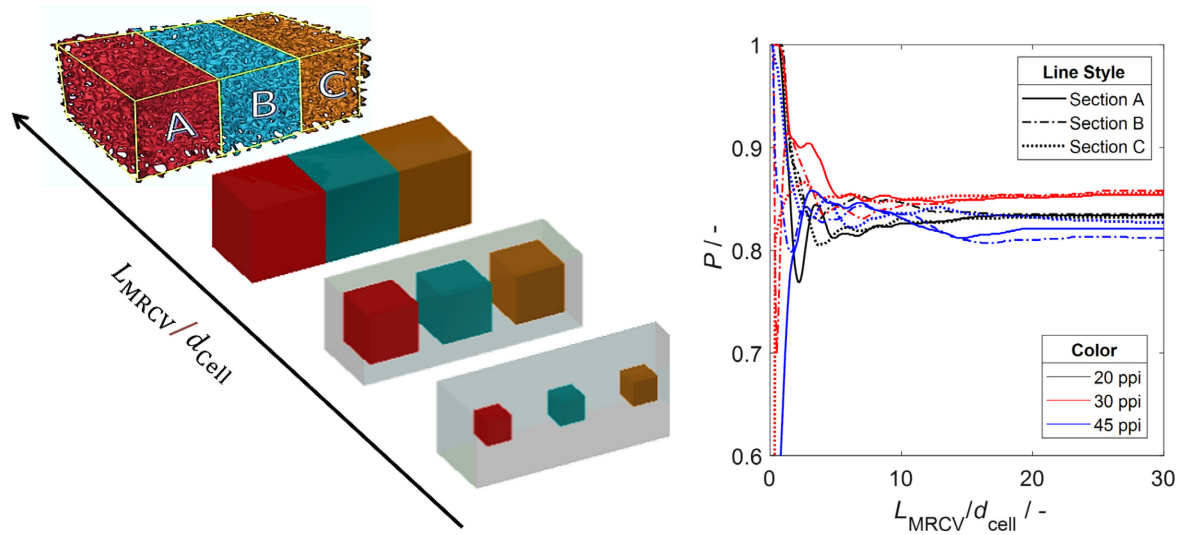
Figure 3.6. (left) cuboidal sections A, B and C for MRCV analysis and their (right) porosity variation over $L_{\mathrm{MRCV}}/d_{\mathrm{cell}}$.
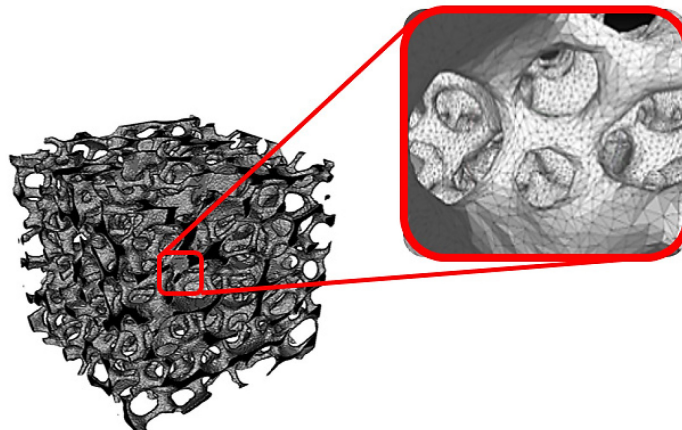
Figure 3.7. Illustration of the meshing result for a 45 ppi SiSiC foam reconstruction.

3.2 Numerical modeling of droplet flow within foams

One approach of modeling the flow within open-cell foam meshes is through numerical calculations utilizing the Reynolds-averaged Navier-Stokes (RANS) equations (Equations 14 and 15) in conjunction with turbulence models such as the different variations of $k - \epsilon$ and $k - \omega$. In this regard, Thiago et al. [94] investigated the airflow in open-cell metal foams using various turbulence models and found that $k - \epsilon$, RNG $k - \epsilon$ and $k - \omega$ models best matched experimental results. As a result, this work employed these models in the commercial CFD solver software Fluent [33]. The entrained droplets and the gas flow were modeled by applying the Euler-Lagrange approach with one-way coupling valid for dilute flows with a particle volume fraction well below 10^{-5} [48]. The droplets were injected to the simulation domain after the gas flow simulation had reached a steady state. Assumptions regarding droplet transport were made, such as that the temperature and gravity gradients can be neglected, due to their insignificant effect on the given simulation setup of droplets motion within foams. Droplets were considered to be perfectly spherical, non-wetting, surfactant-free and coalescence was neglected.

Modelling of droplet motion through the foam skeleton is done by treating them as particles with a velocity u_d which is strongly dependent on the drag force as

$$\frac{du_\mathrm{d}}{dt} = \left(\frac{18\mu}{\rho_\mathrm{p} d_\mathrm{p}^2} \frac{C_\mathrm{D} Re_\mathrm{d}}{24} \right) (u - u_\mathrm{d}), \tag{24}$$

where the drag coefficient C_D and the relative Reynolds number of a droplet Re_d are given by

$$C_\mathrm{D} = a_1 + \frac{a_2}{Re_\mathrm{d}} + \frac{a_3}{Re_\mathrm{d}^2}, \tag{25}$$

$$Re_\mathrm{d} = \frac{\rho d_\mathrm{d} |u_\mathrm{d} - u|}{\mu}. \tag{26}$$

For C_D evaluation a_1, a_2 and a_3 are empirical constants of smoothed spherical particles given by Morsi and Alexander [95]. For turbulent flows, the size of the droplets is comparable to the eddy size, hence, dispersion of droplets is tracked using the discrete Random Walk Model [96]. This model relies on a Gaussian probability distribution conformed of random numbers ζ with values between 0 and 1, and a fluctuation component of the fluid velocity u' based on the turbulent kinetic energy defined as

$$u' = \zeta \sqrt{2k/3}, \tag{27}$$

which is evaluated at each local point of the domain. Each droplet position x_d is updated in time as

$$\frac{dx_\mathrm{d}}{dt} = \bar{u} + u'. \tag{28}$$

The injection of droplets with a certain size distribution is performed using a Rosin-Rammler distribution function, where the mass fraction Y smaller than a given droplet diameter is given by

$$1 - Y = \exp\left[-\left(\frac{d_d}{d_n}\right)^{n_d}\right].$$ (29)

Here, d_n is the diameter size constant and n_d is the size distribution parameter. Preliminary simulations considered uniform droplets with diameters of 10 μm, 50 μm or 100 μm, followed by using a multi-size droplet injection, which is specified according to a Rosin-Rammler droplet size distribution given as $Y_d = 1 - \exp[-(d_d/61.269)^{4.017}]$. The distribution gives specific droplet mass fractions for each droplet size range (as summarized in Table 3.3), which approximate a Gaussian distribution of $R^2 = 0.9983$.

Table 3.3. Mass fractions for the multi-size droplet injection.

Diameter range / μm	10-15	15-25	25-40	40-55	55-70	70-85	85-95	95-100	Total
Mass fraction / %	0.35	2.34	13.80	28.73	36.64	15.71	2.11	0.29	100

Droplets at ambient temperature and pressure vaporize by diffusion. The molar vapor flux N_i that a droplet loses by diffusion is calculated as

$$N_i = K_c \Delta C,$$ (30)

$$K_c = \frac{\left(2 + 0.6 Re_d^{0.5} Sc^{\frac{1}{3}}\right) D_{vap}}{d_d},$$ (31)

where ΔC is the vapor concentration difference between the bulk gas and the droplet surface, K_c is the mass transfer coefficient, and D_{vap} is the diffusion coefficient of vapor. In Section 2.3, droplet-wall interactions such as deposition and splashing were introduced. These interactions occur as a result of the impaction regime, which can be characterized by We and R_{pk}/RS_m as $We = 10.5(R_{pk}/RS_m)^{-0.7}$ [32]. However, according to Gipperich [97], an alternative way of describing roughness is through their surface maximum height profile R_z and the standardized number of peaks at the surface RP_c, as illustrated in Figure 3.8. The roughness of porous ceramic surfaces range from $R_{z,min} = 0.0003$ cm to $R_{z,max} = 0.0113$ cm, corresponding to $RP_{c,max} = 152$ peaks/cm and $RP_{c,min} = 32$ peaks/cm, respectively.

For non-super hydrophobic and hydrophilic materials splashing occurs when $We > We_S$ (Equation 6) and can be calculated by using R_z and RP_c as

$$We_S = 41.885(R_z * RP_c)^{-0.7603}.$$ (32)
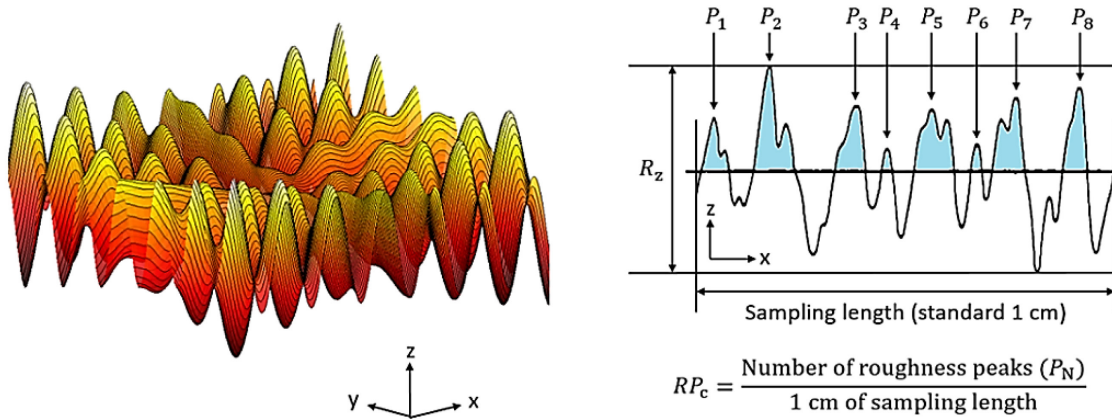
Figure 3.8. Schematic of roughness parameters of a surface.

Using the thresholds proposed by Gipperich [97], Mundo [31] and Roisman [32], a splashing/deposition threshold was produced to distinguish between splashing and deposition, which is illustrated in Figure 3.9.
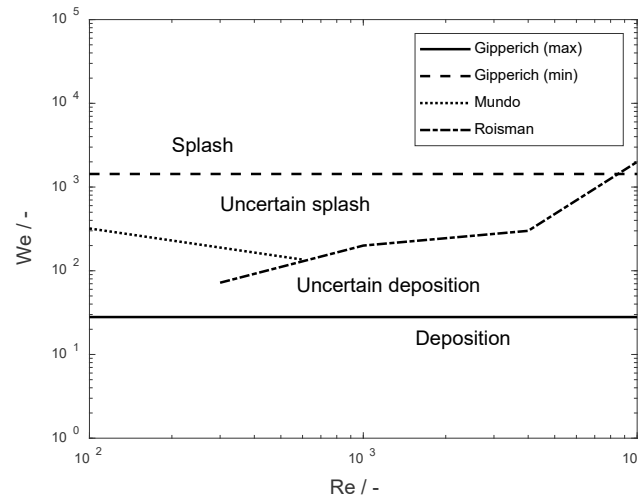
Figure 3.9. Splashing and deposition thresholds for porous ceramics.

Figure 3.9 shows that for We = 28 to 1433 the splashing or deposition is uncertain for porous ceramic foams, however, the uncertainties in calculations are treated as certain splashing or deposition. Additionally, re-entrainment of deposited droplets was also not considered for the calculations. A trap boundary condition for the discrete phase was used for deposition. Else, the splash of small droplets was implemented. The function to distinguish between deposition and splashing, in terms of the droplet impact energy E on a surface, is calculated as

$$E_{\text{splash}}^2 = \frac{We}{\left(min\left(\frac{h_0}{d_{\text{d}}}, 1\right) + \frac{1}{\sqrt{Re}}\right)}, \tag{33}$$

where h_0 is the film height, while for dry surfaces $h_0 = 0$. Then, when using the thresholds from

Figure 3.9 a corresponding quadratic minimum splashing energy E_s^2 can be calculated as

$$
\begin{aligned}
E_{\text{splash}}^2 &\geq 3329 & \text{for } Re \leq 600 \\
E_{\text{splash}}^2 &\geq 0.18Re^{1.5} + 22.6Re^{0.5} & \text{for } 600 < Re \leq 1000 \\
E_{\text{splash}}^2 &\geq 4.62Re^{1.5} - 624.36Re^{0.5} & \text{for } 1000 < Re \leq 4000 \\
E_{\text{splash}}^2 &\geq 2x10^{-5}Re^{2.5} - 3x10^{-15}Re^{1.5} + 9x10^{-12}Re^{0.5} & \text{for } Re > 4000
\end{aligned} \tag{34}
$$

This splashing criterion was defined in the commercial solver of Fluent [33] through user-defined functions. Deposition and splashing were implemented as follows.

1. Deposition: trapped boundary condition (i.e. $u_{2,n} = 0$) is achieved when the energy upon collision with a wall is lower than the minimum splashing energy $E^2 \leq E_{\text{splash}}^2$.

2. Splashing: splashing is given as $E^2 \geq E_{\text{splash}}^2$, which considers that a portion of the droplet remains on the wall, and subsequently, smaller droplets are re-entrained. To determine the mass fraction M/M_0 of a spray of smaller droplets (also termed splashed droplets), the correlation of O´Rourke [34] was used as

$$
\frac{M}{M_0} = \begin{cases} 1.8x10^{-4}\left(E_{\text{splash}}^2 - E_{\text{crit}}^2\right) & \text{for } E_{\text{crit}}^2 = 57.7^2 < E^2 < 7500 \\ 0.75 & \text{for } 7500 < E^2 \end{cases}, \tag{35}
$$

where M is the droplet mass re-entering the gas flow and M_0 is the initial mass of the droplet impacting on the surface. To determine the diameter distribution of the splashed droplets, a Weibull probability density function $f(d_d; D, 2))$ is used as

$$
f(d_d; D, 2) = 2\frac{d_d}{D^2}e^{-(d/D)^2}, \tag{36}
$$

where d_d is the random variable droplet diameter, D is known as the distribution shape parameter and 2 is the scale parameter fitted to data from Mundo [31]. The corresponding cumulative probability function and the maximum diameter of the splashed droplet in accordance with O'Rourke [34], are given by

$$
F(d_d; D, 2) = 1 - e^{-\left(\frac{d_d}{D}\right)^2}, \tag{37}
$$

$$
\frac{d_{d,\max}}{d_{d,\text{incident}}} = \left(\frac{57.7^2}{Es^2}, \frac{6.4}{We}, 0.06\right). \tag{38}
$$

The total number of ejected droplets that re-enter the gas flow can be calculated with the splashed mass fraction M as

$$
\frac{\rho\pi}{6}N_{\text{tot}}\sum_{n=1}^{N_{\text{parcels}}}(f_n d_n^3) = M, \tag{39}
$$

where N_{tot} is the total number of splashed drops and N_{parcels} is the number of splashed drops per parcel. The parcels are statistical representations of several droplets. Finally, to calculate the velocity, at which the smaller droplets are splashed off from a wall surface, a second Weibull function fitted to data of Mundo [98] was used according to

$$f\left(\frac{u_{\text{normal,splashed}}}{u_{\text{normal,incident}}}; \emptyset_{\text{v}}, b_{\text{v}}\right) = \frac{b_{\text{v}}}{\emptyset_{\text{v}}}\left(\frac{u_{\text{normal,splashed}}}{u_{\text{normal,incident}} \cdot \emptyset_{\text{v}}}\right)^{b_{\text{v}}-1} \cdot \text{e}^{\left(\frac{u_{\text{normal,splashed}}}{u_{\text{normal,incident}} \cdot \emptyset_{\text{v}}}\right)^{b_{\text{v}}}}, \quad (40)$$

$$\frac{u_{\text{normal,splashed}}}{u_{\text{tangential,splashed}}} = \tan(65.4 + 0.226\emptyset_{\text{l}}), \quad (41)$$

where b_{v} and $\emptyset_{\text{v}}$ are given as

$$b_{\text{v}} = \begin{cases} 2.1 & \text{if } \emptyset_{\text{l}} \leq 50^{\circ}, \\ 1.10 + 0.02\emptyset_{\text{l}} & \text{elsewhere}, \end{cases} \quad (42)$$

$$\emptyset_{\text{v}} = 0.158\text{e}^{0.017\emptyset_{\text{l}}}. \quad (43)$$

Next, the residence time distribution function $E(t)$ of the droplets can be obtained by tracking the concentration of droplets as they exit the foam over time $Conc(t)$ [99]. In this case, $E(t)\delta t$ is the fraction of droplets exiting the foam, which spent time between t and $t + \delta t$ inside the foam. The histogram of time at the outlet $E(t)$ is defined as

$$E(t) = \frac{Conc(t)}{\int_{t=0}^{\infty} Conc(t)dt}. \quad (44)$$

The average residence time τ_{i} of an ith droplet injection is calculated as

$$\tau_{\text{i}} = \frac{\int_0^{\infty} tConc(t)dt}{\int_0^{\infty} Conc(t)dt}. \quad (45)$$

The mean residence time τ is computed by averaging the residence time of N droplet injections as

$$\tau = \frac{\sum_{i=1}^{N} \tau_i}{N}. \quad (46)$$

The global residence time distribution $f_{\text{n}}(t)$ for multiple integers of individual sections is computed using the convolution of each RTD functions $E_{\text{n}}(t)$ according to

$$f_n(t) = E_1(t) \otimes E_2(t) \otimes \dots \otimes E_n(t) \,. \tag{47}$$

The function $f_2(t)$ reads for example as

$$f_2(t) = E_1(t) \otimes E_2(t) = \int_{-\infty}^{\infty} E_1(\theta) E_2(t - \theta)\, d\theta \,. \tag{48}$$

Convolution is the response of a system to any pulse. The response to a pulse acting at time θ is the shifted impulse response $E(t - \theta)$ multiplied by the area of the pulse.

3.3 CFD mesh and boundary conditions

Tetrahedral meshes were produced for the CFD simulations according to Section 3.2. The skewness ratios (min/max) were 0.014 and 0.021 for the 20 and 45 ppi foams, respectively. The boundary conditions needed for the simulations are summarized in Table 3.4 and illustrated in Figure 3.10. To avoid the influence of flow entrance and exit effects in the simulations, the mesh inlet and outlet surfaces were placed further upstream and downstream, respectively, with a distance equal to 70 % of the streamwise foam length.
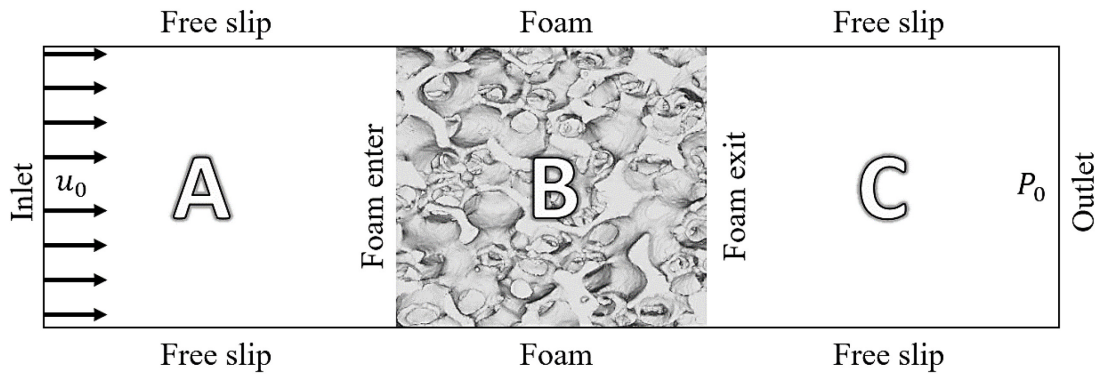
Figure 3.10. 2D schematic of the CFD domain: (A) inlet fluid surface, (B) foam domain, and (C) outlet fluid surface.

Table 3.4. Boundary conditions used for the CFD Simulations.

Interface	Zone	Velocity	Pressure
Inlet	A	$\dfrac{\partial u}{\partial x} = \dfrac{\partial u}{\partial y} = \dfrac{\partial u}{\partial z} = 0$	computed
Foam (no slip)	B	$\dfrac{\partial u}{\partial x} = \dfrac{\partial u}{\partial y} = \dfrac{\partial u}{\partial z} = 0$	$p = 0$
Walls (free slip)	A, B, and C	$\dfrac{\partial u}{\partial x} = \dfrac{\partial u}{\partial y} = u = 0$	$\dfrac{\partial p}{\partial x} = \dfrac{\partial p}{\partial y} = 0$
Outlet	C	$u\|_{(y^+=0)} = 0$	computed

3.4 Mesh size and turbulence model

As explained in Section 2.4.3, flow simulations within open-cell foams are best represented by using a RANS turbulence model for a wide range of Reynolds numbers. The two equations associated with the RNG $k - \epsilon$ turbulence model are derived from the renormalization group theory and according to Carvalho [94] the model has demonstrated good performance for modelling turbulence in open-cell foams. The RNG $k - \epsilon$ turbulence model reads

$$\frac{\partial}{\partial t}(\rho k) + \frac{\partial}{\partial x_i}(\rho k u_i) = \frac{\partial}{\partial x_i}\left(A_k \mu_{eff} \frac{\partial k}{\partial x_j}\right) + G_k + G_b + \rho\varepsilon - Y_M + S_k \,, \qquad (49)$$

$$\frac{\partial}{\partial t}(\rho\epsilon) + \frac{\partial}{\partial x_i}(\rho\epsilon u_i)$$
$$= \frac{\partial}{\partial x_i}\left(A_\epsilon \mu_{eff} \frac{\partial \epsilon}{\partial x_j}\right) + G_{1\epsilon}\frac{\epsilon}{k}(G_k + C_{3\epsilon}G_b) - G_{2\epsilon}\rho\frac{\epsilon^2}{k} - R_\epsilon + S_\epsilon \,, \qquad (50)$$

where the inverse turbulent Prandtl numbers A_ϵ and A_k are given by

$$\left|\frac{A - 1.3929}{1 - 1.3929}\right|^{0.6321} \left|\frac{A + 2.3929}{1 + 1.3929}\right|^{0.3679} = \frac{\mu_{mol}}{\mu_{eff}} \,, \qquad (51)$$

where A represent either A_ϵ and A_k, μ_{mol} is the molecular viscosity, and μ_{eff} is the eddy viscosity. In the present work, temperature gradients and gravity are neglected, i.e. $G_b = 0$. The turbulent viscosity is given by

$$\frac{d(\rho^2 k/\sqrt{\epsilon\mu})}{d(\hat{v})} = \frac{1.72\hat{v}}{\sqrt{(\hat{v})^3 - 1 + C_v}} \quad \text{with} \quad \hat{v} = \frac{\mu_{eff}}{\mu} \quad \text{and} \quad C_v \approx 100 \,. \qquad (52)$$

At higher Reynolds numbers, the production of turbulent kinetic energy G_k is given by

$$G_k = \mu_{eff}S^2 \,, \qquad (53)$$

while

$$G_k = \rho C_\mu S^2 \, k^2/\epsilon \qquad (54)$$

at low Reynolds numbers.

In the RNG $k - \epsilon$ turbulence model, R_ϵ is defined as

$$R_\epsilon = \frac{C_\mu \eta^3 (1 - \eta/\eta_0)\epsilon^2}{(1 + \beta \eta^3)}, \tag{55}$$

$$\eta = S\,k/\epsilon = k/\epsilon \sqrt{2 S_{ij} S_{ij}}, \tag{56}$$

for which the applied closure coefficients are summarized in Table 3.5.

Table 3.5. Closure coefficients.

Coefficient	Value	Coefficient	Value	Coefficient	Value
a_s	0.05	$G_{1\epsilon}$	1.42	β	0.012
C_μ	0.0845	$G_{2\epsilon}$	1.68		
C_v	100	η_0	4.38		

For a more appropriate simulation of the complex 3D flows, a standard wall function was chosen after comparing the experimental and simulated pressure drops, which is given as

$$U^* = \frac{1}{\kappa_c} \ln(y^* + B), \tag{57}$$

where B equals $\ln(9.793)$. $U^* = u^*/u_\tau$ is the normalized velocity in the near-wall region divided by the shear wall velocity u_τ. y^* equals $\rho u_\tau y/\mu$, in which y is the shortest distance to the wall, and κ_c is the von Kármán constant.

The governing equations outlined in Sections 2.4.3 and 3.5 were solved using a Finite Volume Method (FVM). The convergence criterion was set to 10^{-4} for the scaled residuals. A grid dependence study was conducted over the 45 ppi foam mesh, to ensure good accuracy of the numerical results. Table 3.6 summarize the result of the grid dependence study focused on varying the maximum cell length segment from 0.1 to 0.065 mm while keeping a constant minimum cell length segment of 10^{-3} mm. The convergence study was also performed for superficial gas velocities U_{GS} ranging from 0.1 to 1.0 $\mathrm{m \cdot s^{-1}}$ corresponding to Kozeny−Carman Reynolds numbers Re_{KC} (see Equation 13) ranging from 6.6 to 66.2, respectively. ∇p was used as an evaluation criterion. As a result, a maximum cell length segment of 0.08 mm, produces a percentage error below 8 % from the experimental value. The variation from 0.080 to 0.065 mm results in less than 3 % of the pressure gradient change. Grids with a cell length segment of 0.080 mm were used in subsequent simulations.

Table 3.6. Grid dependence study.

Max. cell length segment / mm	∇p / $\mathrm{Pa \cdot m^{-1}}$		
	$U_{GS} = 0.1\ \mathrm{m \cdot s^{-1}}$	$U_{GS} = 0.5\ \mathrm{m \cdot s^{-1}}$	$U_{GS} = 1.0\ \mathrm{m \cdot s^{-1}}$
0.1	146.8	1061	3000
0.09	141.8	1067	3036
0.08	142.5	1082	3087
0.07	143.5	1108	3187

0.065	143.7	1107	3164
Experimental	142.7	1136	3339

The effect of the turbulence model on ∇p was also tested for the 45 ppi foam and compared with their experimental counterparts. Results are reported in Table 3.7. The experimental determination of ∇p was accomplished with SiSiC open-cell foams of 20 and 45 ppi with sample lengths of 100 mm. The inlet superficial gas velocity varied between 0.1 and 1.7 $\text{m} \cdot \text{s}^{-1}$. All experimental ∇p measurements were carried out at ambient temperatures. As a result of this study, the RNG k$-\epsilon$ model with standard wall functions and swirl modification provided the best agreements with the experimental data, therefore, it was chosen for the simulations.

Table 3.7. Pressure gradient for 45 ppi foam under selected turbulence models ($U_{\text{GS}} = 1.7 \text{ m} \cdot \text{s}^{-1}$).

Turbulence model	∇p / Pa $\cdot$ m^{-1}
$k - \epsilon$	7977
RNG $k - \epsilon$, standard wall functions and swirl modification	7900
RNG $k - \epsilon$, enhanced wall functions	7431
Experimental	7800

3.5 Pressure gradient estimation

For comparison purposes, ∇p was modeled using a modification of the Ergun equation derived for open-cell foams. The original Ergun equation corresponds to Equation 10. In this modification, the sphere particle diameter, which is used in the original Ergun equation, is replaced with the inverse specific surface area ($1/S_{\text{v}}$) of the foam. S_{v} was calculated from the mesh, resulting in values of 2000 and 1004 m^2/m^3 for the 20 and 45 ppi foams, respectively. As a result, the modified Ergun equation ($R^2 = 0.9957$ and RMSE $= 17.12$) for SiSiC foams is

$$\nabla p = 559.6 \frac{(1-P)^2 S_{\text{v}}^2 \mu_{\text{f}}}{P^3} u_{\text{f}} + 2.5 \frac{(1-P)S_{\text{v}}\rho_{\text{f}}}{P^3} |u_{\text{f}}|u_{\text{f}}. \tag{58}$$

∇p calculated using the modified Ergun equation is compared with the experimental data from Figure 3.11 and with additional data from 30 ppi SiSiC foam experiments. ∇p is shown as a function of Re_{KC}. The model fit is generally excellent. It only tends to overestimate the predicted ∇p at bigger pore sizes. This is related to the determined dimensionless parameters α and β from Equation 9, which should not have the constant values $\alpha = 559.6$ and $\beta = 2.5$. Instead, these parameters should be functions of the foam geometry, which changes with the porosity.
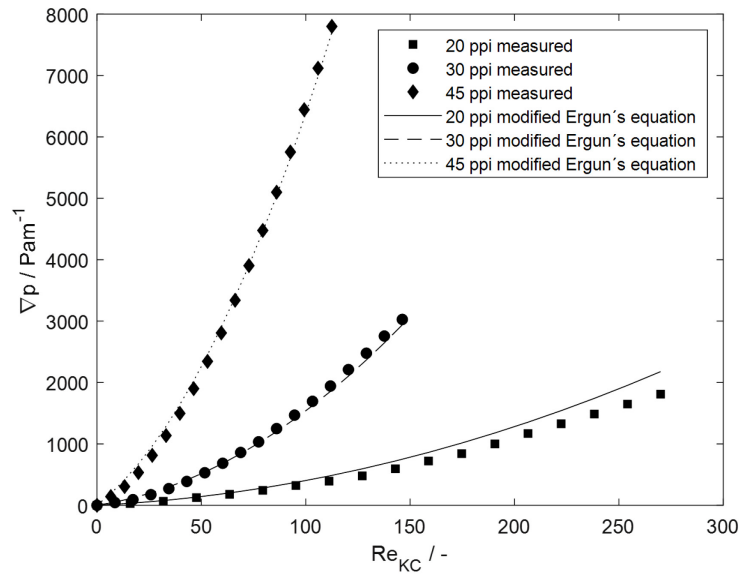
Figure 3.11. Comparison between predicted pressure gradient from the modified Ergun equation and experimental values.

The CFD calculations were also compared against literature models for open-cell foams, e.g. Lacroix model and Du Plessis model [42], the modified Ergun's model from Equation 58, and the experimental ∇p data from Figure 3.12. The calculated CFD pressure gradient was shown to provide better agreement with experimental data compared to literature models. This seems to be related to the fact that the simulations consider the real foam structure instead of idealized elements conforming foam's skeletons.
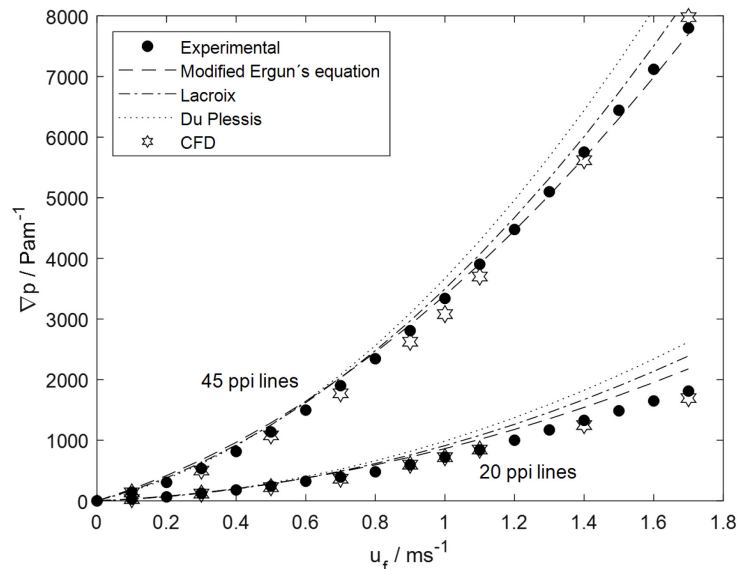
Figure 3.12. Comparison of correlated, experimental, and simulated (CFD) pressure gradient values for 20 and 45 ppi foams.

3.6 Effects of pore density and gas velocity on RTD

Droplet RTD curves were obtained by accounting for both the injected droplets and those exiting the foam. The RTDs were smoothed using weighted adjacent averaging and then fitted with a modified Dagum distribution of five fitting parameters (k, α, β, γ, and ζ) according to

$$E(t)(k, \alpha, \beta, \gamma, \zeta) = \frac{\alpha k((t - \gamma)/\beta)^{\alpha\zeta - 1}}{\beta(1 + ((t - \gamma)/\beta)^\alpha)^{k+1}}. \tag{59}$$

Droplet RTDs are shown in Figures 3.13, 3.14 and 3.15, and the parameters of the fitted Dagum distribution are summarized in Table 3.8. As shown in Figures 3.13, droplets with smaller inertia are easily carried with the fluid. They have fewer interactions with the foam skeleton than bigger droplets, particularly at low superficial gas velocities. Also, the larger the droplets, the longer they remain within the foam (see Figures 3.14 and 3.15,). In addition to droplet size reduction by splashing, it should be noted that droplets are continuously reduced by diffusion evaporation, which allows faster passage through the foams.
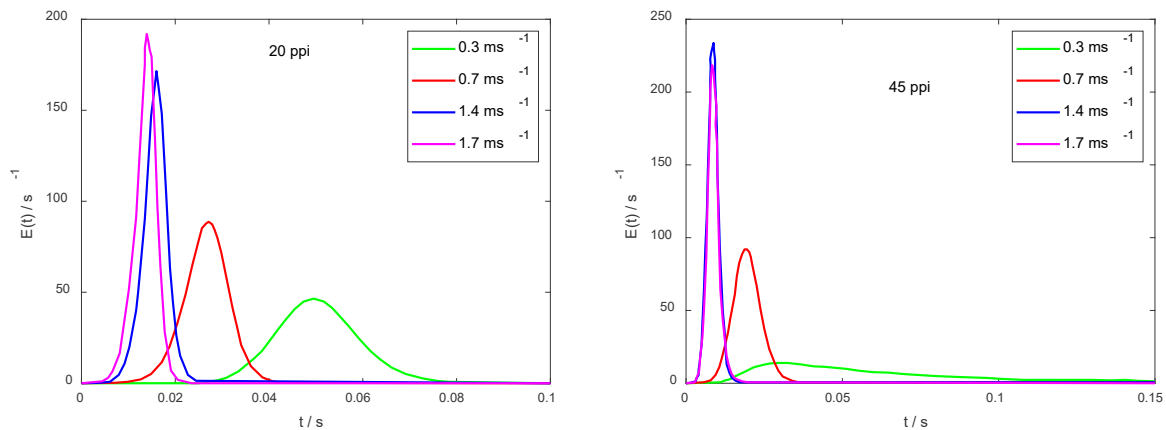
Figure 3.13. $E(t)$ of droplets computed from CFD at different gas velocities and foams with pore density for Rosin-Rammler droplets injections. The foams length is 15 mm (right) and 10 mm (left).
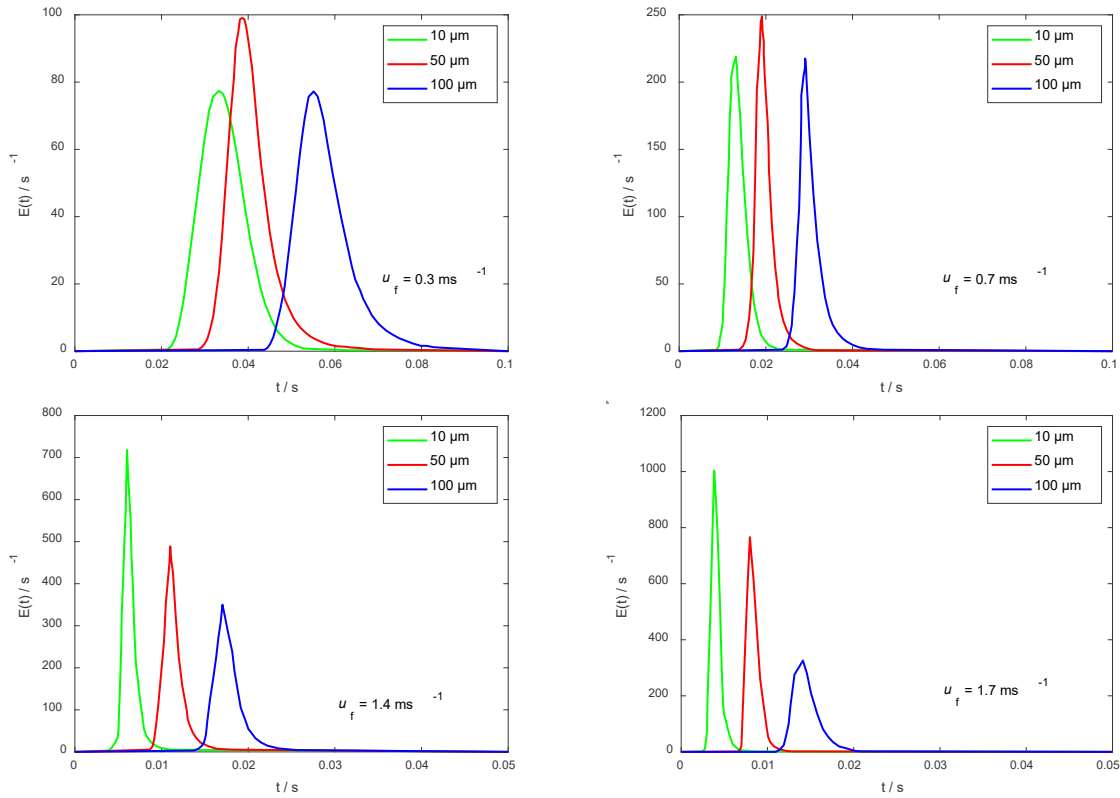
Figure 3.14. E(t) of droplets computed from CFD at different frontal superficial gas velocities and droplet sizes, for foam with a pore density of 20 ppi. The foam length is 15 mm.
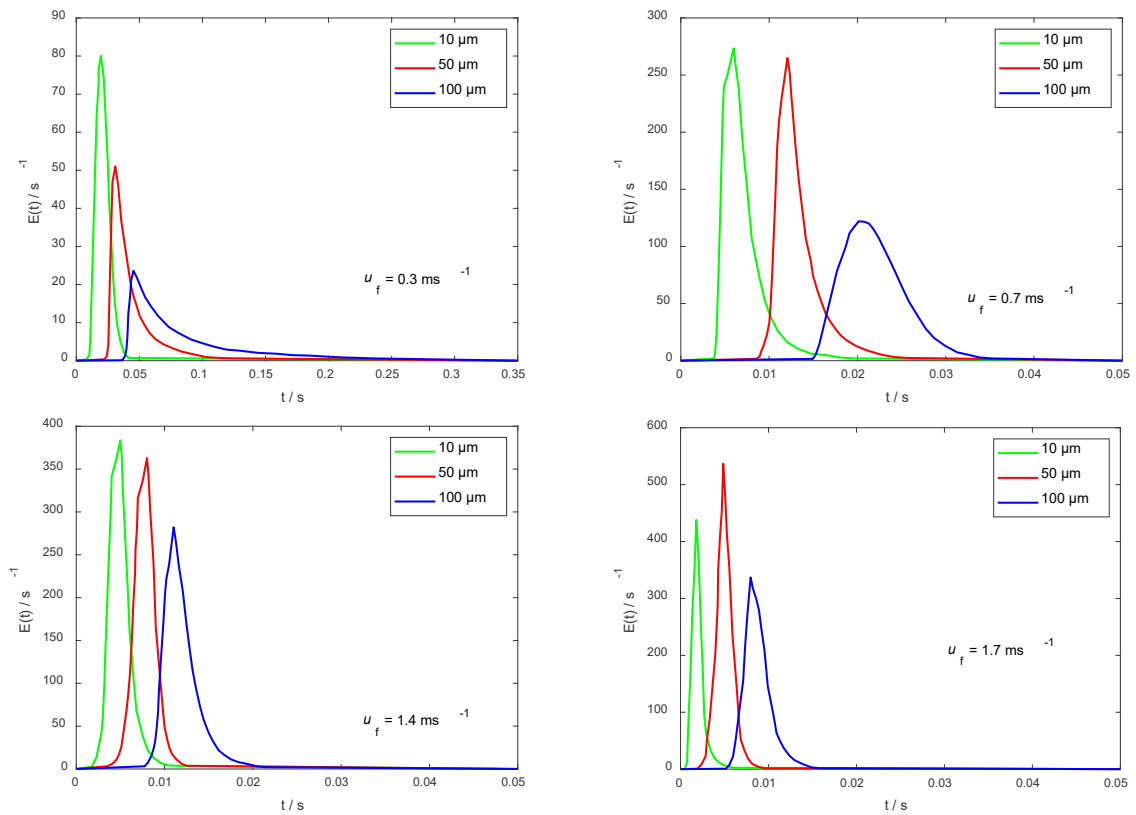
Figure 3.15. E(t) of droplets computed from CFD at different frontal superficial gas velocities and droplet sizes, for foam with a pore density of 45 ppi. The foam length is 10 mm.

Table 3.8. Parameters of the droplet RTDs in accordance with the modified Dagum distribution.

Pore density / ppi	Foam length / mm	u_f / ms^{-1}	Injected droplet diameter / μm	k	α	β	γ	ζ	Mean RTD / s
20	15	0.3	10	6.63	2.88	0.03	0.02	1.00	0.034
			50	0.89	5.54	0.01	0.03	1.00	0.041
			100	1.26	3.71	0.01	0.04	1.00	0.058
			Rosin-Rammler	2.17	5.33	0.04	0.02	1.00	0.051
		0.7	10	2.57	2.57	0.01	0.01	1.00	0.014
			50	0.45	25.90	0.02	0.00	1.00	0.020
			100	0.29	43.29	0.03	0.00	1.00	0.030
			Rosin-Rammler	2.21	12.77	0.05	-0.02	1.00	0.027
		1.4	10	1.00	4.06	0.00	0.00	1.00	0.006
			50	1.00	3.46	0.00	0.01	1.00	0.011
			100	1.00	4.41	0.00	0.01	1.00	0.018
			Rosin-Rammler	0.42	15.63	0.02	0.00	0.42	0.016
		1.7	10	0.34	29.16	0.00	0.00	1.00	0.005
			50	67.07	20.23	0.01	0.00	67.06	0.010
			100	21.32	14.28	0.01	0.00	21.31	0.015
			Rosin-Rammler	0.32	18.15	0.02	0.00	0.32	0.014
45	10	0.3	10	7.08	2.37	0.03	0.01	1.00	0.022
			50	5.28	1.34	0.00	0.03	5.27	0.086
			100	0.03	42.44	0.04	0.00	1.00	0.101
			Rosin-Rammler	79.18	1.42	0.00	0.00	79.18	0.102
		0.7	10	1.26	2.09	0.00	0.01	1.00	0.008
			50	0.20	30.55	0.01	0.00	1.00	0.014
			100	7.76	2.18	0.02	0.02	1.00	0.022
			Rosin-Rammler	3.07	4.69	0.02	0.00	1.00	0.019
		1.4	10	1.00	5.30	0.00	0.00	1.00	0.003
			50	1.37	11.05	0.01	0.00	1.00	0.007
			100	64.34	8.43	0.01	0.00	64.34	0.012
			Rosin-Rammler	0.53	8.93	0.01	0.00	0.52	0.009
		1.7	10	1.00	2.16	0.00	0.00	1.00	0.003
			50	1.00	13.07	0.01	0.00	1.00	0.006
			100	1.00	4.24	0.00	0.01	1.00	0.010
			Rosin-Rammler	1.38	6.69	0.01	0.00	1.00	0.009

Figure 3.16 compares the residence times of the 20 and 45 ppi foams. Both Dagum RTDs were scaled to a foam length of 30 mm by utilizing Equation 48, which accounts for the convolution of distributions. The droplet inertia ($\rho_d^2 d_d^2 / 18\mu_d \rho_g$) at 20°C for d_d of 100, 50, and 10 μm are equal to 0.45, 0.115, and 0.0046 s, respectively. RTDs are shown in terms of boxplots, which graphically show the droplet spectra through statistic quartiles. No significant difference in the residence time is observed for the smallest droplet inertia of 0.0046 s in foams with pore densities of 20 ppi (d_d = 2.4 mm) and 45 ppi (d_d = 1.0 mm). Droplets with diameters below 10 μm are unaffected by the foams because the droplet size is significantly smaller than the mean foam pore size as for d_{pore}/d_d = 240. For droplets with diameters beyond 50 μm, there is a significant difference in the times the droplets are retained within the foam, which increases with decreasing mean pore size to $d_{pore}/d_d \leq 48$.
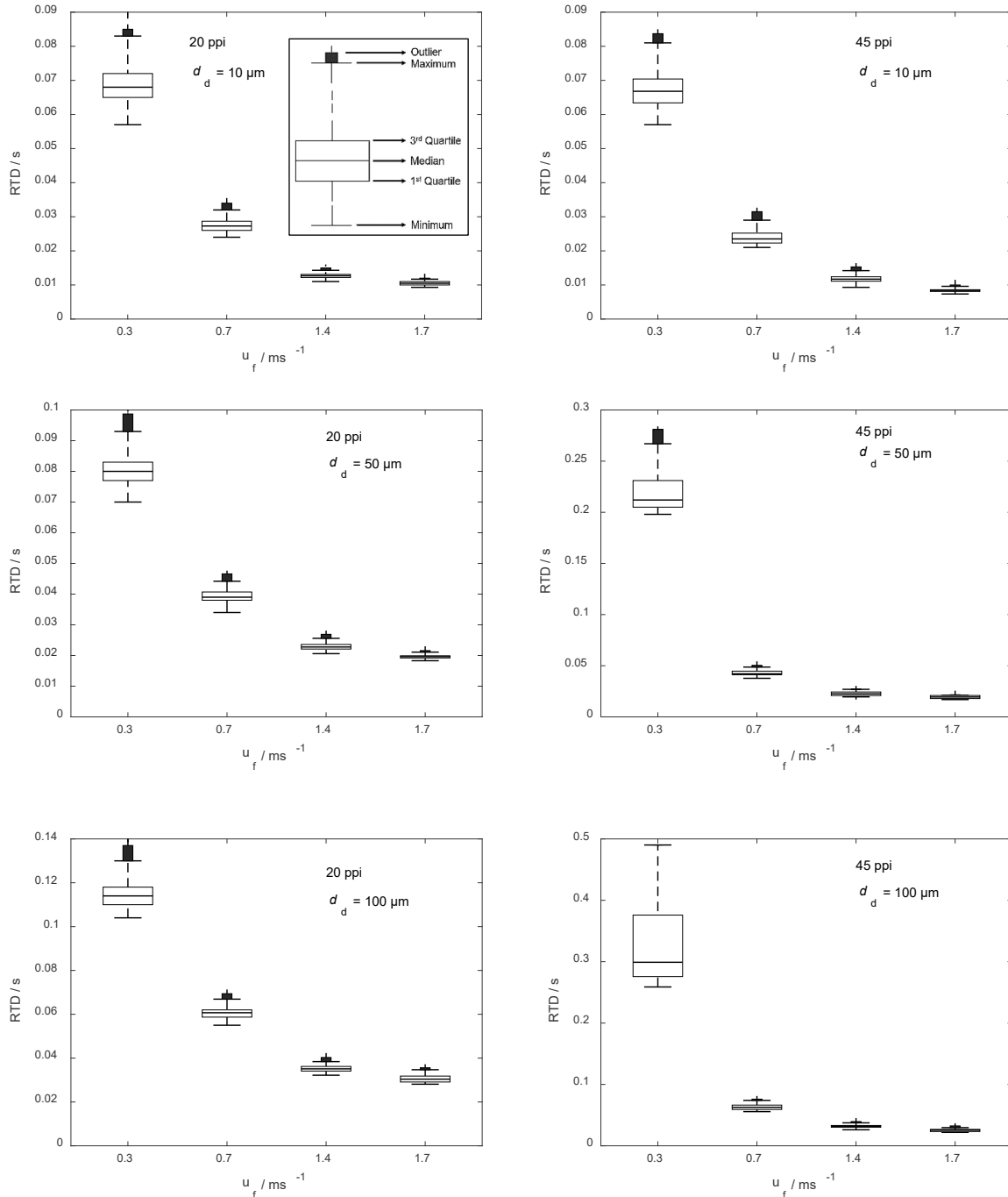
Figure 3.16. Box-plots of the droplet RTDs at different gas velocities and droplet sizes for foams of 30 mm in length with pore densities of 20 ppi (right) and 45 ppi (left).

3.7 Effects of pore density and gas velocity on droplet separation

The fraction of droplets escaping and those droplets being trapped by crashing against a surface is shown in Figure 3.17, where evaporated droplets are intentionally not included. Note, that splash-generated droplets are also considered in the trapped and escaped categories. The pore density of the 20 ppi foam allows more droplets to escape than that of the 45 ppi foam.

The 20 ppi foam has less specific surface area, implying a lower droplet impact probability with the foam skeleton. It is also shown that an increase in the superficial gas velocity decreases the percentage of escaping droplets. This can be explained by the fact that as the droplet inertia increases, the motion of droplets resists longer the entrainment effect of the long-lived flow patterns within the foam structure. As droplets are dominated by their inertia, the trajectories they follow decrease, avoiding impact with the foam skeleton. For both pore densities, there is no significant difference in the number of droplets escaping the foams to injected droplets with diameters $d_d > 50$ μm in both laminar and turbulent flows (maximum $u_f = 17$ m/s). When the droplets with 10 μm diameters are injected, the percentage of droplets escaping the foam is considerably larger compared with that for the larger droplets. Thus, the foam with a pore density of 20 ppi allows 84.5 % of the droplets to pass through its structure without impacting.
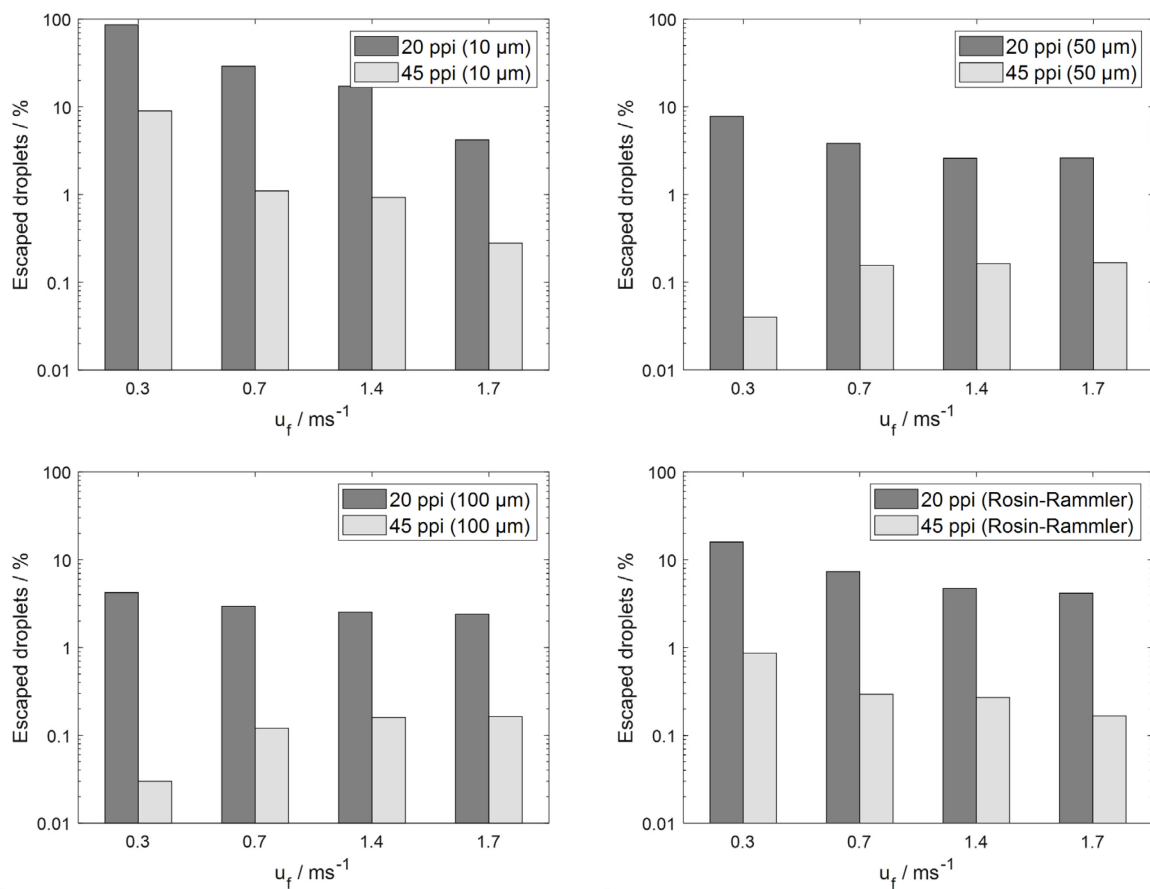
Figure 3.17. Percentages of droplets escaping the foams for injected droplet sizes of 10 μm (left-top), 50 μm (right-top), and 100 μm (left-bottom) and the Rosin−Rammler distribution (right-bottom).

3.8 Effect of foams materials on the droplet contact angle

This section studied the hydrodynamic performance of droplet capture and retention time using SiSiC open-cell foams. These materials are based on Silicon Carbide (SiC) and exhibit similar properties as other SiC-based foams as well as similar skeletal networks when produced using the same fabrication technique. Therefore, the presented droplet retention time would apply to

similar SiC foams with similar structures, i.e. pore sizes, cell sizes, and porosities. However, hydrodynamic results may differ depending on the generation of re-entrained droplets, which is influenced by the wetting properties of the droplet-foam combination. The ability to retain captured droplets is determined by their ability to spread over a surface, which is dependent on interfacial tension and equilibrium contact angle. Droplets that cannot be permanently captured may eventually be entirely or partially re-entrained [100].

In this thesis, various SiC-based materials were used as droplet separators. However, pure SiC was not used. Pure SiC powder must be sintered at high temperatures and/or pressures due to its covalent bond properties [101]. Therefore, it is preferable to use additives to facilitate the sintering process, leading to various forms of SiC ceramics, such as: Silicon-infiltrated Silicon Carbide (SiSiC), Silica-Bonded Silicon Carbide (SBSiC) and SSiC (Pressureless sintered Silicon Carbide (SSiC). These SiC-based materials and an additional low-loss magnesium-aluminium-cyclosilicate ($Mg_2Al_3(Si_5AlO_{18})$), also called cordierite, were used for producing open-cell foams (IKTS Fraunhofer, Germany). The contact angles of the foam materials were measured using an Olympus BX60M microscope by placing deionized water droplets on bulky foam substrates. Images were later examined using the contact angle plug-in implemented in ImageJ [91]. Table 3.9 summarize the measured left (θ_{LEFT}), right (θ_{RIGHT}) and average ellipse (θ_E) contact angles. The measurement of all contact angles revealed values less than 90°, which indicates that all materials exhibit hydrophilic behavior. The order of the materials, from lowest to highest hydrophilicity, is SBSiC > SSiC > Cordierite > SiSiC. A decrease in contact angle increases the interfacial area between the droplet and the substrate. Thus, better droplet retention and enhanced heat transfer are expected for foam substrates with small contact angles.

Table 3.9. Contact angle of water droplets on SiSiC, SSiC, SBSiC and Cordierite materials.

	SiSiC		SSiC		SBSiC		Cordierite	
Foam								
Angle / °	Average	Std. Dev.	Average	Std. Dev.	Average	Std. Dev.	Average	Std. Dev.
θ_E	77.7	5.4	60.1	4.4	34.7	5.9	68.1	6.0
θ_{LEFT}	76.6	5.9	58.8	4.1	34.4	4.7	69.9	5.5
θ_{RIGHT}	78.9	4.9	61.4	4.9	35.0	7.5	67.3	7.0

3.9 Conclusion

This chapter used a tomography-based pore-scale modeling approach to study the flow of droplets within open-cell foams. These representations were utilized to construct a pore-scale model of the foam and study the flow of droplets within the pores. The tomography-based pore-scale modeling approach has several advantages over other methods for studying droplet flows within open-cell foams. One major advantage is the detailed three-dimensional representations of the skeleton, which can be used to capture the complex geometry of the foams accurately. This is particularly important for skeletons, with very irregular shapes and sizes of cells. Volume renderings and a series of morphological characterization routines were applied to the

tomographic datasets. The tomographic datasets were used to discretize a computational domain into a mesh representing the foam skeleton. This mesh was utilized to perform numerical calculations of fluid flow within the foam. Computations of the minimum MRCV showed convergence of porosity values for nondimensional lengths $L_{\mathrm{MRCV}}/d_{\mathrm{cell}} > 6$ and $L_{\mathrm{MRCV}}/d_{\mathrm{cell}} > 15$ within ±5 % and ±1 % for the 20 and 45 ppi foams, respectively.

Numerical calculations were computed in the commercial software package Fluent. Pressure gradient measurement data were used to validate and select the turbulence RNG $k-\epsilon$ model, including standard wall functions and swirl modification. An Euler-Lagrangian approach was used to model the disperse droplet flow. Inlet superficial gas velocities were evaluated up to $1.7~\mathrm{ms}^{-1}$ for entraining droplets with diameter between $10 - 100$ µm. Droplet capture was implemented by using a splashing/deposition threshold criterion for droplets impinging on surfaces with the same roughness as the materials from which the foams are produced. The criterion was evaluated regarding the impact energy of the droplets with the skeletal foam surface.

A Lagrarian approach was employed to determine droplets' residence time distribution and the capture efficiency of open-cell foam structures. The residence time distribution was fitted and reported using a modified Dagum distribution function, while droplet capture was determined by the percentage of escaped liquid. The key findings of the numerical calculations are:

- The probability of the droplet impact with the foam skeleton increases with increasing superficial gas velocity.

- For a pore-to-droplet diameter ratio of $d_{\mathrm{p}}/d_{\mathrm{d}} \leq 50$, the droplet residence time increases with the pore density. It is recommended to use foams with high pore densities for practical applications as they exhibit better separation performance.

- For superficial gas velocities below $1.7~\mathrm{ms}^{-1}$ and pore-to-droplet diameter ratio of $d_{\mathrm{p}}/d_{\mathrm{d}} \geq 240$, the droplet residence times for foams with pore densities ranging between 20 and 45 ppi are found to be statistically similar. Under these conditions, there is no observable enhancement in droplet separation performance for foams of varying pore densities.

These conclusions are not exclusive for SiC-based foams but would also apply to other porous ceramic foams featuring similar skeletal networks.

Chapter 4

Experimental analysis of dielectric properties of open-cell foams

In this chapter, different ceramic foam materials are characterized with regard to their dielectric properties. Additionally, the permittivity results from experiments are compared with those estimated from mixture relations, providing a comprehensive evaluation of the data.

Parts of this chapter have been published in:

J. N. Camacho Hernandez, G. Link, S. Soldatov, A. Füssel, M. Schubert, and U. Hampel, "Experimental and numerical analysis of the complex permittivity of open-cell ceramic foams," Ceram. Int., vol. 46, pp. 26829-26840, 2020. In accordance with Elsevier permission guidelines: Authors can include their articles in full or in part in a thesis or dissertation for non-commercial purposes.

4.1 Foam materials and samples

In the previous chapter, several SiC-based and cordierite foams were proposed for capturing and evaporating droplets in foams. The SiC-based materials are SBSiC, SSiC and SiSiC, which are described [102] as follows:

- SBSiC is an oxide-bonded SiC ceramic manufactured from coarse and medium-grained SiC powders by sintering at standard pressure, during which amorphous silica or cristobalite (or both) bond the SiC particles.

- SSiC is produced using very fine SiC powder that contains sintering additives.

- SiSiC is produced by the reaction of molten silicon with compact SiC powder, containing a high amount of free carbon. Initially, the carbon reduces the native silica layer on the SiC particles. The infiltrating melted silicon then reacts with the remaining free carbon to produce secondary SiC leading to SiC-bonding between the SiC grains. The remaining melted silicon fills the inter-particle voids creating a somewhat dense microstructure.

The fabrication material ingredients and microstructures of SBSiC, SSiC, and SiSiC are presented in Table 4.1 and Figure 4.1, respectively. These solid foams have a macro-porous open-cell structure composed of stiff vertices interconnected with struts, which form a continuous three-dimensional network. This structure can be visualized in the image of an SiSiC solid foam presented in Figure 2.5. The foam structure results from the replication technique, wherein the polymeric template defines the cell size and shape. The polymeric templates were impregnated with a ceramic slurry. The excess slurry was then removed by squeezing and centrifugation, resulting in the uniform coating of the polymer foam struts. During the subsequent heat treatment, the polymeric template was decomposed by pyrolysis, and the ceramic material became sintered. The same SiC powders were used to manufacture the SSiC and SiSiC test samples, which were used to identify the influences of the various compositional materials and binding types (see Table 4.1). These powders were fine and reactive with a median grain diameter $d_{50} \approx 2$ μm. The SBSiC also included a second coarser SiC powder ($d_{50} \approx 20$ μm) to achieve a fine-to-coarse ratio of 2:3.
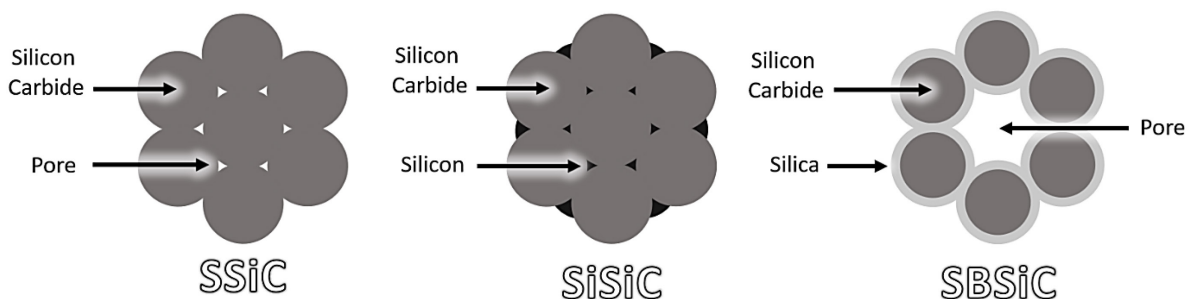
Figure 4.1. Schematic showing the structure of (left) SSiC, (center) SiSiC, and (right) SBSiC.

Table 4.1. Material composition

Material	Ingredients
SBSiC	Bi-modal SiC powder composition, silica sources and alumina powder as inorganic binder matrix.
SSiC	Fine SiC powder, organic temporary binder acting as carbon source after pyrolysis, and boron as a sintering aid.
SiSiC	Fine SiC powder, acting as carbon source after pyrolysis to react with the infiltrated silicon.
Cordierite	Composition of cordierite chamotte, bentonite, alumina, clay, and soapstone.

Cylindrical samples of the bulk material and the open-cell foams were produced by IKTS Fraunhofer, Germany, for the purpose of dielectric characterization. The same suspension was used for both sample types to identify the structure-related differences between the foam and bulk samples. The foam samples had nominal pore densities of 30 ppi, 45 ppi, and 60 ppi, and porosities in the range of 86.9 % – 96.5 %. The average cell diameters of the foams were determined by optical 2D image analysis of light micrographs using a Pore!Scan-System from Goldlücke GmbH [103] and are summarized along with other foam properties in Table 4.2.

Table 4.2. Bulk and foam sample properties for dielectric characterization.

Material	Description	Average cell diameter / μm	Density / gcm^{-3}	Porosity / %	Diameter / mm	Height / mm
SSiC	Bulk	–	2.88	8.7	7.9	10.0
	30 ppi	≈ 1460	0.19 – 0.21	93.3 – 94.1		
	45 ppi	≈ 890	0.11 – 0.15	95.2 – 96.4	76.9 ± 1.0	9.0 ± 1.0
	60 ppi	≈ 600	0.11 – 0.17	94.7 – 96.5		
SiSiC	Bulk	–	2.69	0.0	7.9	10.0
	30 ppi	≈ 1460	0.27 – 0.35	88.0 – 88.9		
	45 ppi	≈ 890	0.20 – 0.22	90.9 – 91.8	7.4 ± 0.5	9.5 ± 0.5
	60 ppi	≈ 600	0.18 – 0.20	92.2 – 93.0		
SBSiC	Bulk	–	2.14	29.1	7.9	10.0
	30 ppi	≈ 1460	0.18 – 0.28	90.7 – 94.0		
	45 ppi	≈ 890	0.16 – 0.22	92.6 – 94.7	7.2 ± 0.7	9.3 ± 0.7
	60 ppi	≈ 600	0.22	92.7		
Cordierite	Bulk	–	1.80	29.3	7.9	10.0
	30 ppi	≈ 1460	0.33- 0.37	85.3 – 87.2		
	45 ppi	≈ 890	0.27 – 0.49	80.7 – 89.5	7.4 ± 0.5	9.5 ± 0.5
	60 ppi	≈ 600	0.27	89.5		

4.2 Experimental determination of dielectric properties

The dielectric properties of solid materials can be determined by various techniques [104]. Among them, the cavity perturbation technique compares resonance frequency f_1 and quality

factor Q_1 of a cavity without perturbation against resonance frequency f_2 and quality factor Q_2 of the same cavity after perturbation by a small material sample. The complex permittivity of the sample is then calculated according as

$$\varepsilon'_{\text{eff}} = \frac{V_{\text{cavity}}}{V_{\text{sample}}} \frac{(f_1 - f_2)}{A * f_2} + 1 \; ,$$

(60)

$$\varepsilon''_{\text{eff}} = \frac{V_{\text{cavity}}}{B * V_{\text{sample}}} \left(\frac{1}{Q_1} - \frac{1}{Q_2} \right),$$

(61)

where V_{cavity} is the cavity volume and V_{sample} is the sample volume [60]. The cavity perturbation technique utilizes two coefficients, A and B, to determine the dielectric properties of a material. These coefficients can be determined through calibration, which can be achieved by using samples of known permittivity or by using a numerical calibration procedure. The numerical calibration procedure involves the use of full-wave 3D electromagnetic simulations to correlate the frequency shift $(f_1 - f_2)$ and the changes in the quality factors $(1/Q_1 - 1/Q_2)$ with a given permittivity value. The complex permittivity can be calculated from the measured scattering parameters (S-parameters) by using this correlation [105]. The transmission factor S_{21}, is the ratio of the transmitted power at output port 2 to the incident power at input port 1 characterizes the resonance behavior. A schematic of the experimental system used to acquire the complex permittivity of the samples is shown in Figure 4.2.
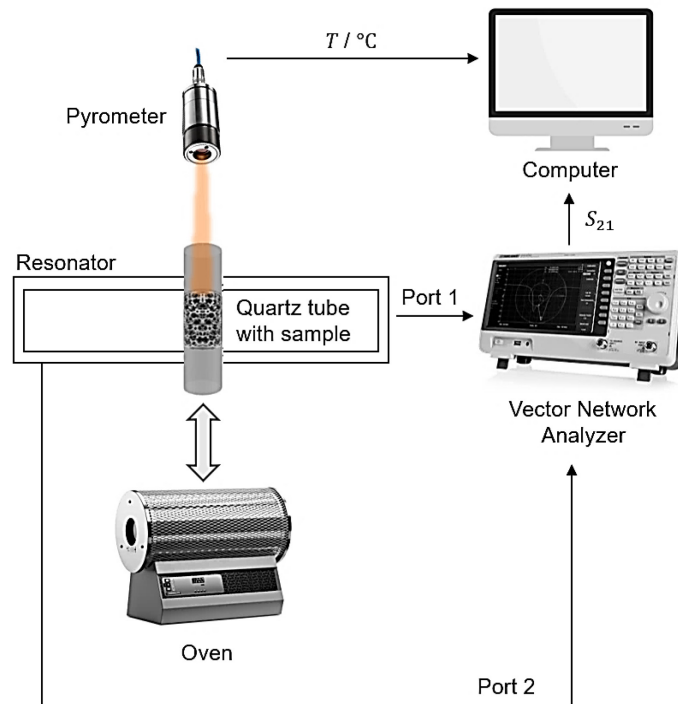
Figure 4.2. Schematic of the dielectric measurement system using the cavity perturbation technique.

The resonator was based on a standard rectangular WR-340 waveguide cavity, and the length of the cavity was chosen to be resonant at a frequency of 2.45 GHz in the TE_{104} mode. Thus,

the electric field standing wave pattern had four maxima along the longest side of the cavity. The microwave signals were coupled using inductive coupling ports with 10 mm width and 43.18 mm height on both ends. The cavity was connected to a vector network analyzer (VNA E5071C from Agilent) with coaxial-to-waveguide adaptors and coaxial cables to measure the S_{21} parameter. Two small opposing holes were made in the cavity walls at the position of one of the four electric field maxima to enable the positioning of the sample inside the cavity (within a quartz tube sample holder). A pyrometer (Cella-Temp-PA from Keller) at the opposite end measured the sample surface temperature inside the resonator. A resistive tubular furnace (MFT 12/38/400 from Carbolite) was placed in front of the waveguide, allowing the sample to be heated up to 1200 °C before entering the cavity. A more detailed description of the dielectric measurement system is provided by Soldatov et al. [106]. This study's characterization was performed in the temperature range of 30 °C – 200 °C. The parameter S_{21} and the temperature were recorded using a computer-controlled data acquisition system, which also provided automatic control of predefined heating scenarios. Finally, the measured resonance frequency shifts and Q-factors were post-processed to calculate the real and imaginary parts of the effective permittivity at various temperatures via Equations 60 and 61.

The temperature-dependent measurements using the cavity perturbation method were used to obtain the effective dielectric constants and the effective loss factors of the cordierite and SiC-based samples, as shown in Figure 4.3. In contrast to the bulk SiSiC sample, the other materials had significant residual porosities (SBSiC: 29.1 %, SSiC: 8.7 %, cordierite: 29.3 %) as listed in Table 4.2. Notably, the bulk did not necessarily refer to samples having a 100 % theoretical density, since no subsequent sample compaction was possible, except for the eventual sintering shrinkage, which can be applied to produce bulk samples from foams. The permittivity of the bulk SiC-based sample was not included in the data analysis as their high losses result in excessive cavity perturbation leading to unreliable results. The error bars in Figure 4.3 for all materials represent the variations in permittivity resulting from the spread in sample geometry as shown in Table 4.2 for fabrication tolerance errors in the diameter and the height of samples.
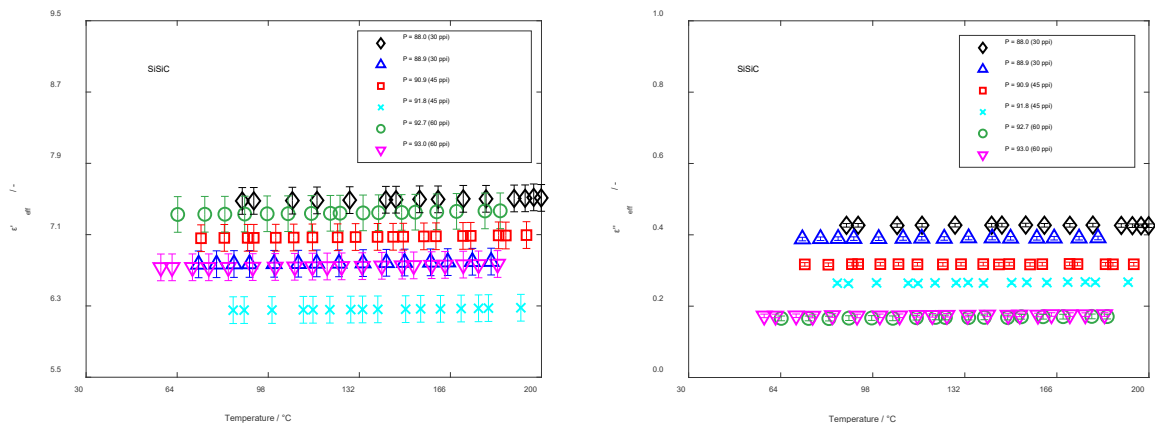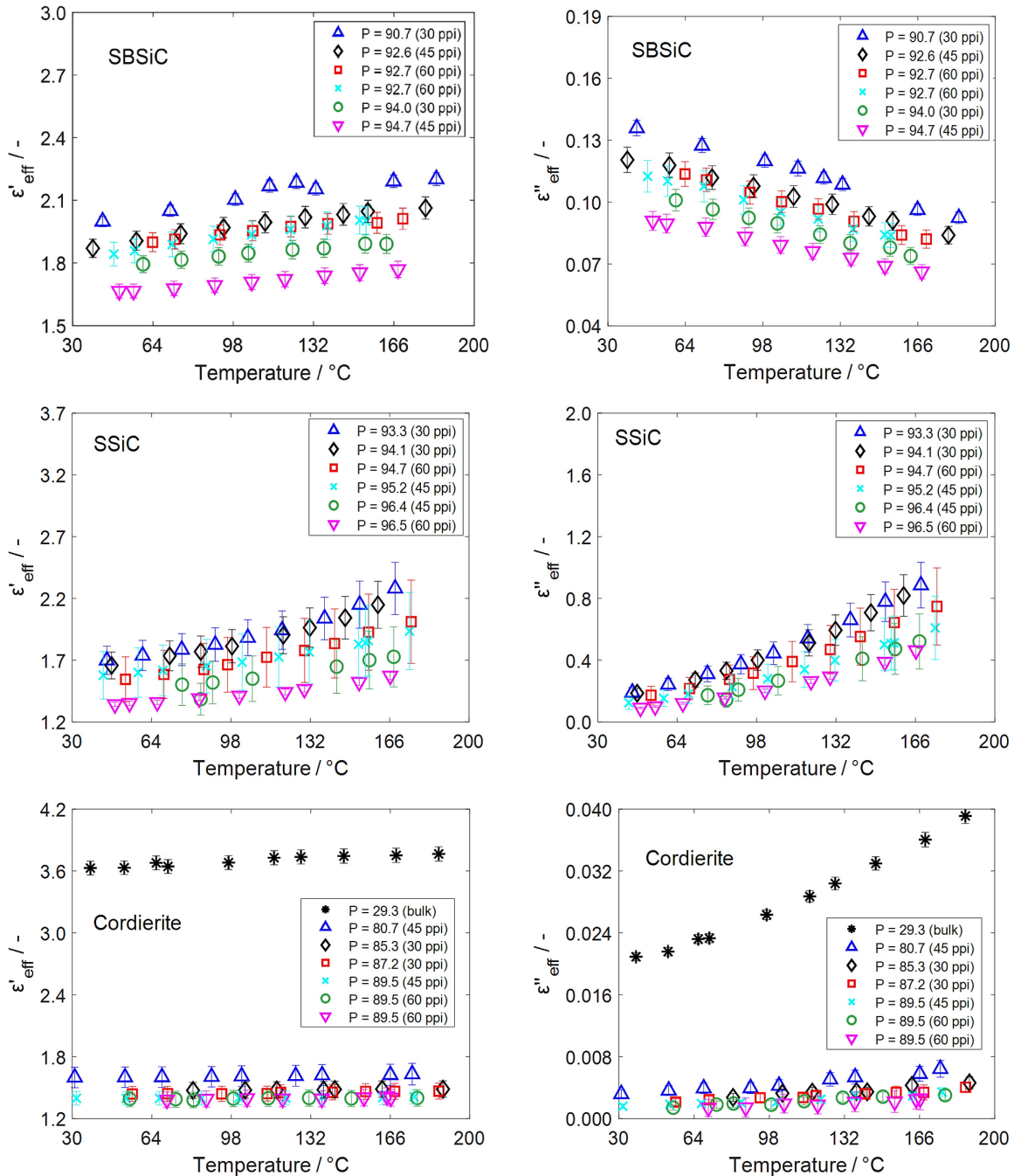
Figure 4.3. Effective dielectric constants (left) and effective loss factors (right) of cordierite (first row), SiSiC (second row), SBSiC (third row), and SSiC (fourth row) at a frequency of 2.45 GHz.

As can be seen in Figure 4.3, no clear trend could be observed for the permittivity related to the skeleton structure and pore density. However, the dielectric properties of SiC ceramic foams depend strongly on the characteristics of their doping, additives and impurities. This is evidenced by the significant difference in permittivity observed between SiSiC and the samples of SSiC and SBSiC, presumably related to the infiltration of free silicon into the structure of the SiSiC foam. Since silicon is a semiconductor with a dielectric constant of approximately 11.9 [107] at 2.45 GHz, the resulting effective dielectric constant is higher than the SiC-based foams that do not contain free silicon.

Highly porous materials always retain some water in their pores from the ambient atmosphere. Being exposed to elevated temperatures causes water to leave the material, thus leading to a decrease in its effective permittivity. The effect of water depletion on the effective permittivity competes in foams made from typical dielectrics like oxides, nitrides, or carbides, which have increasing trends in permittivity versus temperature. Additives, such as silicon and carbon in SiC-based foams, could cause increased effective loss factors, which correlate with the SiC skeleton temperature behavior and inversely with water depletion. The interplay of these three factors that define the resulting temperature behavior of the permittivity of the foams in this study differs between SSiC and the other foams.

The dielectric loss factor of the SSiC demonstrated a significant temperature dependence, in contrast to other samples. This likely arose from the presence of a higher fraction of silicon carbide and the excess carbon, as indicated by Table 4.1, which were not completely consumed by the native silica layer of the SiC particles during the sintering process. Adding carbon to SiC (C–SiC) [108], produces a conductivity change from n-type to p-type, so a greater amount of carbon would increase the conductivity and, therefore, its loss factor. Furthermore, as observed for SSiC, increasing temperature increases carbon-based conductivity, leading to a higher permittivity [109]. Additionally, after the manufacturing process is complete, some additive materials used in the manufacturing process may remain as reacted materials or binders. In this study, boron was employed as a sintering aid for SSiC. Incorporating boron as a trivalent dopant in SSiC leads to the creation of p-type electron vacancies, resulting in increased electrical conductivity and, thus, higher permittivity.

Compared to SSiC, SBSiC does not contain any species source adding carbon or boron but rather incorporates alumina (Al_2O_3) and silica (SiO_2). The dielectric constant of fused amorphous silica is approximately 3.8 for the frequency range of 1×10^{-5} to 40 GHz [110], and it is known for its low dielectric loss factor, typically less than 1×10^{-3} [111]. Thus, the dielectric behavior of SBSiC can be attributed to the permittivity competition of only SiC and water. Interestingly, the water depletion resulted in a decrease of the loss factor with increasing temperature. According to Figure 4.3, the microwave absorbance of SiSiC and cordierite foams can be considered constant within the studied temperature range.

The assessment of whether the foam behaves as an effective homogeneous medium or not is also important for characterizing the foams. Foams can be considered to behave as an effective medium when the wavelength of the incident electromagnetic radiation λ is much larger than their mean cell size. Therefore, a criterion such as an inclusion size parameter given as $x = 2\pi r/\lambda$ can be used to determine whether the system behaves as an effective medium. The parameter r represents the inclusion or particle size, which corresponds to the cell size for foams. Mishchenko et al. proposed a threshold value of $x < 0.15$ [67], to assess the suitability of considering a mixture as an EMA medium. Their study involved analyzing Lorenz-Mie dispersion matrixes from mixtures generated by using the Maxwell-Garnet formula. The proposed threshold value suggests that for inclusion sizes above this value, the dispersion matrix of the host-inclusion mixture deviates from the dispersion matrix produced by an EMA medium.

In order to evaluate x, the wavelength of the radiation propagating through the material and the cell size of the foams must be determined. The wavelength is known to depend on the permittivity of the medium according to $\lambda = \lambda_0 / \sqrt{\varepsilon'_{\text{eff}}}$, where λ_0 is the wavelength in a vacuum. The cell size, represented as the diameter of the largest sphere that can fit within the cell structure, was found to have values of ~1.46 mm and < 1 mm for the 30 ppi and 60 ppi foams, respectively. As seen in Table 4.3, the inclusion size parameters for all foam types were found to be below the threshold value ($x < 0.15$), indicating that the foams can be treated as EMA media.

Table 4.3. Calculated maximum inclusion size parameters for the foams. Note that, 30 ppi foams were used for the calculations because they have the largest cell diameter.

Foams	SiSiC	SSiC	SBSiC	Cordierite
$\varepsilon'_{\text{eff,30ppi}}$	7.10	1.67	1.85	1.45
λ / mm	46.4	99.3	90.7	101.32
x_{30ppi}	0.10	0.05	0.05	0.05

4.3 Permittivity mixing relations

Mixing relations were employed to describe the effective permittivity of ceramic foams based on their porosities and bulk permittivities. Moreover, SiC powder and SiC foam data from the literature [112, 113] were used as additional data for the SSiC material. The bulk permittivities of the SiSiC, SBSiC, and SSiC were not directly measured. Instead, they were determined through iterative least-squares estimations by fitting the experimental data to the mixing relations. As the porosity approaches 1, the effective permittivity of the foam should converge to the permittivity of the material filling the voids, denoted as $\varepsilon'_{\text{eff}(P=1)} = \varepsilon'_{\text{f}}$. For air this value corresponds to $\varepsilon'_{\text{air}} \approx 1.00$ at 25 °C and remains constant within the studied temperature range. Conversely, if the porosity is 0, the effective permittivity corresponds to that of the ceramic material of the foam, that is $\varepsilon'_{\text{eff}(P=0)} = \varepsilon'_{\text{c}}$.

4.3.1 Effective-medium approximations

The most widely used EMA relations [70-73] described in Table 2.3, were employed to fit the experimental data simultaneously. As seen in Figure 4.4 those relations correspond to the Maxwell-Garnett approximation (Maxwell type relation), the Bruggeman-Landauer approximation (self-consistent relation), the Differential Effective Medium (DEM, differential relation), the exponential relation (from Rice [73]), and the Pabst-Gregorová exponential relation [74]. The dimensional parameter d for the spheres was set as $d = 3$. The adjustable parameter B of the Pabst-Gregorová exponential relation was set to $B = 2$ for the spherical pores [74], and B used in the exponential relation (from Rice [73]) was estimated from experimental data fitting.
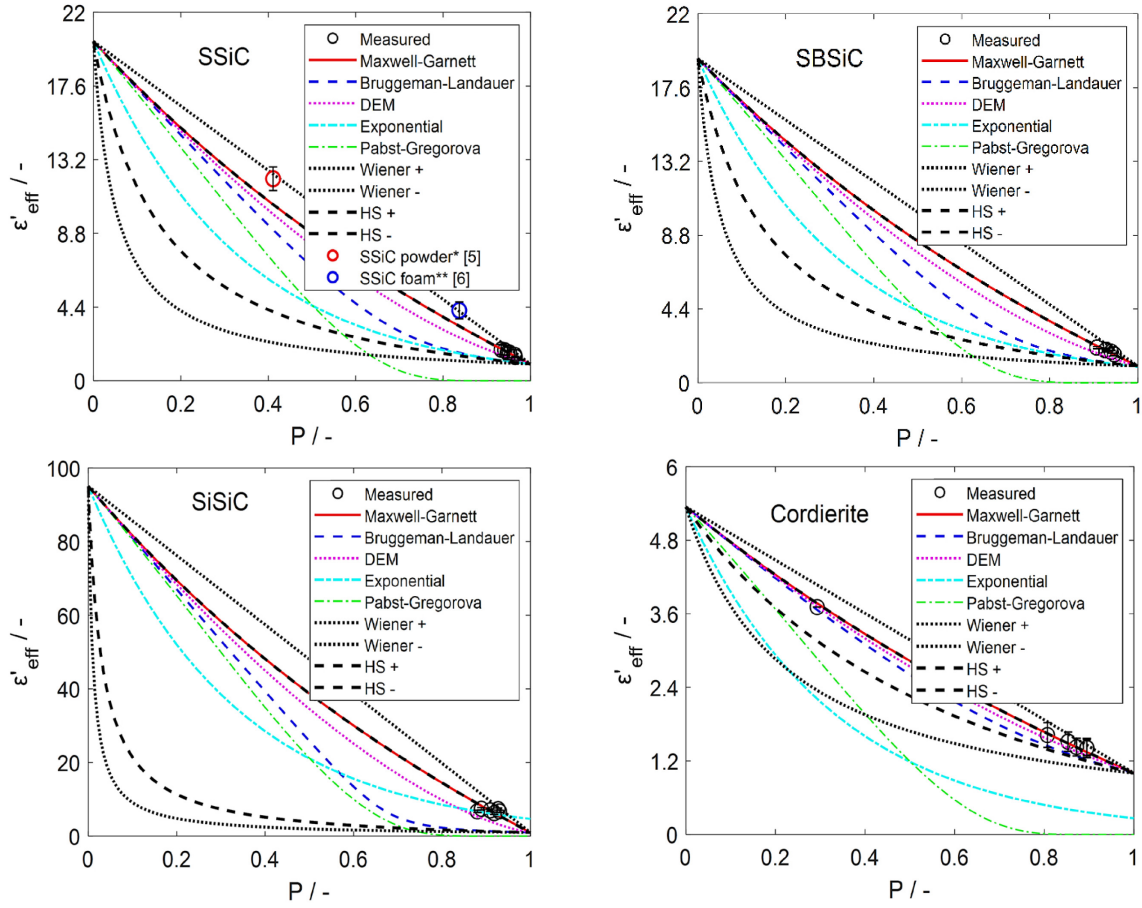
Figure 4.4. Comparison of the measured and predicted effective dielectric constants using various effective medium approximation relations for SiSiC (lower-row, left), SBSiC (upper-row, right), SSiC (upper-row, left) and cordierite (lower-row, right) at 2.45 GHz and 100 °C. The SSiC permittivities from powder extrapolated to 100 °C powder* [112] and foam** [113] were used for comparison.

The estimated ε'_{eff} of the fully dense materials were $\varepsilon'_{SiSiC} = 95.05 \pm 0.31$, $\varepsilon'_{SBSiC} = 19.34 \pm 0.10$, $\varepsilon'_{SSiC} = 20.26 \pm 0.40$, and $\varepsilon'_{Cordierite} = 5.35 \pm 0.21$. The best agreement was obtained using the Maxwell-Garnett relation for the SiC-based foams among the compared relations. The Maxwell-Garnett approach is a non-symmetric relation wherein the sphere inclusions are well-separated from each other.

Additionally, there was some agreement between the temperature extrapolated permittivities up to 100 °C of the powder and foam made from SiC and the Maxwell-Garnett approach relation for the SSiC, despite these materials having a slightly different composition. Further, the dielectric constant of fully dense SSiC ($\varepsilon'_{SSiC} = 20.26 \pm 0.40$) agrees with the extrapolated value of $\varepsilon'_{SSiC} = 20.3 \pm 0.3$ (at 100 °C) from a fully dense tile sample of SiC with boron impurities [114].

4.3.2 Fixed-parameter weighted mean relations

Fixed-parameter weighted mean relations [73], based on arithmetic, harmonic, and geometric means (as listed in Table 2.2 and 2.3), were also used for fitting the experimental data

simultaneously. The Hashin-Shtrikman (HS) bounds were used along the fixed-parameter weighted mean relations, because the foams were considered to be contained within the anisotropic permittivity limits. The results are shown in Figure 4.5.
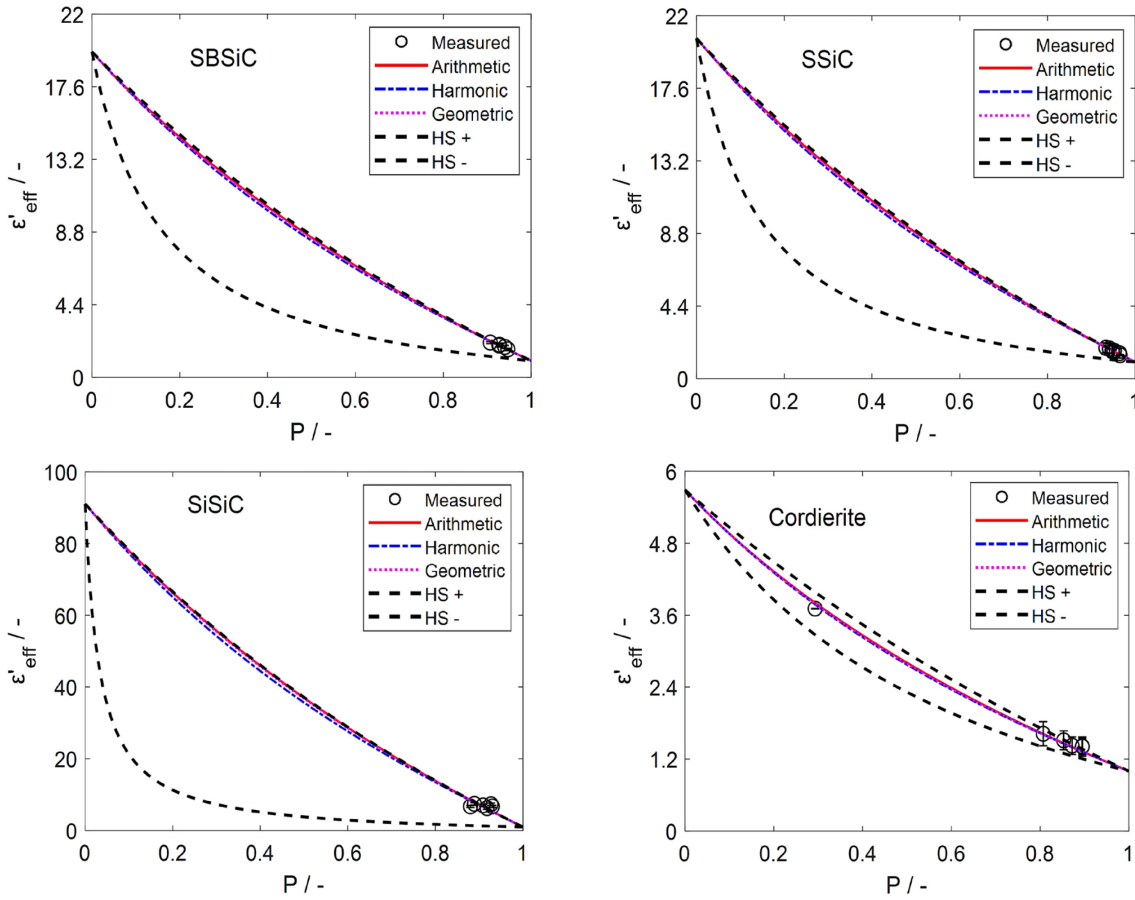
Figure 4.5. Comparison of measured and predicted effective dielectric constants using the weighted mean relations with Hashin-Shtrikman bounds for SiSiC (lower-row, left), SBSiC (upper-row, right), SSiC (upper-row, left) and cordierite (lower-row, right) at 2.45 GHz and 100 °C.

The estimated effective dielectric constants of the fully dense materials for the fixed-parameter weighted mean relations were $\varepsilon'_{\text{SiSiC}} = 91.07 \pm 0.31$, $\varepsilon'_{\text{SBSiC}} = 19.73 \pm 0.10$, $\varepsilon'_{\text{SSiC}} = 20.63 \pm 0.40$, and $\varepsilon'_{\text{cordierite}} = 5.69 \pm 0.21$, which agreed exceptionally well with the values estimated by the effective-medium approximations.

For the SiC-based foams, the weighted mean relations were practically reduced to the fitted upper bound because the data were primarily concentrated at the right side of the graph, that is $P > 0.8$. Thus, the lines for the upper Wiener or HS bounds nearly overlapped as $\Psi_{\text{arithm}} \approx \Psi_{\text{harm}} \approx \Psi_{\text{geom}} \approx 0$. Conversely, the measured data for the cordierite were between the HS bounds. All weighted mean relations agreed well with the measured data. The weight parameters estimated for cordierite using the HS bounds were $\Psi_{\text{arithm/geom/harm}} \approx 0.25$ and $\varepsilon'_{\text{cordierite}} = 5.69$.

4.3.3 General sigmoidal mean relations

The general sigmoidal mean relation was also used for fitting the experimental data simultaneously. The N-parameter in the general sigmoidal mean relation [73] denotes the type of volume-weighting, which is $N \neq 0$ for the non-geometric (harmonic for $N = -1$ and arithmetic for $N = 1$) and $N = 0$ for geometric as listed in Tables 2.2 and 2.3. Figure 4.6 shows the comparison of the measured and predicted effective dielectric constants for different N-parameters.
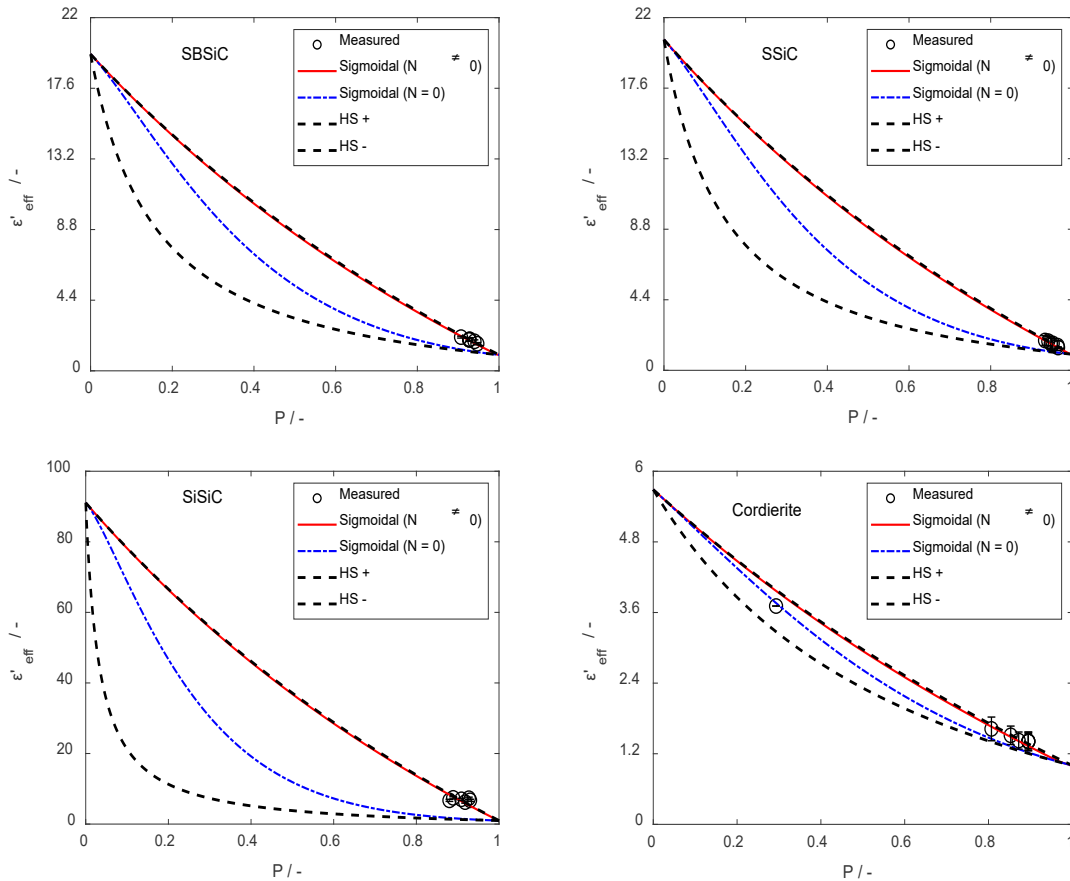
Figure 4.6. Comparison of measured and predicted effective dielectric constants using the general sigmoidal mean relations for different N-parameters and bounds for SiSiC (lower-row, left), SBSiC (upper-row, right), SSiC (upper-row, left) and cordierite (lower-row, right) at 2.45 GHz and 100 °C.

The estimated effective dielectric constants of the fully dense materials for the general sigmoidal mean relation were essentially equal to those obtained from the weighted mean relation, which is probably related to both relations using the HS bounds. All materials show a good agreement for $N \geq 60.83$, corresponding with the volume-weighted superarithmetic mean relations coinciding with the Hashin-Shtrikman upper bound.

4.3.4 General power mean relations

The general power mean relation was also fitted using the experimental data simultaneously. Like the previous relation, the n-parameter in the general power mean relation [73] denotes the type of volume-weighting, which is harmonic for n = -1, geometric for n = 0, and arithmetic for n = 1. The comparison of the predicted and measured effective dielectric constants is shown in Figure 4.7.
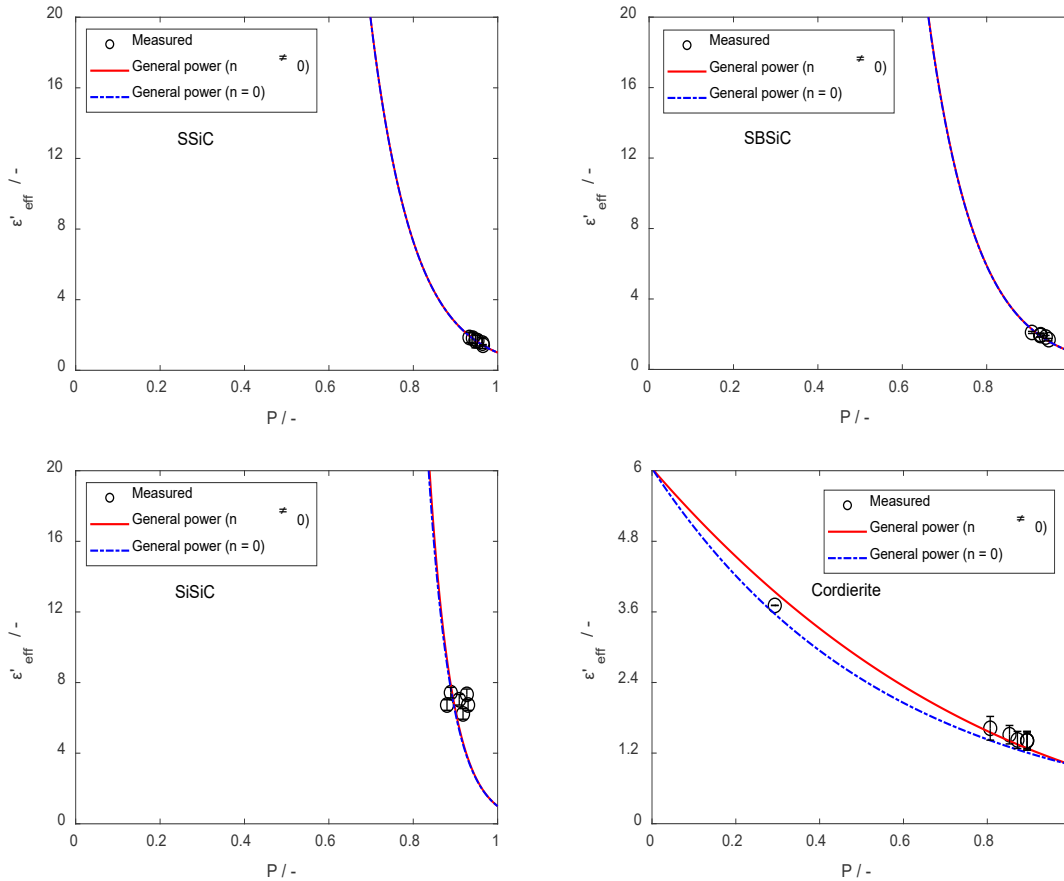
Figure 4.7. Comparison of predicted and measured effective dielectric constants using the general power mean relations (solid line: n = 0, dashed line: n ≠ 0); and bounds for the SiSiC (lower-row, left), SBSiC (upper-row, right), SSiC (upper-row, left) and cordierite (lower-row, right) at 2.45 GHz and 100 °C.

Power relations do not well represent ε'_{eff} of the SiC-based materials because the data were mainly located on the right side of the graphs, which caused unrealistically high values of the fully dense effective dielectric constant, i.e. $\varepsilon'_{SiSiC} \gg 1000$, and n to be almost zero. In contrast, n = 0.237 was determined for the cordierite. Interestingly, this value agrees well with n = 1/3, which is the predicted n value of the Landau-Lifshitz and Looyenga formula [115, 116] given as $\varepsilon'^{1/3}_{eff} = (1 - P)\varepsilon'^{1/3}_c + P\varepsilon'^{1/3}_f$. This formula was developed for the finely dispersed mixing of isotropic particles, which is also a reasonable assumption for cordierite foams. The dielectric constant estimated for the fully dense cordierite is $\varepsilon'_{cordierite}$ = 6.038.

4.4 Conclusion

The effective permittivity of SiC-based foam materials with pore densities of 30, 45, and 60 ppi were quantitatively determined by applying the cavity perturbation technique. As the permittivity is frequency- and temperature-dependent, permittivity measurements were performed at a microwave frequency of 2.45 GHz up to 200°C. Both the effective dielectric constant and the effective loss factor of the SiSiC and SBSiC foams showed remarkably different values compared to pure SiC. This could be attributed to the additives or dopants used during the sintering of the foams, which cause changes in the conductivity either by creating p-type electron vacancies or by providing n-type free electron carriers. It was also found that the permittivity of foams depends on the porosity but demonstrates no dependence on the pore density and pore size. This is a highly interesting finding in the context of droplet flow within open-cell foams, as it suggests that any foam with a pore density greater than 20 ppi can be selected to remove droplets without significantly impacting its microwave heating performance. The results of this study indicate that the permittivities of SiC-based open-cell foams, including SBSiC, SSiC, and SiSiC, exhibit skin depths ranging from 15 to 65 cm. Skin depth refers to the depth at which the radiation intensity within a material falls to ~37 % of its initial value. This is interesting, as it suggests that any of these SiC-based open-cell foams are viable options for microwave heating applications in industrial pipes up to diameters of 15 cm.

Estimating the effective permittivity of open-cell foams using mixing relations was also investigated. To achieve this, the existing literature relations for effective permittivity estimation were applied and the results were compared with experimental data. The best agreement was obtained by using the Maxwell-Garnett relation for the SiC-based foams. In addition, the permittivity of foams made of cordierite was as also measured. A satisfactory agreement to cordierite foam permittivity was obtained by using the general power mean relation. The experimental data were fit to this relation, which resulted in an exponent value of $n \approx 1/3$. This value agrees with the prediction of the well-known Landau mixing model prediction exponential value of 1/3.

Chapter 5

Estimation of dielectric and thermal properties of open-cell foams

In this chapter, a novel topological mixture relation for estimating the effective relative permittivity of solid foams is derived from electromagnetic wave propagation calculations. The topological relation estimates are compared to other mixture relations and experimental data. Additionally, a comprehensive assessment was performed comparing the topological relation and published experimental data for thermal conductivity.

Parts of this chapter have been published in:

1. J. N. Camacho Hernandez, G. Link, M. Schubert, and U. Hampel, "Modeling of the effective permittivity of open-cell ceramic foams inspired by platonic solids," Materials, vol. 14, pp. 7446, 2021. In accordance to MDPI Open Access Information and Policy: No special permission is required to reuse all or part of article published by MDPI, including figures and tables.

2. J. N. Camacho Hernandez, G. Link, M. Schubert, and U. Hampel, "Novel mixing relations for determining the effective thermal conductivity of open-cell foams," Materials, vol. 15, pp. 2168, 2022. In accordance to MDPI Open Access Information and Policy: No special permission is required to reuse all or part of article published by MDPI, including figures and tables.

5.1 Morphology modelling open-cell foams made of sintered ceramics

Two morphology classes, i.e., foam and Platonic solids, were analyzed to compare their influences on the effective complex permittivity. Two samples of open-cell ceramic foams with pore densities of 20 and 30 ppi, respectively, made of SiSiC, were used for the foam morphology models. X-ray micro-computed tomography was used to obtain cross-sectional slices of the foam. The slices were then compiled into stacks with a voxel size of 56 μm, and a small representative cubic volume of 10 mm edge length was selected to reduce the computational burden while preserving porosity. As described in Section 3.2, mesh reconstruction of the models was achieved by applying the marching cube algorithm [91], followed by the removal of small non-connected skeleton structures. Further, mesh simplification, smoothing, and uniform resampling [117] were performed for mesh optimization. Eventually, the reconstructed models of the "sintered foams" attained porosities of 89.3 % and 89.8 % for the 20 ppi and 30 ppi foams, respectively. The porosities agree well with those reported by the manufacturer of 88 % and 89 %, respectively. Finally, the meshes were imported into the CST Microwave Studio Suite and incorporated as inclusions within boxes, where the boxes enclose the ceramic foams and air, as shown in Figure 5.1.
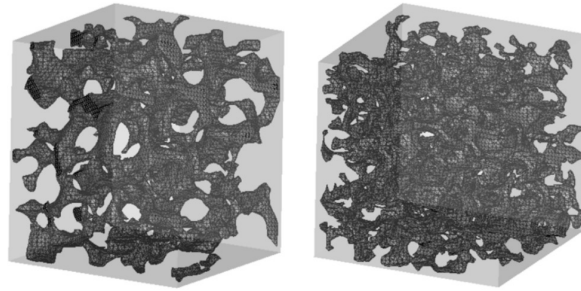
Figure 5.1. Illustration of the mean representative cubic volume element (MRCV) of the sintered foams (left: 20 ppi, right: 30 ppi).

Additional meshes with lower porosities were produced using a 3D dilation and erosion filter to study the porosity over a wide range [118, 119]. This filter dilates the cross-sectional structure of the foam by using a spherical kernel diameter of 3 voxels, which increases or reduces the skeleton volume and modifies the porosity. The mean cell diameters d_{cell} and mean strut diameters d_{st} of the foams were determined by using a 3D thickness method [120]. d_{cell} and d_{st} are summarized in Table 5.1.

Table 5.1. Cell and strut diameters of the sintered foams (mean ± standard deviation).

	P	0.25	0.37	0.55	0.72	0.89
20 ppi	d_{cell} / mm	1.33 ± 0.44	1.58 ± 0.28	1.85 ± 0.33	2.10 ± 0.49	2.65 ± 0.51
	d_{st} / mm	1.93 ± 0.23	1.41 ± 0.52	1.03 ± 0.42	0.95 ± 0.21	0.64 ± 0.20
	P	0.18	0.34	0.52	0.70	0.89
30 ppi	d_{cell} / mm	0.70 ± 0.17	0.92 ± 0.14	1.13 ± 0.19	1.22 ± 0.20	1.68 ± 0.54
	d_{st} / mm	1.22 ± 0.26	0.84 ± 0.20	0.70 ± 0.30	0.53 ± 0.13	0.37 ± 0.12

5.2 Morphology modelling open-cell foams with Platonic skeletons

Platonic solids are regular polyhedrons with identical faces and equal vertex angles. The polyhedrons that were used in this work were hexahedrons, octahedrons, icosahedrons and dodecahedrons [121]. An important feature of these solids is that they can be inscribed in a cube enclosure with outer cube faces that exhibit periodicity as illustrated in Figure 5.2. This guarantees that these cubes when juxtaposed, repeat the Platonic solids with the same spatial arrangement. In the case of octahedrons, two arrangements satisfy periodicity: $octahedron_1$ (the struts cross at the center of the cube faces) and $octahedron_2$ (the struts cross at the center and corners of the cube faces). Throughout this thesis, these arrangements of Platonic solids will be referred to as the periodic cubic enclosure arrangement (PCA) of Platonic inclusions.
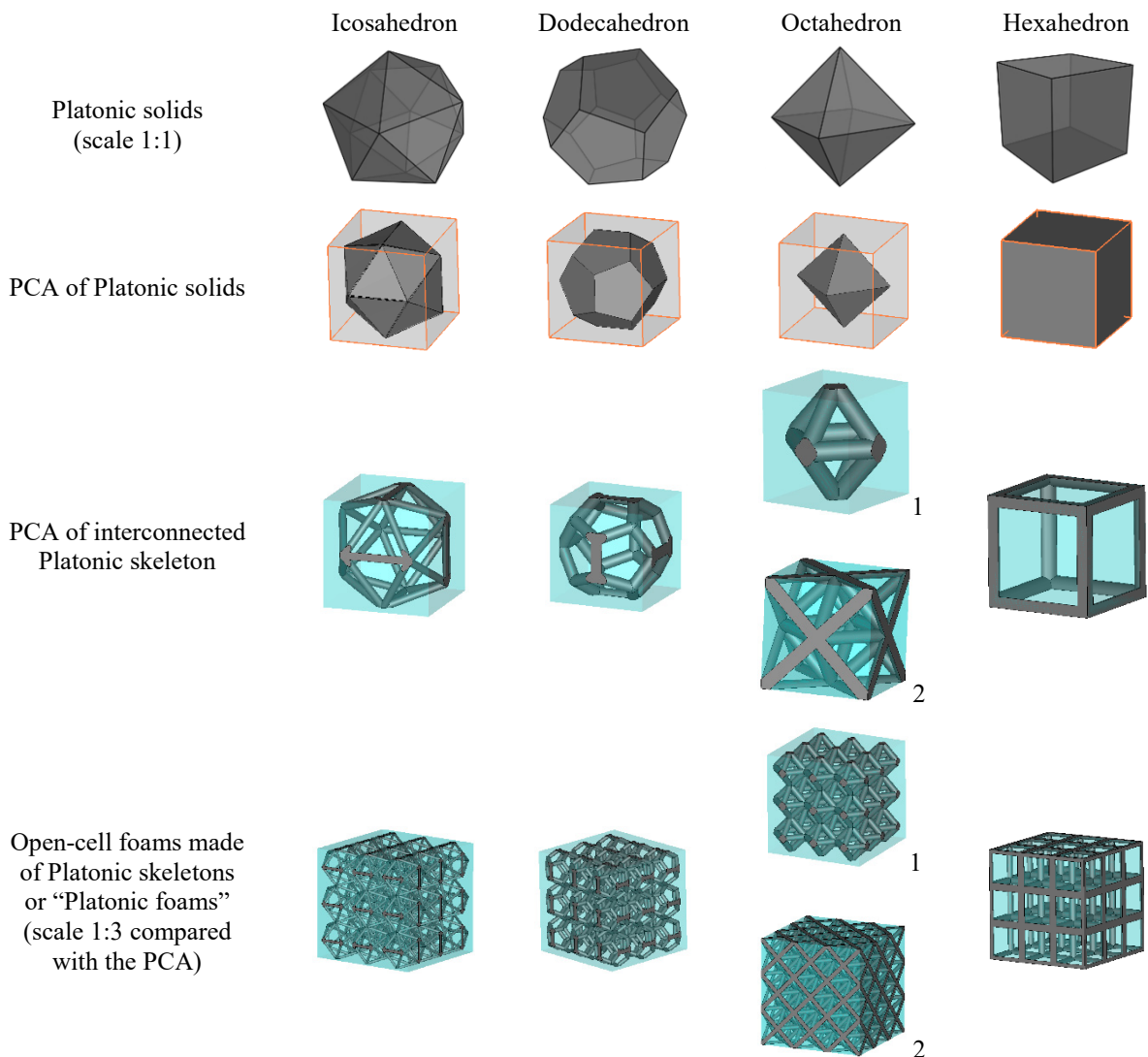
Figure 5.2. Geometrical structures of open-cell foams built from Platonic skeletons. (1: $Octahedron_1$, 2: $Octahedron_2$).

The cylinders at the edges of the Platonic solids form an interconnected network that is equivalent to the skeleton of open-cell foams with their struts and joints. However, such a simplification adds a geometrical defect given as a gap at the vertices where the cylinders come across each other. These gaps can be easily filled using Boolean operations with a spherical triangle, as shown in Figure 5.3. In this way, a PCA of interconnected Platonic networks is obtained, which upon replication in any direction (x, y or z) forms the open-cell foams of Platonic skeletons that are referred to as "Platonic foams" (see Figure 5.2, bottom row). Their cylinders represent by analogy the struts of sintered foams. Then, a sphere inscribed in the Platonic network is by analogy the equivalent of a cell of sintered foams. Moreover, since the geometries of these foams are regular, both their cylinders and spheres have constant diameters, d_{cyl} and d_{sp}, respectively, as shown in Figure 5.4.
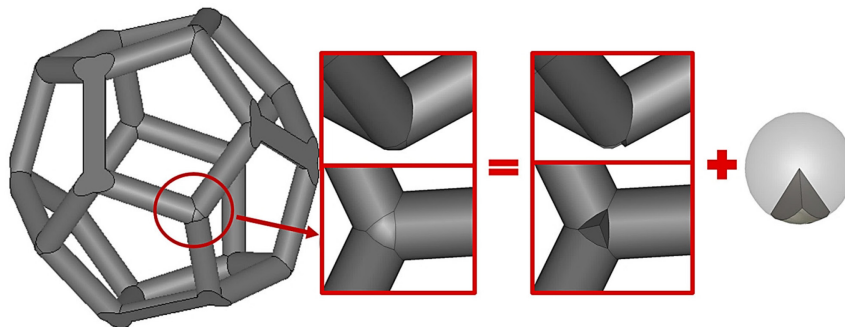
Figure 5.3. Example of vertex filling for the dodecahedron structure.
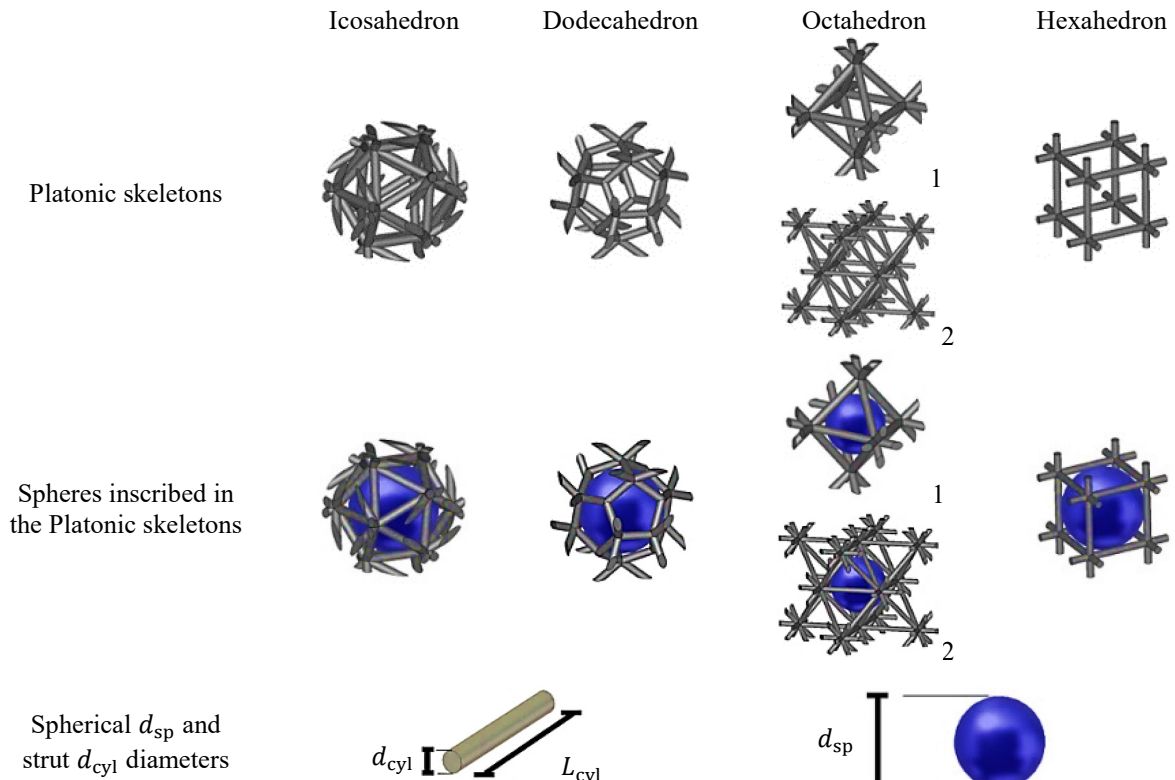
Figure 5.4. Visual representation of the Platonic foams.

The volume of the skeleton V_p can be calculated from the diameter d_cyl and length L_cyl of the cylinders, as the Platonic foams are composed of identical geometric elements. The relation between L_cyl and the side length of the PCA L_PCA is defined for each Platonic foam, as given in Table 5.2. Also, the porosity of Platonic foams can be expressed as a function of their structural geometric elements as given in Table 5.3. It is important to note that Platonic foams have a limit to their existence as porosity changes. When d_cyl becomes large enough for the struts to overlap, the skeleton cells close, and the Platonic geometry is no longer preserved.

Table 5.2. Formulas to calculate the volume of the Platonic skeletons.

Platonic skeleton	Relation between L_cyl and L_PCA	Volume of the Platonic skeleton
Hexahedron	$L_\mathrm{cyl} = L_\mathrm{PCA}$	$V_\mathrm{p} = \dfrac{3}{4}\pi d_\mathrm{cyl}{}^2 L_\mathrm{cyl} - \sqrt{2}d_\mathrm{cyl}{}^3$
Octahedron$_1$	$L_\mathrm{cyl} = L_\mathrm{PCA}/\sqrt{2}$	$V_\mathrm{p} = 3\pi d_\mathrm{cyl}{}^2 L_\mathrm{cyl} - \left(\dfrac{59}{8} + \dfrac{93}{100}\left(\sqrt{8}-\sqrt{6}\right)\right)d_\mathrm{cyl}{}^3$
Octahedron$_2$	$L_\mathrm{cyl} = L_\mathrm{PCA}/\sqrt{2}$	$V_\mathrm{p} = 6\pi d_\mathrm{cyl}{}^2 L_\mathrm{cyl} - \left(\dfrac{2939}{155} + \dfrac{93}{100}\left(\sqrt{8}-\sqrt{6}\right)\right)d_\mathrm{cyl}{}^3$
Dodecahedron	$L_\mathrm{cyl} = \dfrac{L_\mathrm{PCA}}{(3+\sqrt{5})}$	$V_\mathrm{p} = \dfrac{27}{2}\pi d_\mathrm{cyl}{}^2 L_\mathrm{cyl} - \left(\dfrac{152}{7\sin(108)} - 10\tan(54)\right)d_\mathrm{cyl}{}^3$
Icosahedron	$L_\mathrm{cyl} = \dfrac{L_\mathrm{PCA}}{2(1+\sqrt{5})}$	$V_\mathrm{p} = 27\pi d_\mathrm{cyl}{}^2 L_\mathrm{cyl} - \left(\dfrac{1}{3}\pi + \dfrac{15}{2}\sin\left(\dfrac{151}{3}\right) - \dfrac{95}{\sqrt{12}}\right)d_\mathrm{cyl}{}^3$

Table 5.3. Porosity of the Platonic foams and corresponding limits, where the Platonic geometry is no longer preserved.

Platonic Skeleton	Porosity	Limits for strut diameter and porosity
Hexahedron	$P = 1 - \left[\dfrac{3\pi}{4}\dfrac{d_\mathrm{cyl}{}^2}{L_\mathrm{PCA}{}^2} - \sqrt{2}\dfrac{d_\mathrm{cyl}{}^3}{L_\mathrm{PCA}{}^3}\right]$	$d_\mathrm{cyl} \le L_\mathrm{PCA}$ $P \ge 0.058$
Octahedron$_1$	$P = 1 - \left[\dfrac{3\pi}{\sqrt{2}}\dfrac{d_\mathrm{cyl}{}^2}{L_\mathrm{PCA}{}^2} - 7.73\dfrac{d_\mathrm{cyl}{}^3}{L_\mathrm{PCA}{}^3}\right]$	$d_\mathrm{cyl} \le \dfrac{L_\mathrm{PCA}}{\sqrt{6}}$ $P \ge 0.415$
Octahedron$_2$	$P = 1 - \left[\dfrac{6\pi}{\sqrt{2}}\dfrac{d_\mathrm{cyl}{}^2}{L_\mathrm{PCA}{}^2} - 19.31\dfrac{d_\mathrm{cyl}{}^3}{L_\mathrm{PCA}{}^3}\right]$	$d_\mathrm{cyl} \le \dfrac{L_\mathrm{PCA}}{\sqrt{6}}$ $P \ge 0.093$
Dodecahedron	$P = 1 - \left[\dfrac{27\pi}{2(3+\sqrt{5})}\dfrac{d_\mathrm{cyl}{}^2}{L_\mathrm{PCA}{}^2} - 9.07\dfrac{d_\mathrm{cyl}{}^3}{L_\mathrm{PCA}{}^3}\right]$	$d_\mathrm{cyl} \le \dfrac{2L_\mathrm{PCA}}{(3+\sqrt{5})}\sqrt{1+\dfrac{2}{\sqrt{5}}}$ $P \ge 0.078$
Icosahedron	$P = 1 - \left[\dfrac{27\pi}{2(1+\sqrt{5})}\dfrac{d_\mathrm{cyl}{}^2}{L_\mathrm{PCA}{}^2} - 20.60\dfrac{d_\mathrm{cyl}{}^3}{L_\mathrm{PCA}{}^3}\right]$	$d_\mathrm{cyl} \le \dfrac{2L_\mathrm{PCA}}{(\sqrt{3}+\sqrt{15})}$ $P \ge 0.267$

5.3 Numerical calculation of the effective permittivities

Sintered and Platonic foam models with different porosities were generated to analyze the influence of the skeletal morphology on ε_eff. As examples, some models are illustrated in Figure 5.5. For the Platonic foams, the diameter of the struts was varied to adjust their porosity to

match the values of the sintered foams, as shown in Table 5.1. The Platonic foam models were adjusted to a total length L of 10 mm to match L_{MRCV} of the sintered foams.
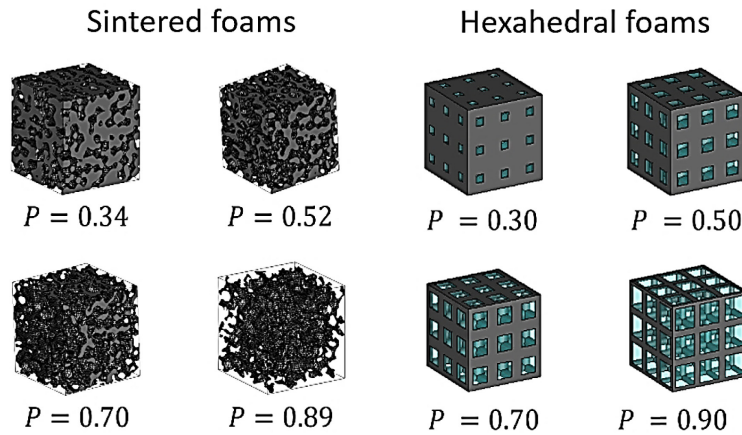
Figure 5.5. Visual representation of sintered (30 ppi) and Platonic (hexahedral) foams for different porosities.

These models were imported into CST Microwave Studio Suite (Version 2018 from Dassault Systemes) to perform electromagnetic wave propagation simulations with the transient domain solver. This commercial software uses the finite difference time-domain method to solve the integral formulation of the Maxwell equations. A frequency of 2.45 GHz was chosen for the pulse excitation signal of the microwaves. The simulation setup is shown in Figure 5.6. This simulation approach is identical to the one reported by Pickles et al. [75]. The boundary conditions are normal electric ($E_{tangential} = 0$) and magnetic ($H_{tangential} = 0$) walls for the x- and y-axes, respectively. The input (1) and output (2) are non-reflective open boundary ports with added space distance to the models equal to $\lambda/4$ for the z-axis.
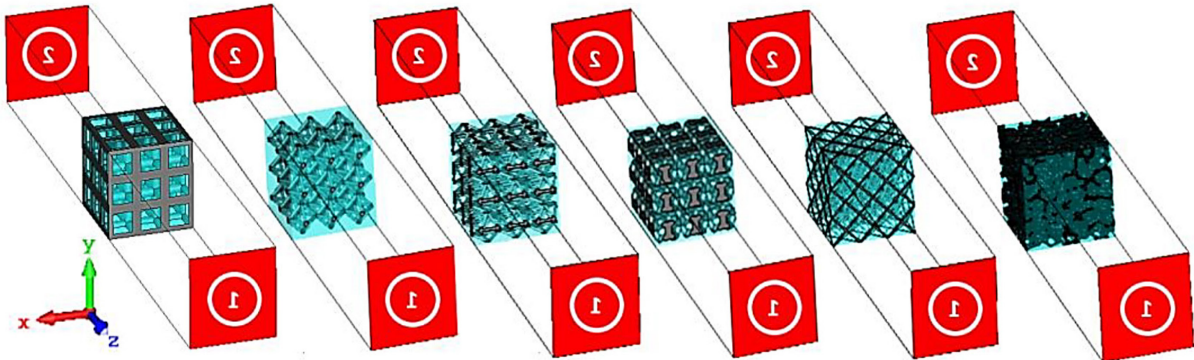
Figure 5.6. Setup of the numerical simulations to calculate the dispersion parameters (from left to right: hexahedral, octahedral$_1$, octahedral$_2$, dodecahedral, icosahedral and sintered foams, red faces represent the ports).

Loss tangent and dielectric loss of the skeleton were assigned as

    I. $\tan \delta_c = 0.23$ with $\varepsilon_c' = 10$,
    II. $\tan \delta_c = 0.46$ with $\varepsilon_c' = 20$,
    III. $\tan \delta_c = 0.91$ with $\varepsilon_c' = 40$,

which were chosen to be the double of each other to compare different permittivity contrasts while maintaining the EMA consideration for the models.

The parameters of the continuous medium were assigned as

I. $\tan\delta_f = 0.00$ with $\varepsilon'_f = 1.0$, corresponding to the permittivity of air,
II. $\tan\delta_f = 0.14$ with $\varepsilon'_f = 2.6$, this permittivity corresponds to that of a hypothetical dielectric fluid as an alternative to air.

The higher ε'_f was not chosen to match a particular fluid but rather to evaluate its effect on the effective permittivity. Moreover, the complex dielectric contrast is:

$$\frac{\varepsilon_c}{\varepsilon_f} = \frac{\varepsilon'_c\varepsilon'_f + \varepsilon''_c\varepsilon''_f}{\varepsilon'^2_f + \varepsilon''^2_f} - j\frac{\varepsilon''_c\varepsilon'_f - \varepsilon'_c\varepsilon''_f}{\varepsilon'^2_f + \varepsilon''^2_f}. \tag{62}$$

Accordingly, the complex dielectric contrasts of the foam mixtures are:

1. Skeleton: $\tan\delta_c = 0.23$ with $\varepsilon'_c = 10$, medium: $\tan\delta_f = 0.00$ with $\varepsilon'_f = 1.0$, $\varepsilon_c/\varepsilon_f = 10 - j2.3$,
2. Skeleton: $\tan\delta_c = 0.46$ with $\varepsilon'_c = 20$, medium: $\tan\delta_f = 0.00$ with $\varepsilon'_f = 1.0$, $\varepsilon_c/\varepsilon_f = 20 - j9.2$,
3. Skeleton: $\tan\delta_c = 0.91$ with $\varepsilon'_c = 40$, medium: $\tan\delta_f = 0.00$ with $\varepsilon'_f = 1.0$, $\varepsilon_c/\varepsilon_f = 40 - j36.4$,
4. Skeleton: $\tan\delta_c = 0.46$ with $\varepsilon'_c = 20$, medium: $\tan\delta_f = 0.14$ with $\varepsilon'_f = 2.6$, $\varepsilon_c/\varepsilon_f = 8 - j2.4$.

The reflected and transmitted energy, given by the S_{11} and S_{21} scattering parameters, respectively, were obtained by moving the reference planes of the ports to the faces of the models. These scattering parameters are used in the retrieval method [122] to calculate the effective permittivity of each model. This is done by calculating the impedance z and the refractive index n as

$$z = \pm\sqrt{\frac{(1 + S_{11})^2 - S_{21}^2}{(1 - S_{11})^2 - S_{21}^2}}, \tag{63}$$

$$n = \frac{1}{k_0 L}\left[\text{Im}\left\{\ln\left(\frac{S_{21}}{1 - \frac{(z-1)S_{11}}{(z+1)}}\right)\right\} + 2m\pi - i\cdot\text{Re}\left\{\ln\left(\frac{S_{21}}{1 - \frac{(z-1)S_{11}}{(z+1)}}\right)\right\}\right], \tag{64}$$

Where L is the model length between the reference ports, k_0 is the wavenumber in free space, and m is the fundamental branch of the sinusoidal function periodicity ($m = 0$ for $L < \lambda/4$, otherwise $m = \pm1, \pm2, ..., \pm\infty$). Impedance and refractive index are then used to calculate the effective permittivity $\varepsilon_{\text{eff}} = n/z$ and the effective permeability $\mu_{\text{eff}} = nz$. Since the models have no magnetic properties, μ_{eff} was only used to validate whether the impedance and

refractive index yield the permeability of a non-magnetic sample, i.e., $\mu_{\text{eff}} = 1.0 - j0.0 \pm (0.10 - j0.02)$.

For the numerical simulations, hexagonal meshes were used. The mesh size for the Platonic foams was defined based on a sensitivity study that was performed for the hexahedral foam. The objective was to achieve a mesh size for which ε_{eff} does not change more than 1 % and which produces a tolerable computational burden. Cell sizes < 133 μm (with at least 3.4×10^6 cells) were assigned to all Platonic foam meshes. Meshes with at least 1×10^7 cells were considered for the sintered foams based on the simulations performed in Chapter 3.

5.4 Effective permittivity of simulated foams

5.4.1 Analysis of the effective medium approximation applied to sintered foams

The results of the numerical calculations for the estimated effective permittivity of the sintered foams are shown in Figure 5.7. The effective permittivities of the 20 and 30 ppi sintered foams are practically the same, despite the difference in the size of their struts and cells. Such results provide evidence that the EMA consideration is plausible and that it can be verified by the inclusion size condition. Using the inclusion size parameter with a threshold value $x = 0.15$ [67], it is possible to validate the EMA assumption as

$$\varepsilon'_{\text{eff}} \ll \left(\frac{0.15\lambda_0}{\pi d_{\text{cell}}} \right)^2 . \tag{65}$$
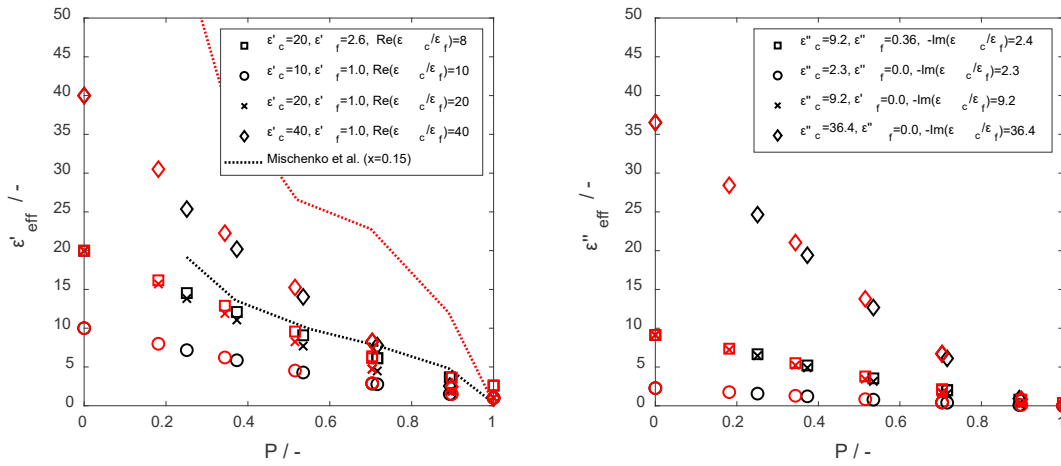
Figure 5.7. Effective dielectric constants (left) and effective dielectric losses (right) as a function of porosity obtained from numerical simulations for the sintered foams with pore densities of 20 ppi (black symbols) and 30 ppi (red symbols). Predicted thresholds (left) for the EMA assumption are shown for 20 ppi (black line) and 30 ppi (red line).

Figure 5.7 (left) shows the effective permittivity (marked with symbols) that was obtained from the numerical simulations for the sintered foams compared to the predicted thresholds for the EMA assumption (represented as lines) in accordance with the inclusion size condition. The

obtained data illustrate that the EMA assumption is valid except for some points of the 20 ppi foams with $\varepsilon'_c = 40$. As the pore size increases, the inclusion size parameter approaches the threshold value and the EMA assumption slightly begins to lose its validity. For those points that have already surpassed the threshold value, the scattering matrix of the foam ceases to replicate the scattering matrix of an EMA mixture. For example, the 20 ppi and 30 ppi samples with $\varepsilon_c/\varepsilon_f = 40 - j36.4$ do not yield comparable ε_{eff} values.

A foam analysis method is performed by using the real and imaginary susceptibility ratios of the permittivity expressed as

$$SR_{Re} = \frac{Re(\varepsilon_{eff}) - Re(\varepsilon_f)}{Re(\varepsilon_c) - Re(\varepsilon_f)}, \tag{66}$$

$$SR_{Im} = \frac{Im(\varepsilon_{eff}) - Im(\varepsilon_f)}{Im(\varepsilon_c) - Im(\varepsilon_f)}. \tag{67}$$

Figure 5.8 shows the effect of the porosity on the susceptibility ratios from the numerical simulations for the sintered foams. These data reveal the contribution of the interactions between the inclusion and the background constituents of the system. For a given porosity (except for $\varepsilon_{eff}(P = 0) = \varepsilon_c$ and $\varepsilon_{eff}(P = 1) = \varepsilon_f$), the effective dielectric constant and complex dielectric contrast do not increase proportionally [70]. As the half-wavelength of the radiation approaches the inclusion size at which resonance occurs [123], the propagating fields gradually decrease due to the evanescent and near fields generated, reducing ε'_{eff} as shown for SR_{Re}. The fact that the increase in the dielectric contrast affects SR_{Re} and not SR_{Im} is related to the shortened wavelength propagating in the foam, which following Equation 65 depends only on ε'_{eff}.
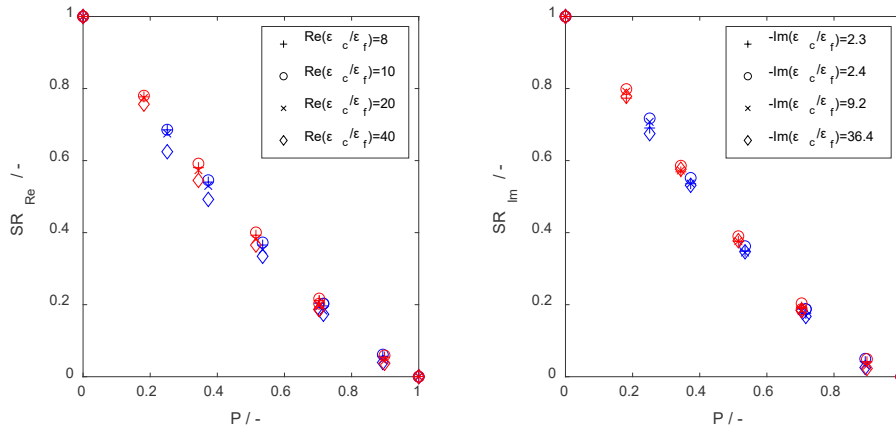
Figure 5.8. Estimated real (left) and imaginary (right) susceptibility ratios from numerical simulations for the sintered foams with pore densities of 20 ppi (blue symbols) and 30 ppi (red symbols).

5.4.2 Comparison of effective permittivity estimates of sintered foams with mixing relations from literature

Figure 5.9 shows the susceptibility ratios of the estimated effective permittivity for sintered foams (marked with symbols) compared to those that were obtained using the EMA relations (continuous data shown by lines). In addition, Figure 5.9 shows the root mean square errors (RMSE) that have been averaged for the dielectric constant and the loss factor given as $\overline{RMSE} = (RMSE_{\varepsilon'} + RMSE_{\varepsilon''})/2$. From the obtained data, it can be deduced that the DEM relation best estimates the simulated permittivity of the sintered foams, followed by the M-G relation. This is not unexpected, given that, in general, both mixing relations provide very close estimations of the effective permittivity [70]. Unlike the M-G relation, the DEM relation is symmetric to all medium components and therefore treats them all equally. Thus, the DEM relation can produce significantly better estimates in cases where the volume fraction of the inclusions is considerably large, as is the case with sintered foams.
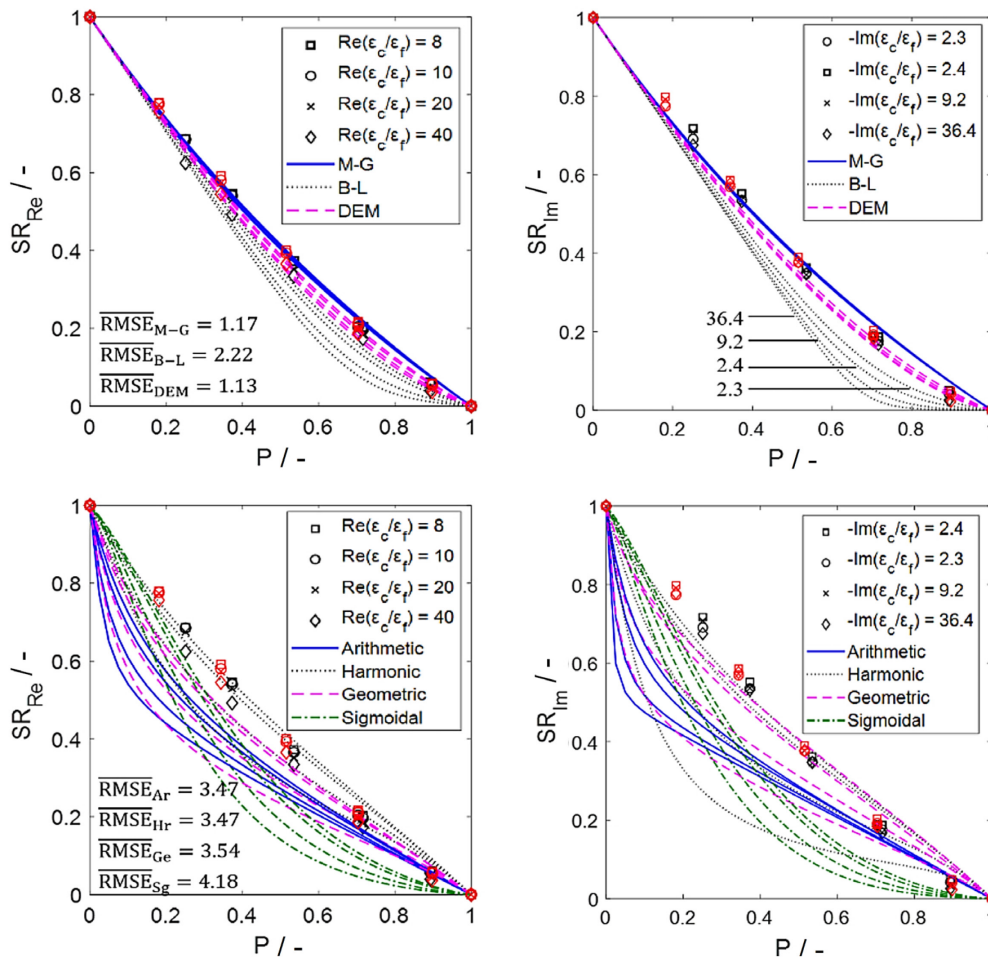
Figure 5.9. Real (left) and imaginary (right) susceptibility ratios of the EMA relations (lower row) and the probability distribution relations (upper row) compared with the calculated ratios from the numerical simulations for sintered foams for 20 ppi (black symbols) and 30 ppi (red symbols). The figure symbol corresponds to the complex dielectric contrasts of the foam mixtures, while lines show the EMA relations predictions. The curves derived from the relations follow a descending order as $\varepsilon_c/\varepsilon_f$ increases, as illustrated in the upper right figure for the B-L relation.

5.4.3 Comparison of effective permittivity from sintered and Platonic foams

The effective permittivities obtained from the electromagnetic wave propagation simulations for the Platonic and sintered foams are shown in Figure 5.10. Note that the models do not have the same porosities due to the different methods that were used to obtain both the sintered and Platonic foams.
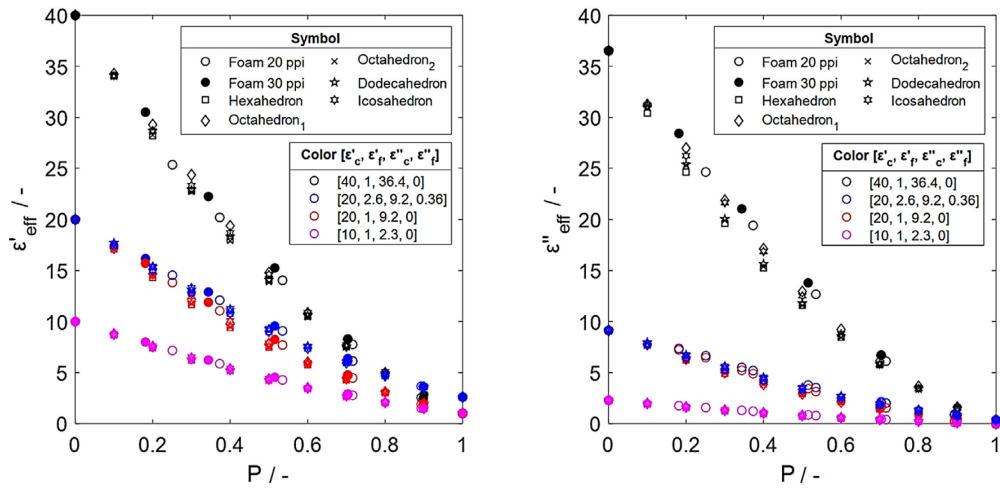
Figure 5.10. Estimated effective dielectric constants (left) and effective dielectric losses (right) from numerical calculations for sintered and Platonic foams. The mixtures of the foams are identified by their corresponding properties (ε_c', ε_f', ε_c'', ε_f'').

In general, the difference in ε_{eff}' and ε_{eff}'' for each foam is observed as a result of their different microstructures. Consequently, the microstructures of the Platonic foams that better represent sintered foams, would provide more accurate estimates of ε_{eff}. The effect of the different Platonic skeletons can be analyzed by comparing their susceptibility ratios as shown in Figure 5.11.
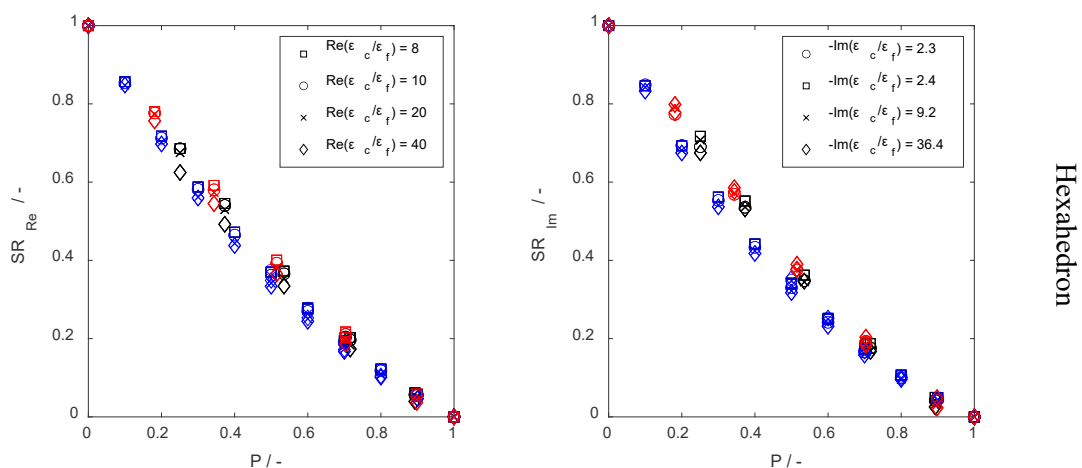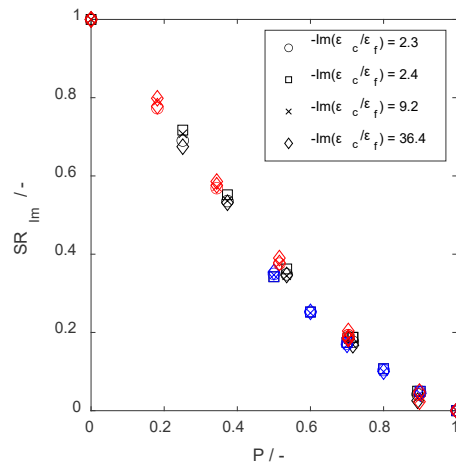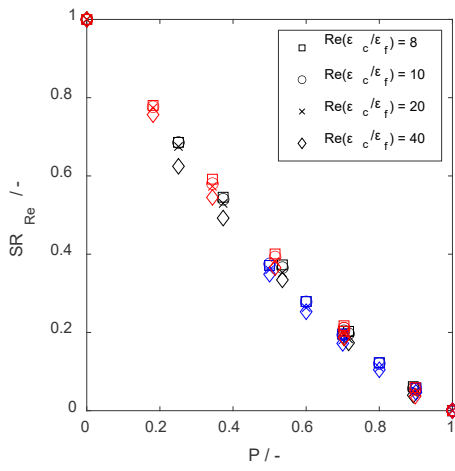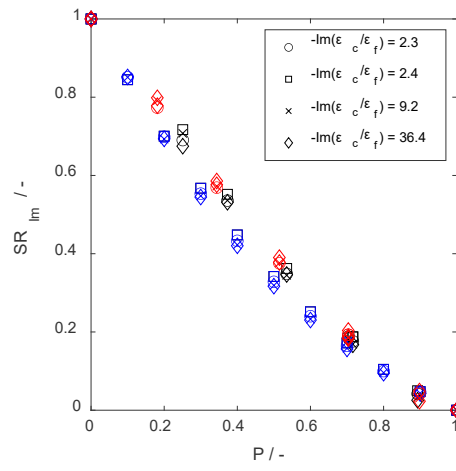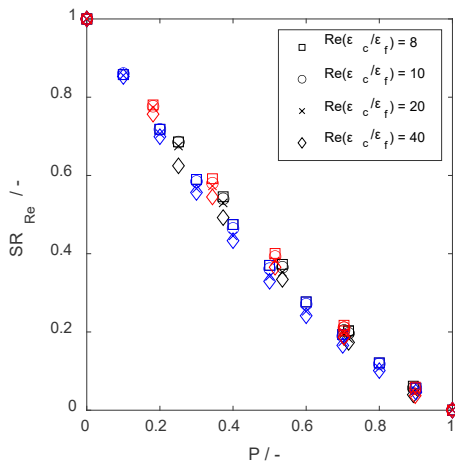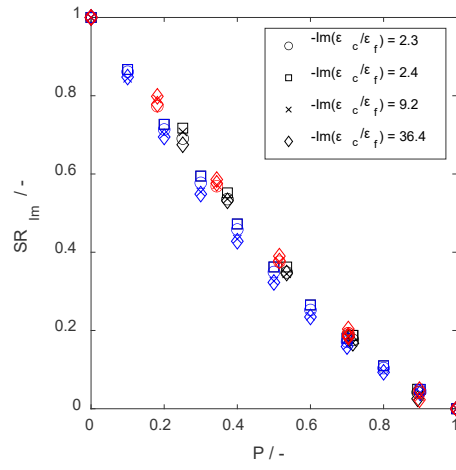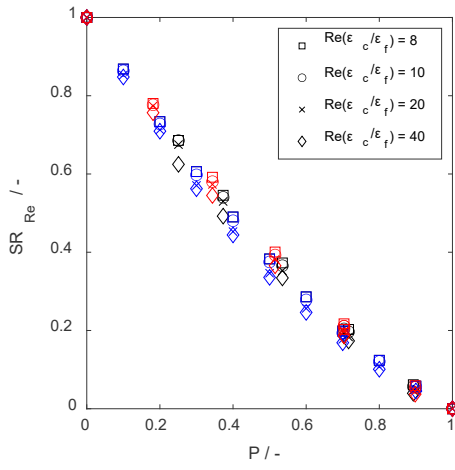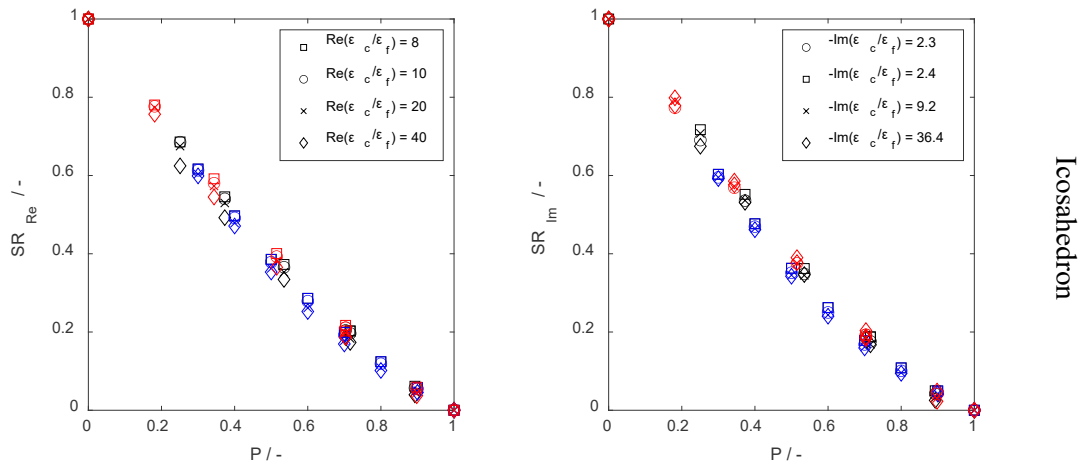
Figure 5.11. Real (left) and imaginary (right) susceptibility ratios from the numerical simulations of the Platonic foams (blue symbols) compared with the numerical simulations for the sintered foams at 20 ppi (black symbols) and 30 ppi (red symbols).

The effect of the various Platonic solids that were used as building elements for the open-cell skeletal structures is small. However, a general order can be observed for the dielectric loss, i.e., octahedron$_1$ > icosahedron > dodecahedron > octahedron$_2$ > hexahedron. This coincides with the order in which the Platonic shapes are preserved as indicated in Table 5.3, i.e., there is a decrease in the size of the faces of the open cells of the Platonic solids by increasing the struts. This suggests that as the open-cell faces become more closed, the resistivity decreases and, in turn, the loss increases.

5.5 Deriving a permittivity mixture-relation for Platonic foams

A mixing relation is proposed for estimating ε_eff of Platonic foams based on the analysis of their permittivities. The amplitude of the polarizability of a single scatterer dipole is

$$\alpha = p_\text{dip}/E \ , \tag{68}$$

where p_dip is the induced dipole moment of a single inclusion in a uniform local electric field with magnitude E. Previous calculations [71, 72] showed that for inclusions with minimal symmetry defects, such as for the Platonic solids, their α is a simple dyadic, which is obtained by solving its electrostatic field. Note that for non-zero dielectric loss ($\varepsilon'' \neq 0$), the polarizability must be represented as a complex number. Physically, the described phenomenon can occur in an oscillating electric field, such as microwaves, and is characterized by a damping velocity response (relaxation time [124]) of the induced dipole moment. This methodology is accurate but requires significant numerical effort for complex geometries such as the Platonic foams. Thus, it was better to start from the macroscopic domain, assuming that the loss mechanism is identical in both bulk and foam materials and sought a complex-valued correlation parameter g that contains the topological details of the micro-geometry. As g represents the topology, it is formulated in terms of the volume fraction of the skeleton $(1 - P)$

and fluid (P), as well as the effective and bulk permittivities. Observe that at $P < 0.5$ the fluid corresponds to the inclusion medium and the skeleton to the guest medium, and vice versa at $P > 0.5$. Accordingly, the parameter g for ceramic and fluid properties was proposed as

$$g = [\alpha_c \quad \alpha_f] \cdot \begin{bmatrix} \beta_c \\ \beta_f \end{bmatrix}, \tag{69}$$

where α_c, α_f and β_c, β_f are variable expressions in terms of the permittivity and volume fraction of the ceramic and fluid phases, respectively. The following expressions were proposed to assess α_c, α_f, β_c, β_f as

$$\alpha_c = \frac{q_0 \varepsilon_{eff} + q_2 \varepsilon_c}{q_4 \varepsilon_c + q_5 \varepsilon_f}, \tag{70}$$

$$\beta_c = \frac{\sum_{u=n_1}^{m_1} q_6 (1-P)^u}{\sum_{k=n_3}^{m_3} q_8 (1-P)^k + \sum_{j=n_4}^{m_4} q_9 P^j}, \tag{71}$$

$$\alpha_f = \frac{q_1 \varepsilon_{eff} + q_3 \varepsilon_f}{q_4 \varepsilon_c + q_5 \varepsilon_f}, \tag{72}$$

$$\beta_f = \frac{\sum_{j=n_2}^{m_2} q_7 P^j}{\sum_{k=n_5}^{m_3} q_8 (1-P)^k + \sum_{j=n_4}^{m_4} q_9 P^j}, \tag{73}$$

where all q-parameters are positive integers. At the porosity limits $P = 0$ and $P = 1$, the material corresponds completely to the ceramic and the fluid, which have no microstructure, that is $g = 0$. The numerator was selected to comply with the natural bounds $\varepsilon_{eff}(P = 0) = \varepsilon_c$ and $\varepsilon_{eff}(P = 1) = \varepsilon_f$ by setting $q_0 = -q_2$, $q_1 = -q_3$, $n_1 \neq 0$ and $n_2 \neq 0$, while the denominators are evaluated with any combination of bulk permittivities and volume fractions. For each set of parameters, several relation equations were deduced, in which g is given as a complex expression defined as

$$g(P, \varepsilon_c, \varepsilon_f) = g' - jg''. \tag{74}$$

For isotropic materials, g must be proportionally dependent on the permittivities of the mixture. On this basis, a selection condition was defined for the mixing relation giving a linear dependence of g to the permittivity contrast as

$$g' = \text{Re}\left(\frac{\varepsilon_c}{\varepsilon_f}\right) g'_m + g'_0, \tag{75}$$

$$g'' = -\text{Im}\left(\frac{\varepsilon_c}{\varepsilon_f}\right) g''_m - g''_0, \tag{76}$$

where g_0', g_0'' are the g values when $\varepsilon_c/\varepsilon_f \to 0$ and g_m' and g_m'' are the slopes. Next, an evaluation routine was set up using MATLAB (R2020a from Mathworks). After some iterations using $k \le 2$ and $j \le 2$ (due to limitations in computational resources), an expression was obtained, which satisfies the selection condition of linearity ($R^2 > 0.99$, see Figure 5.12) and is given as

$$g = \begin{bmatrix} \dfrac{(\varepsilon_{\text{eff}} - \varepsilon_c)}{\varepsilon_f} & \dfrac{(\varepsilon_{\text{eff}} - \varepsilon_f)}{\varepsilon_f} \end{bmatrix} \cdot \begin{bmatrix} \dfrac{(1-P)^2}{((1-P)^2 + 2P)} \\ \dfrac{2P}{((1-P)^2 + 2P)} \end{bmatrix}. \tag{77}$$

The equation can be rewritten as

$$g = \frac{1}{\varepsilon_f}\left[\frac{2P}{(1+P^2)}(\varepsilon_c - \varepsilon_f) - (\varepsilon_c - \varepsilon_{\text{eff}}) \right] \text{ or} \tag{78}$$

$$\varepsilon_{\text{eff}} = \frac{-2P}{(1+P^2)}(\varepsilon_c - \varepsilon_f) + (\varepsilon_c + g\varepsilon_f). \tag{79}$$

Then, substituting Equation 74, 75 and 76 into Equation 79 gives

$$\varepsilon_{\text{eff}} = \frac{-2P}{(1+P^2)}(\varepsilon_c - \varepsilon_f) + \varepsilon_f\big[[\text{Re}(\varepsilon_c/\varepsilon_f)g_m' + g_0'] + j[\text{Im}(\varepsilon_c/\varepsilon_f)g_m'' + g_0'']\big] + \varepsilon_c. \tag{80}$$
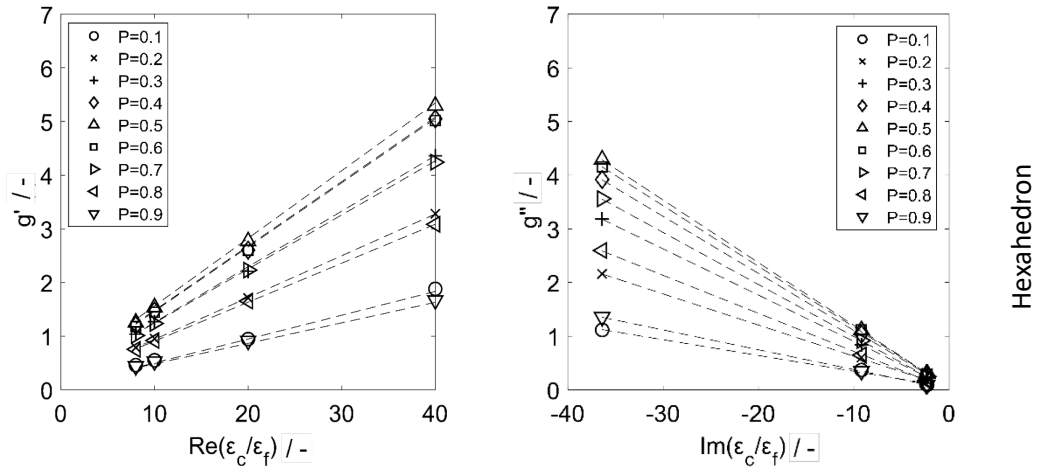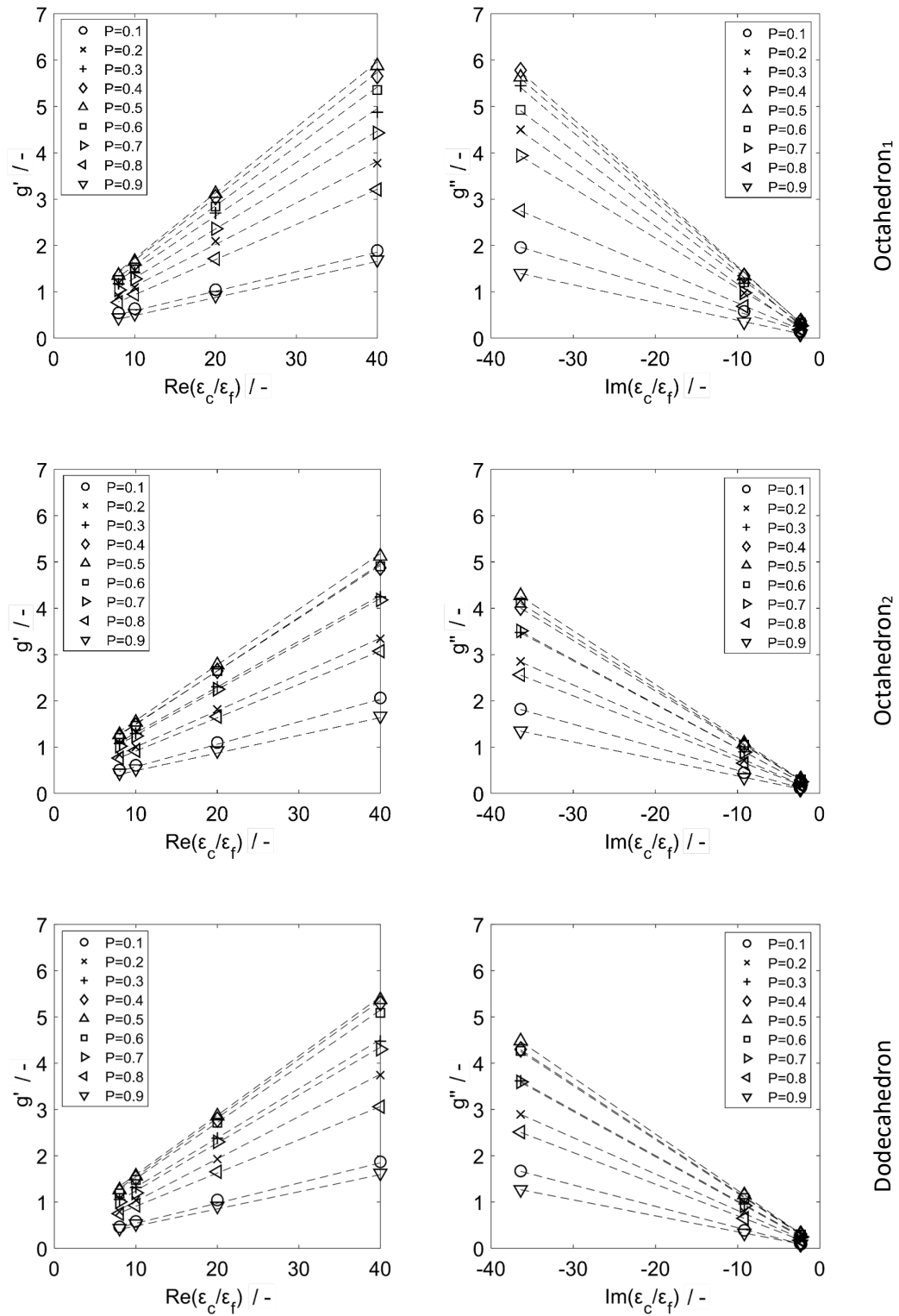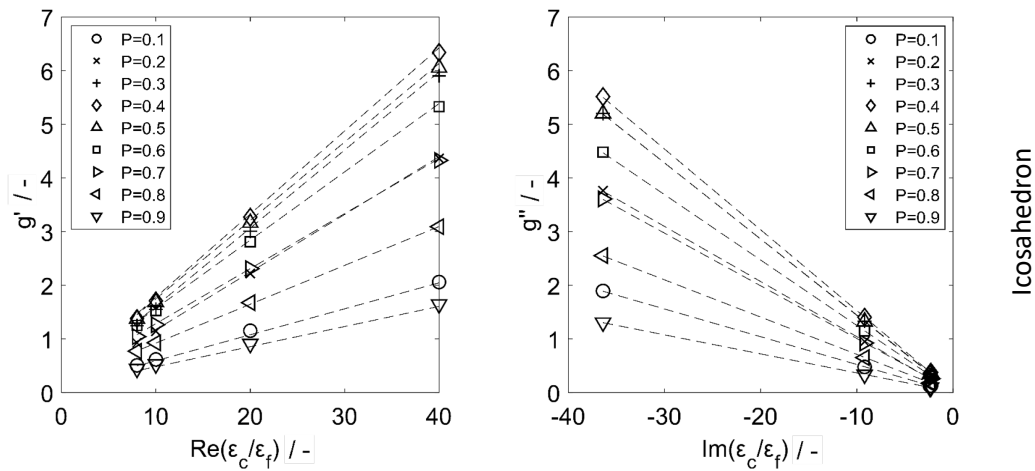
Figure 5.12. Complex-valued correlation parameter g of the Platonic foams vs. complex permittivity contrast ratio (all linear regressions are $R^2 > 0.99$).

In Figure 5.12, it is observed that none of the Platonic foams has a symmetrical inclusion–background morphology, i.e., $\text{Re}(g(P)) \neq \text{Re}(g(1-P))$. Best symmetry is obtained for the hexahedron skeleton, where the morphology of the skeleton only differs due to the cylindrical struts. Note that full symmetry is expected for symmetrical elements such as rectangular struts.

Platonic foams differ from common EMA inclusions such as spheres and ellipsoids because their microstructure changes with porosity, arising from geometric interference between their skeleton elements, particularly at the joints. Therefore, the topology-related parameters g_0', g_0'', g_m' and g_m'', are subject to variation with changing the porosity. The polynomial equation of degree 6 can effectively describe these parameters over the entire porosity range $P \in [0,1]$ as

$$Y = \sum_{k=1}^{6} a_k P^k , \qquad (81)$$

where Y represents any of the variables g_0', g_0'', g_m' or g_m''. Coefficients a_k are summarized in Table 5.4. Equation 80, referred to as Platonic relation, is only applicable within the range of porosity where the Platonic structure is preserved (refer to Table 5.3). Figure 5.13 shows ε_{eff} estimated using Equation 80, which represents a fair agreement with the Platonic foam calculations.

Table 5.4. Parameters used to calculate g_0', g_0'', g_m' and g_0''.

Variable	a_1	a_2	a_3	a_4	a_5	a_6
			Hexahedron			
g'_m	0.5229	−0.9951	2.4460	−4.7673	3.9566	−1.1630
g_0'	0.2775	4.7271	−14.1449	15.0204	−6.6742	0.7939
g_m''	0.2889	−0.0356	0.8263	-3.3594	3.3200	−1.0402
g_0''	−1.2278	10.1408	−36.4260	63.3016	−52.0799	16.2911
			Octahedron$_1$			
g_m'	0.4008	0.6699	−3.2970	3.9169	−2.2435	0.5528
g_0'	2.1613	−7.0162	17.1386	−28.2326	23.5875	−7.6392
g_m''	0.3209	4.0884	−19.4308	33.9140	−27.2604	8.3683
g_0''	−2.0185	26.2707	−105.0485	185.5296	−151.8010	47.0699
			Octahedron$_2$			
g_m'	0.6546	−2.1904	6.0160	−9.7020	7.2485	−2.0266
g_0'	0.3698	7.6377	−26.3063	34.1470	−20.6464	4.7987
g_m''	0.7183	−2.8553	8.1037	−12.6555	9.2101	−2.5214
g_0''	0.1978	−2.4611	7.5172	−10.0237	6.2255	−1.4557
			Dodecahedron			
g_m'	0.4617	0.3546	−3.9082	7.6496	−7.0236	2.4661
g_0'	1.4799	−10.1720	50.1347	−109.2526	103.7717	−35.9641
g_m''	0.6052	−1.7991	4.9208	−8.1320	5.9922	−1.5869
g_0''	0.1169	−3.0237	12.1921	−20.3098	15.4249	−4.4004
			Icosahedron			
g_m'	0.2213	4.1649	−17.8917	29.0420	−21.8497	6.3132
g_0'	2.4320	−21.2239	84.7916	−152.1911	124.4845	−38.2943
g_m''	0.3270	2.8913	−12.9887	20.3933	−14.6653	4.0423
g_0''	−0.1270	0.6904	−2.6267	4.5291	−3.4173	0.9512
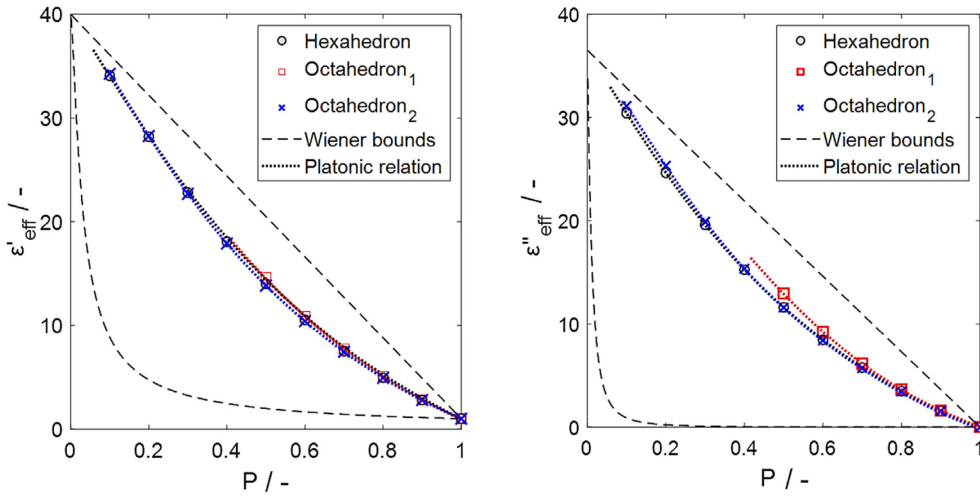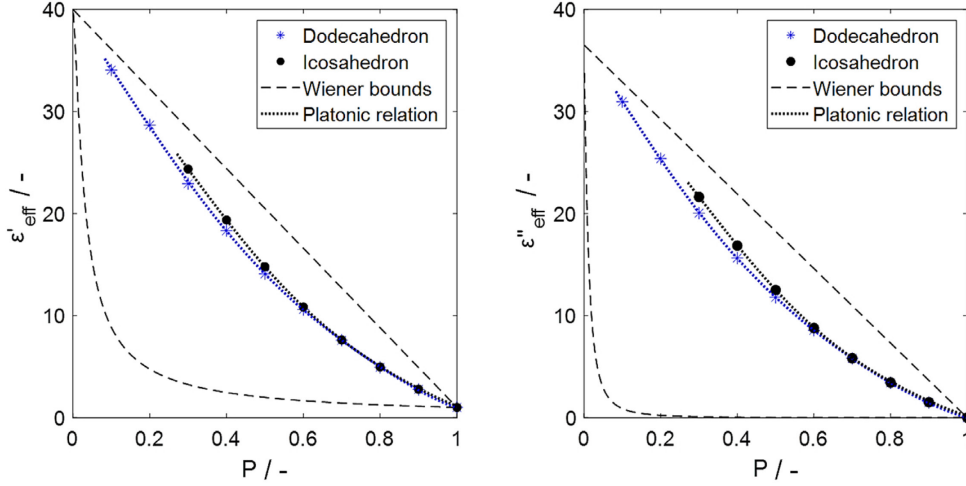
Figure 5.13. Effective dielectric constants (left) and losses (right) obtained from simulations for the Platonic foams. Dotted lines were obtained using Platonic relation (Equation 80). Dashed lines represent the Wiener bounds, $\varepsilon_c = 40.00 - j36.53$, $\varepsilon_f = 1.00 - j0.00$.

5.6 Extending the proposed permittivity mixture relation for sintered foams

Although the new relation was obtained directly from the analysis of the Platonic foam data, it also presents a linear relation between g and $\varepsilon_c/\varepsilon_f$ for sintered foams. However, in contrast to the Platonic foams, the real and imaginary parts of $g(P, \varepsilon_c, \varepsilon_f)$ for the sintered foams are well approximated by a simplified expression as

$$g(P, \varepsilon_c, \varepsilon_f) = (\varepsilon_c/\varepsilon_f)P(1 - P)^{3/2} . \tag{82}$$

Then, substituting Equation 82 into Equation 79 gives

$$\varepsilon_{\text{eff}} = \frac{-2P}{(1 + P^2)}(\varepsilon_c - \varepsilon_f) + \varepsilon_c\left(1 + P(1 - P)^{3/2}\right). \tag{83}$$

Note, that Equation 83 will be referred to as the open-cell foam (OCF) relation since it estimates the effective permittivity of the open-cell foam models.

5.7 Analysis of proposed relations for the estimation of the permittivity of Platonic and sintered foams.

Figure 5.14 shows the susceptibility ratios of the estimated effective permittivity for the sintered foams (marked with symbols) compared to that obtained using the OCF relation (continuous data shown by lines), including the $\overline{\text{RMSE}}$. Figure 5.14 illustrates the agreement between the data that were obtained from the simulations and relations. The OCF relation yields an ε_{eff} that surpasses the estimations obtained through the DEM relation ($\overline{\text{RMSE}}_{\text{OCF}} < \overline{\text{RMSE}}_{\text{DEM}}$) and other EMA or Platonic relations, as illustrated in Figure 5.11.
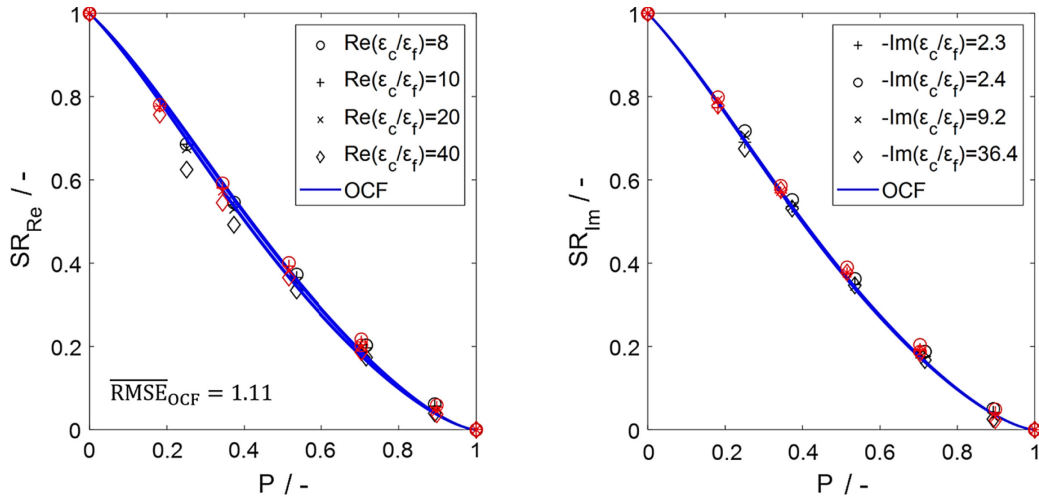
Figure 5.14. Real (left) and imaginary (right) susceptibility ratios of the OCF relation compared with the calculated ratios from the numerical simulations for sintered foams for 20 ppi (black symbols) and 30 ppi (red symbols).

The OCF and Platonic relations were also compared with the experimental data. However, the data in the literature are scarce and no records for the variation of the porosity and ε_{eff} are available for open-cell foams under conditions of constant temperature and incident radiation frequency. Thus, a series of previous ε_{eff} measurements of 30, 40 and 60 ppi cordierite samples at 2.45 GHz using the cavity perturbation technique [125] and polyurethane with different moisture content were used for evaluation. Figures 5.15 and 5.16 depict the effective permittivity of cordierite and polyurethane along with the dodecahedron Platonic, OCF, M-G, and DEM estimations. The Platonic dodecahedron was chosen over the other Platonic relations due to its high level of agreement with the numerical results of the sintered foams.
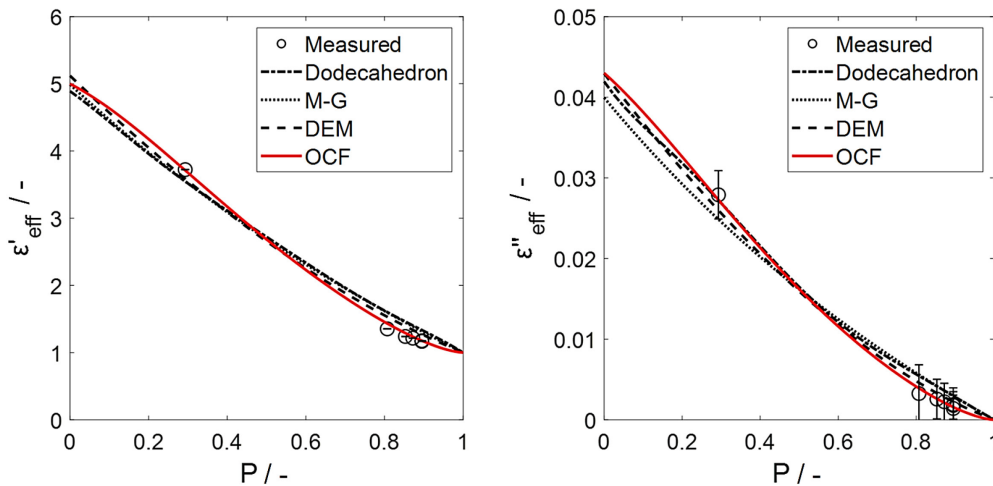
Figure 5.15. Effective dielectric constants (left) and effective dielectric losses (right) of cordierite foam samples and estimates using dodecahedron, OCF, MG, and DEM relations.
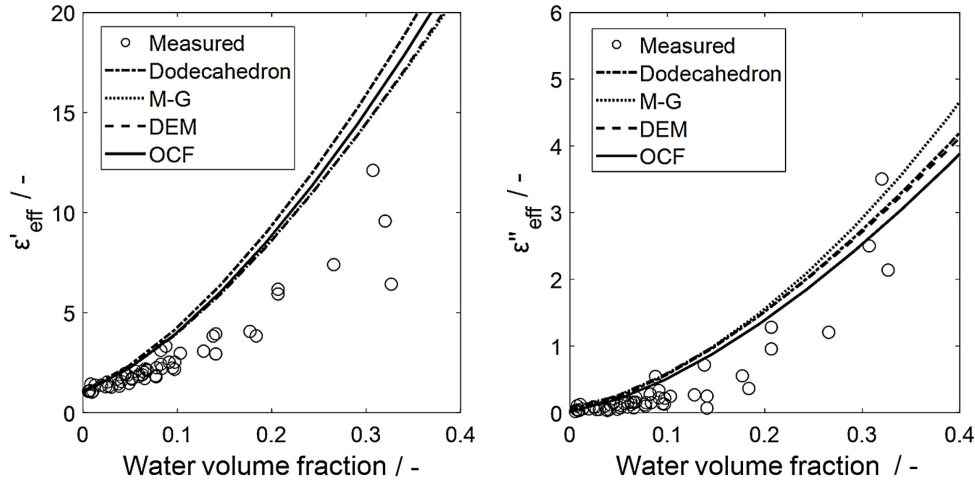
Figure 5.16. Effective dielectric constants (left) and effective dielectric losses (right) of polyurethane foam samples and estimates using dodecahedron, OCF, M-G, and DEM relations.

In Figure 5.15, ε_c is obtained from the mixing relations that were fitted to the experimental data using an iterative least-squares estimation. The dodecahedron, M-G and DEM relations show similar estimates but do also have a remarkably different trend compared with the OCF relation. This is due to the different approaches used by relations to describe the microstructure of the foams. According to the literature, the bulk permittivity of cordierite ranges from a minimum of $\varepsilon_{cord,min} = 4.77 - j0.008$ (at $P = 0$, 20 °C and 8.52 GHz [126]) to a maximum of $\varepsilon_{cord,max} = 6 - j0.06$ (at $P = 0$, 20 °C and 1 MHz [127]). All of the relations provide an acceptable estimate of $5 - j0.04 \pm 0.2 - j0.004$ within the cordierite bulk permittivity range assuming that this range remains practically constant at 100 °C and 2.45 GHz.

Figure 5.16 shows ε_{eff} of the polyurethane samples with $P = 0.978 \pm 0.007$, which were adjusted with different water volume fractions. $\varepsilon_{moisture}$ were calculated using the DEM relation at 2.45 GHz by setting $\varepsilon_{air} = 1.00 - j0.00$ and $\varepsilon_{water} = 80.36 - j14.57$ [128]. Subsequently, $\varepsilon_{moisture}$ and $\varepsilon_{polyurethane} = 2.0 - j3.2$ [129], were utilized in the mixing relations to calculate ε_{eff}. For polyurethane foams, the mixing relations were not applied to estimate ε_c, resulting in a distinct trend in the relations observed. The employed mixture relations show consistent agreement with each other. However, the discrepancies with the experimental data may be attributed to the non-uniform distribution of water within the foam voids, as well as the high moisture adsorption characteristics of highly polar polymers such as polyurethane [130]. Both factors in combination produce a significant variation to an EMA mixture, whereby overestimated values for the effective permittivity are expected. Moreover, at a porosity of $P = 0.97$, ε_{eff} depends more on moisture rather than on morphology. Finally, it can be concluded that OCF relations provide good estimates that are comparable to those from the EMA relations for ε_{eff}.

5.8 Using the derived mixing relations for determining the effective thermal conductivity of open-cell foams

Cross-property relations, also known as multi-property relations, are frequently employed to correlate variations in effective values of various physical properties such as thermal conductivity, elastic moduli, electrical conductivity, and fluid permeability [74, 131-134]. However, due to microstructural features, such as pores and inclusions in heterogeneous materials, determining effective properties is more complex than simply applying a volumetric mean-weighted calculation. Predictive relations for ε_{eff}, k_{eff} or any cross-property are based on models describing the microstructure of heterogeneous materials. In particular, for estimating k_{eff} of open-cell foams, several relations can be found in the literature. These relations are mostly based on empirical data-fitting functions: e.g. Calmidi relation [134], geometrical models: e.g. Bracconi, Dai and Yao relations [135-137], probability distributions of parallel and series models: e.g. weighted arithmetic mean relation [73], and those based on EMA assumptions such as the Maxwell-type and self-consistent models, e.g. Differential Effective Medium relation [73, 138].

The analogy of thermal and electrical networks can also be applied to the pore network of open-cell foams [135, 139]. According to this analogy, it is reasonable to assume that any relation describing ε_{eff} can be used to estimate k_{eff}, or vice versa [73, 74, 134, 138]. Please note that k_{eff} only considers thermal conductivities and not convective heat transfer coefficients. Following the thermal-electrical analogy, both derived Platonic and OCF relations can be used to estimate k_{eff}. In case of estimating k_{eff}, the Platonic relation is given as

$$k_{\text{eff}} = \frac{-2P}{(1 + P^2)}(k_{\text{s}} - k_{\text{f}}) + (k_{\text{s}} + gk_{\text{f}}) \, , \qquad (84)$$

where k_{s} and k_{f} are the thermal conductivities of the bulk materials, i.e. the solid skeleton and the medium that fills the voids of the skeleton, respectively. When dealing with complex-valued quantities, such as $\varepsilon_{\text{eff}} = \varepsilon'_{\text{eff}} - j\varepsilon''_{\text{eff}}$, the calculation of g also results in a complex-valued quantity $g = f(g'_{\text{m}}, -jg''_{\text{m}}, g'_0, -jg''_0)$. Unlike ε_{eff}, both k_{eff} and the derived function g are real-valued quantities. As a result, g is calculated as

$$g = g'_{\text{m}}(k_{\text{s}}/k_{\text{f}}) + g'_0 \, , \qquad (85)$$

where g'_{m} and g'_0 are given by Equation 81. Moreover, the corresponding relation for estimating k_{eff} using the OCF relation is

$$k_{\text{eff}} = \frac{-2P}{(1 + P^2)}(k_{\text{s}} - k_{\text{f}}) + k_{\text{s}}\big(1 + P(1 - P)^{3/2}\big) \, . \qquad (86)$$

Predictions for k_{eff} of open-cell foams using Platonic and OCF relations, as well as predictions from selected literature relations, are compared with experimental and numerical data. State-of-the-art k_{eff} relations [73, 134-141] considered in this study are summarized in Table 5.5. They were selected because of their excellent prediction capability [133-142]. Tables 5.6 and

5.7 summarize k_{eff} of skeleton materials and filling medium, as well as the thermal conductivity contrast of selected literature open-cell foams data [134, 137, 138, 140, 142-147].

Table 5.5. Mixing relations applied for estimating the effective thermal conductivity of open-cell foams.

Relation	Expression	Remarks
Bracconi [134]	$k_{\text{eff}} = k_s\left(\dfrac{2}{3}(1-P)^2 + \dfrac{1}{3}(1-P)\right)$	This relation ignores k_f because it was derived from a correlation for the tortuosity in periodically ordered structures, which is defined by the skeleton structure only.
Weighted arithmetic mean (WAM) [73]	$k_{\text{eff}} = \Psi_{\text{arithm}}\left(Pk_f + (1-P)k_s\right) + \dfrac{1-\Psi_{\text{arithm}}}{\left(\dfrac{P}{k_f} + \dfrac{1-P}{k_s}\right)}$	Weighted arithmetic mean of the Wiener bounds using 1. $\Psi_{\text{arithm}} = 0.35$ as proposed by Bhattacharya et. Al [141] 2. $\Psi_{\text{arithm}} = 0.49$ as proposed by Dietrich et. Al [140]
Calmidi [134]	$k_{\text{eff}} = k_f P + k_s 0.181(1-P)^{0.763}$	
Dai [136]	$k_{\text{eff}} = \dfrac{\sqrt{2}}{2(R_A + R_B + R_C + R_D)}$	$R_A = \dfrac{4d}{\left(2e^2 + \pi d(1-e)\right)(k_s - k_f) + 4k_f}$ $R_B = \dfrac{(e-2d)}{e^2(k_s - k_f) + 2k_f}$ $R_C = \dfrac{2(\sqrt{2} - 2e)}{\pi d^2\sqrt{2}(k_s - 2k_f) + 2k_f}$ $R_D = \dfrac{2e}{e^2(k_s - k_f) + 4k_f}$ $d = \sqrt{\dfrac{\left(\sqrt{8}(1-P) - \dfrac{3e^3}{2}\right)}{\pi\left(3 - e(\sqrt{32} + 1)\right)}}$ $e = 0.198$
Differential Effective Medium (DEM) [138]	$\dfrac{k_f - k_{\text{eff}}}{k_f - k_s}\left(\dfrac{k_s}{k_{\text{eff}}}\right)^{1/3} = 1 - P$	Also known as the Bruggeman relation, non-symmetric.
Yao [137]	$k_{\text{eff}} = \dfrac{1}{(\lambda/k_E + (1-2\lambda)/k_F + \lambda/k_G)}$	$k_E = \dfrac{\sqrt{2}}{6}\pi\lambda(3 - 4\lambda)\dfrac{1+b^2}{b^2}(k_s - k_f) + k_f$ $k_F = \dfrac{\sqrt{2}}{6}\pi\lambda^2\dfrac{1+b^2}{b^2}\left(\dfrac{k_s}{2} - k_f\right) + k_f$ $k_G = \dfrac{\sqrt{2}}{6}\pi\lambda^2\dfrac{1+b^2}{b^2}(k_s - k_f) + k_f$ λ is calculated (implicit method) from $P = 1 - \dfrac{\sqrt{2}}{2}\pi\lambda^2(3 - 5\lambda)\dfrac{1+b^2}{b^2}$, where a is a geometrical parameter ($b = 2.01$ as recommended by Yao et al. [137]).

Table 5.6. Thermal conductivities of filling media and skeleton bulk materials (*average value).

Skeleton material	k_s / Wm^{-1}K^{-1}	Filling medium	k_f / Wm^{-1}K^{-1}
Aluminum [134]	218	Air [137]	0.0265
Alumina [140]	25.9	Paraffin [137]	0.305
AlSi$_7$ [138]	167	Vacuum* [146]	0.003
Copper [137]	401	Water [137]	0.613
FeCr-alloy [151]	16		
Mullite [140]	4.4		
Nickel [148]	91.4		
OBSiC [140]	8.1		
Stainless steel (SS) [142]	15		
Zirconia [151]	2.5		
Polyurethane (PU) [142]	0.2		

Table 5.7. List of references with published k_{eff} values for different skeleton and filling media combinations and corresponding thermal conductivity contrast values.

Skeleton – Fluid	k_s/k_f	Skeleton – Fluid	k_s/k_f
Al–Air [134, 142-145]	8.2×10^3	Nickel–Air [142]	3.4×10^3
Al–Water [134, 142-145]	355.6	Nickel–Water [142]	149.1
Al–Paraffin [142]	714.7	Nickel–Paraffin [142]	299.7
Al–Vacuum [146, 147]	7.3×10^4	Polyurethane–Air [142]	7.5
Alumina–Air [140]	977.4	Polyurethane–Water [142]	0.3
AlSi7–Air [138]	6.3×10^3	Polyurethane–Paraffin [142]	0.7
Cu–Air [137, 142]	1.5×10^4	OBSiC–Air [140]	305.7
Cu–Paraffin [138, 145, 148]	1.3×10^3	Stainless steel–Air [142]	566.0
Cu–Water [137, 142]	654.2	Stainless steel–Water [142]	24.5
FeCr-alloy–Air [149]	603.8	Stainless steel–Paraffin [142]	49.2
Mullite–Air [140, 149]	166.0	Zirconia–Air [149]	94.3

For easier data comparison k_{eff} of open-cell foams is normalized as

$$k'_{eff} = \frac{k_{eff} - k_f}{k_s - k_f} . \tag{87}$$

This way, all values are scaled between 0 to 1, allowing to describe k'_{eff} as a function of P, which depends on foam microstructure and thermal conductivity contrast. The difference between k_{eff} estimated from relations and those from experimental or simulated data is quantified by the RMSE metric.

Figure 5.17 shows the normalized k'_{eff} data (symbols) found in the literature for open-cell foams against estimations (lines) using the literature mixing relations (upper subfigures), the Platonic relations (lower subfigures) and the OCF relation (lower-right subfigure). As k_s/k_f increases, k'_{eff} decreases for both experimental data and estimates from relations, as illustrated in the upper right subfigure for the prediction of the Dai relation [136]. In addition, Table 5.8 summarizes the RMSE for each relation at three different porosity ranges ([0.5, 1.0], [0.85, 1.0], and [0.9, 1.0]), to characterize the deviation from the experimental data.
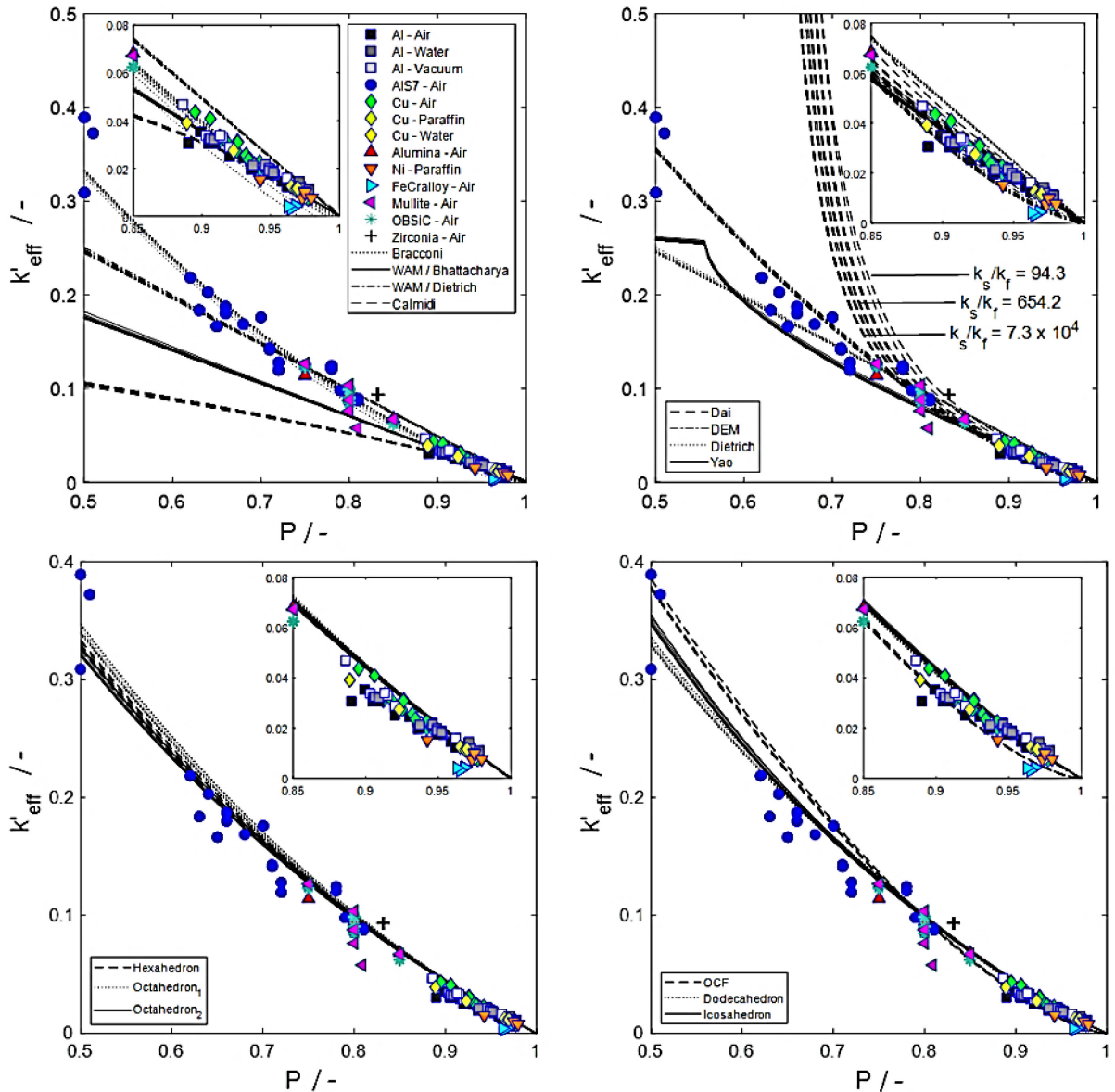
Figure 5.17. Normalized experimental k'_{eff} values (represented by symbols corresponding to foams listed in Table 5.7) compared with those estimated from relations (represented by lines corresponding to relations listed in Table 5.5 and Equations 84 and 86). The embedded subplots provide an enlarged view for the porosity ranging from 0.85 to 1.0.

Table 5.8. Comparison of the RMSE for k'_{eff} of the considered relations (*weighted arithmetic mean approach proposed by Bhattacharya or Dietrich [140,141], see remarks in Table 5.5).

Relation	RMSE		
	$P \geq 0.50$	$P \geq 0.85$	$P \geq 0.90$
Bracconi	1.55	0.78	0.68
Calmidi	7.80	0.98	0.81
Dai	84.05	0.80	0.73
DEM	2.10	1.77	1.72
WAM / Bhattacharya*	5.38	0.68	0.58
WAM / Dietrich*	3.58	2.32	2.13
Yao	3.02	0.62	0.53

Hexahedron	1.85	1.29	1.14
Octahedron$_1$	1.89	1.34	1.18
Octahedron$_2$	1.90	1.32	1.18
Dodecahedron	1.65	0.87	0.73
Icosahedron	1.67	1.07	0.92
OCF	2.30	1.55	1.52

Figure 5.17 (upper row) illustrates that the literature relations estimate k'_{eff} better for P → 1, and this is expected because they were preferably developed for foams with higher porosity. The best predictions are obtained by the relation from Bracconi, as seen from Table 4.11. However, it should be mentioned that the Bracconi relation accuracy decreases as k_f increases, since the relation does not include a k_f term.

The relations inspired by the Platonic solids (bottom row of Figure 5.17) provide excellent predictions with only minor deviations from the experimental data, as shown in Table 5.8. The results suggest that the dodecahedral structure (followed by the icosahedral) best mimics the skeleton of real foams. It is important to highlight that other researchers [136, 145] have proposed the Kelvin tetrakaidekahedron as the best geometrical element to mimic foams. The Kelvin tetrakaidekahedron is known to reproduce packings with low surface area. However, the modelling of this polyhedron has been performed only in two dimensions, using ligaments corresponding to struts and thus lacks important features, such as the effect of the geometrical shape of joints. Accordingly, a better description of tetrakaidekahedron-inspired foams would be required for a fair comparison with the dodecahedral and the icosahedral relations from this study.

Figure 5.18 shows k_{eff} estimated from Bracconi [135] and dodecahedron and OCF relations compared with those reported from numerical simulations [142].
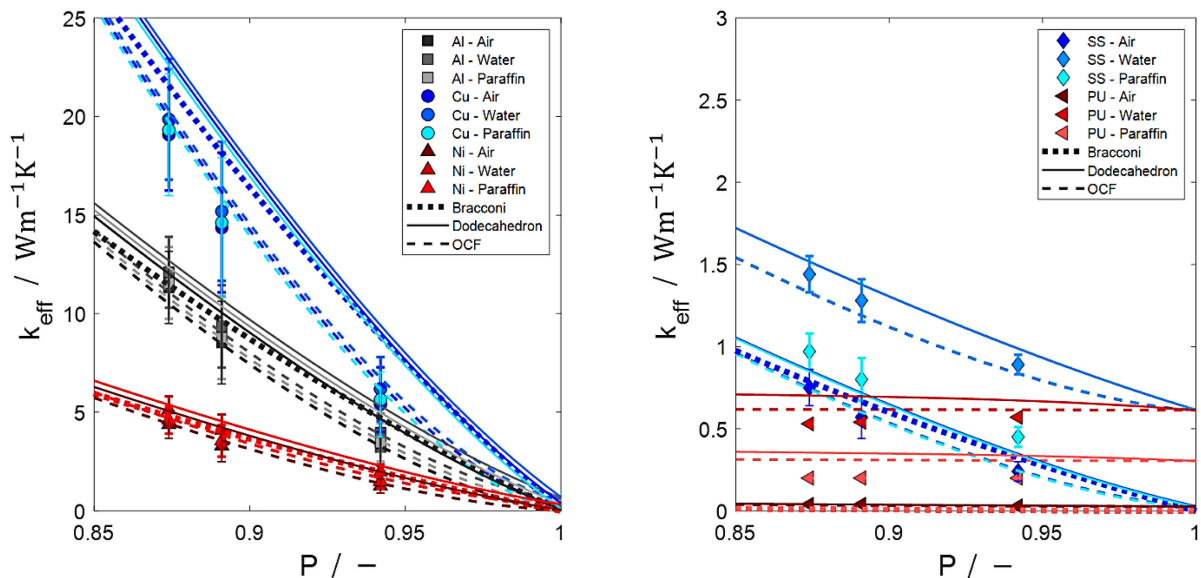
Figure 5.18. k_{eff} estimated from Bracconi, dodecahedron and OCF relations compared with those from numerical simulations Al, Cu and Ni foams (left) and SS and PU foams (right). The errors bars correspond to the standard deviation as reported by August et al. [142]. Lines from Bracconi's relation overlap, as it does not consider the filling medium.

Figure 5.18 reveals that, in contrast to the experimental values, the OCF relation yields the best predictions for the simulated data (RMSE$_{OCF}$ = 0.41 < RMSE$_{Bracconi}$ = 1.27 < RMSE$_{Dodecahedron}$ = 1.77). This is consistent with previous electromagnetic wave propagation calculations used for computing ε_{eff} (see Section 5.7) and with calculations via the diffuse interface representation of the phase-field model used for computing k_{eff} [142]. The structural models for computing ε_{eff} were reconstructed from tomographic scans of open-cell foams, while the structural models for computing k_{eff} correspond to synthetic foam structures generated by the algorithm proposed by August et al. [152]. Although the open-cell structural models used for the simulations are different, both are well represented by the OCF relation. Thus, it can be concluded that the simulation models are significantly different from real foams for the following reasons:

First, the morphology of the foam skeleton was reconstructed from µCT-scans of samples with a porosity range of 0.90 ± 0.01. This particular porosity value accurately represents both experimental and simulation results, which are in good agreement with the OCF relation (refer to Figures 5.17 and 5.18). However, as previously discussed in Section 5.1, using three-dimensional erosion and dilation filters to generate models of varying porosity may result in significant differences compared to the actual microstructure of foams. The extent of these differences will depend on the resolution of the mesh used in the process.

Second, the synthetic foam structures produced by August et al. [142] are not entirely identical morphologically, even though they have the same porosity. It has been observed that the numerically computed and experimentally measured values of k_{eff} as reported by August et al. [142] only match when the standard deviation is considered. This suggests that only a few synthetic structures exhibit morphological consistency with real-world foams.

5.9 Conclusion

In this chapter, numerical calculations of electromagnetic wave propagation were used to improve estimates of the effective permittivity of open-cell foams. Two model approaches were chosen for estimating the effective permittivity. One approach employed the foam morphology obtained through tomographic reconstruction, and the other approach used Platonic solids as building blocks of open-cell skeletal structures. A good agreement was observed between the foam models and those constructed from Platonic solids such as dodecahedrons. In addition, a new empirical relation was also proposed for estimating the effective permittivity of sintered foams. The relation was derived through an examination of the effective permittivity obtained from numerical simulations. The relation is only based on porosity, bulk material permittivities, and geometrical parameters depending on the model structure, i.e. Platonic building elements.

Comparisons with other literature mixing relations were performed by using cross-properties. Based on the thermal-electrical analogy, mixing relations used for estimating the effective permittivity can be used to estimate cross-properties, such as the effective thermal conductivity. The relations were compared with experimental and numerical data from the literature as well as with predictions from available mixing relations. It has been shown that the effective thermal conductivity of foams can be well estimated from the Platonic relation by using dodecahedrons building elements for the skeleton. The following recommendations can be derived from this work to properly select the most suitable relation (relations can be consulted from Table 5.5):

- For foams with porosities ranging from 0.5 to 1.0 and low bulk thermal conductivity or permittivity of the filling medium, the Bracconi relation [134] is recommended.

- Novel mixing relations are recommended for porosities ranging from 0.5 to 0.9, except for the Platonic relation based on dodecahedrons, which can be applied for porosities from 0.5 to 1.0. In addition, the Platonic relation based on dodecahedrons is recommended over the Bracconi relation [134] for thermal conductivity of the filling medium higher than 1 $Wm^{-1}K^{-1}$ and for the permittivity higher than 1.

- The relations of Yao [137] and the weighted arithmetic mean approach with the arithmetic coefficient proposed by Bhattacharya [141] are recommended if the porosity of the foam is higher than 0.85.

Finally, significant discrepancies were also observed between predicted values obtained from numerical simulations and those from experiments. In particular, it was identified that only a few of the synthetic structures are morphologically consistent with real foams. The variations are attributed to the fact that foams with varying porosities may exhibit distinct morphologies.

Chapter 6

Liquid evaporation using a microwave applicator: modeling and experimental investigation

This chapter discloses the model and design procedure performed to manufacture a compact microwave applicator, which is intended for mechanical droplet separation and in-situ evaporation by using microwave-assisted heated open-cell foams. The primary focus of the study was to experimentally investigate the effectiveness of the microwave applicator in removing liquid accumulations on fine droplet separators.

Parts of this chapter have been published in:

6.1 Governing equations and foams properties

Microwave design requires modelling microwave effects such as electromagnetic propagation and thermal heating. Electromagnetic propagation is considered by the Maxwell equations (see Equations 19-22), while thermal energy generated from the microwave energy density Q_{MW} is directly proportional to the square of the mean root electric field strength. The foam mixture composed of a gaseous medium, foam skeleton, and droplets is treated as an effective medium. Thus, Q_{MW} is given as

$$Q_{MW} = 0.5\omega\varepsilon''_{eff}\varepsilon_0 E^2 \, , \tag{88}$$

where ω is the angular frequency and V is the volume occupied by the open-cell foam. The system is conformed of a ceramic skeleton and a filling medium composed of droplets surrounded by the gas phase. The skeleton can be well described using the Topological Mixture Relation from Equation 80 and by considering dodecahedrons as the Platonic building elements. Assuming that droplets are spherical and homogeneously dispersed in the air or steam, the Maxwell–Garnett mixing relation provides good estimates of the filling permittivity ε_f for the droplet-laden or wet steam [153]. The Maxwell-Garnett relation for the filling medium is

$$\frac{\varepsilon_f - \varepsilon_g}{\varepsilon_f + 2\varepsilon_g} = \delta_d \left(\frac{\varepsilon_d - \varepsilon_g}{\varepsilon_d + 2\varepsilon_g} \right), \tag{89}$$

where ε_d and ε_g are the permittivities of droplets and gas, respectively, and δ_d is the droplet volume fraction, so that $\delta_d + \delta_g = 1$. The dielectric permittivity of the droplets is equal to that of water, which can be described by its molecular relaxation time using the Debye formula

$$\varepsilon_d = \varepsilon_\infty(T) + \frac{\varepsilon_{st}(T) - \varepsilon_\infty(T)}{1 - i\omega\tau(T)} \, , \tag{90}$$

where ε_{st} and ε_∞ are static (at zero frequency) and optical frequency (at an infinite frequency) permittivities, respectively, depending on temperature T, ω and the relaxation time τ. The Debye formula [154] is limited to 1 THz, covering the microwave frequency range. Figure 6.1 shows the permittivity of water from 2.4 to 2.5 GHz and 0 to 100 °C at 1 atm.
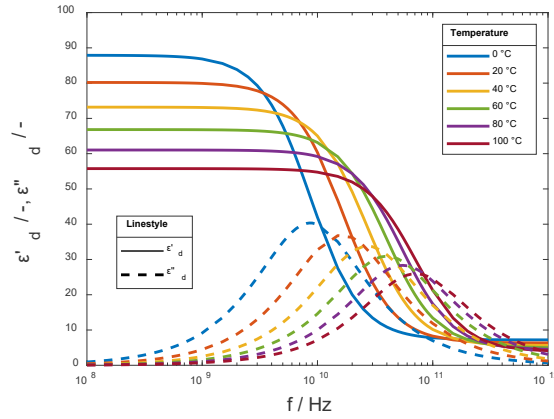
Figure 6.1. Pure water permittivity for $f = 1E8 - 1E14$ Hz and $T = 0 - 100$ °C generated by using the Debye formula [154].

Figure 6.1 shows that the permittivity of water decreases with increasing temperature, thus ε_d must consider the temperature. As the droplets evaporate, it would also be necessary to consider the effect of the dielectric properties of water vapor on ε_f. Yet, the dielectric constant of saturated water vapor, which is ~ 1.006 ($T = 373$ K and atmospheric pressure) is significantly lower than that of saturated liquid water, which is 55 [155, 156], due to its much lower density. Such a significant difference is relevant not only to the dielectric constant but also to the loss factor [157]. The permittivity of air and water vapor are comparable, and as a result, it is not necessary to differentiate between water vapor and air permittivities. The effective permittivity for foam porosities of 0.85, 0.90 and 0.95, and droplet volume fractions of 0.00, 0.05 and 0.10 is illustrated in Figure 6.2.
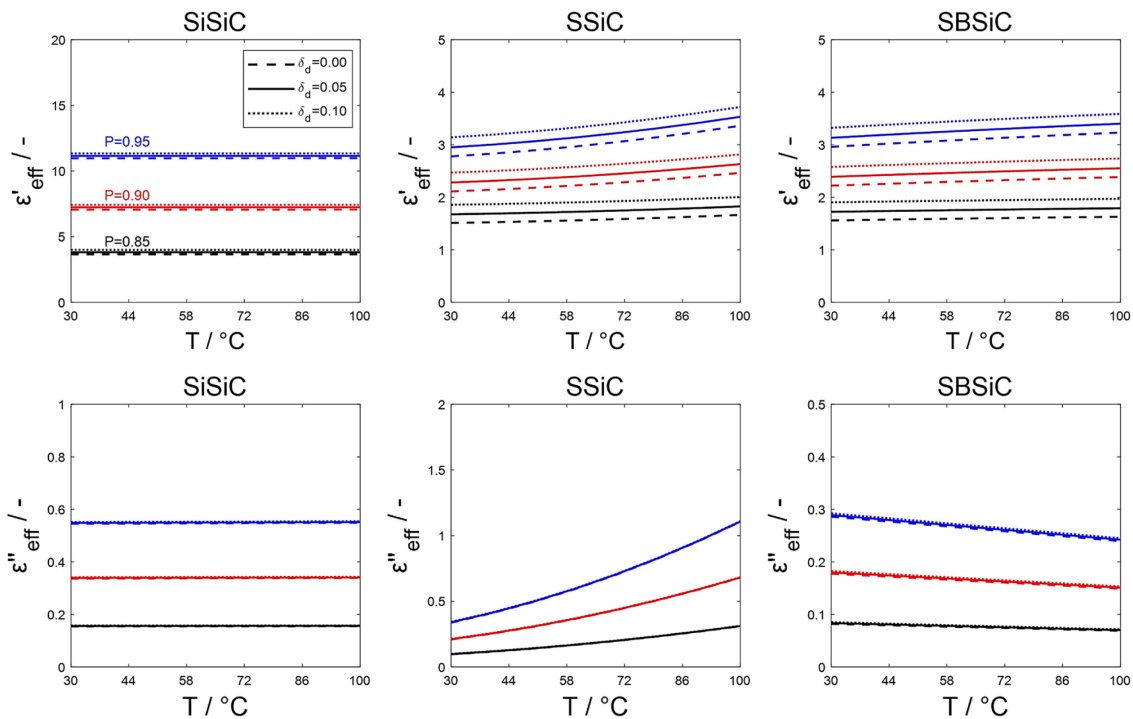
Figure 6.2. Effective permittivity of the system consisting of foam skeleton, air/steam and dispersed water droplets at a frequency of 2.45 GHz, estimated based on the average skeleton permittivity

(notation shown in the upper left subfigure holds for all subfigure).

Considering the SiSiC, SSiC and SBSiC foams as effective materials, the size of the inclusions must not exceed the maximum inclusion diameter calculated as $d_{icl} = X\lambda/(\pi\sqrt{\varepsilon'_{eff}})$. Using the threshold value $X = 0.15$ as suggested by Mishchenko et al. [70], along with the maximum value of ε'_{eff} ($P = 0.85$, $T = 100\,°C$, $\delta_d = 0.1$), the allowed maximum d_{icl} is 1.7 mm (SiSiC), 3.2 mm (SBSiC) and 3.1 mm (SSiC). These values exceed the largest cell size of the foams corresponding to 1.36 ± 0.17 mm. Note that only the average cell diameter was measured for SiSiC, however, due to the similarity with the skeleton of the other foams, their cell size is also expected to be similar.

The flow can be modeled as a single-phase flow since the droplet-laden stream is very dilute. Therefore, the equations of continuity and conservation of inertial momentum are given as

$$\nabla \cdot (\rho u) = 0 \,, \tag{91}$$

$$\frac{\partial u_g}{\partial t} + u_g \cdot \nabla u_g = -\frac{\nabla p}{\rho_g} + \frac{1}{\rho_g}\left(\mu_g \nabla^2 u_g + \frac{1}{3}\mu_g \nabla(\nabla \cdot u_g)\right) + g \tag{92}$$

For incompressible flows the density is constant in space and time, therefore, the conservation equation reduces to $\nabla \cdot u = 0$. While the conservation of momentum equation changes according to

$$\rho_g\left(\frac{\partial u_g}{\partial t} + (u_g \cdot \nabla)u_g\right) = -\nabla p + \mu_g \nabla^2 u_g + g\rho_g \,. \tag{93}$$

Since the SBSiC, SiSiC and SSiC foam samples were produced by replication technique using the same polymeric template, their skeletal structure is similar and they feature common pressure gradient and droplet residence time. The pressure gradient and residence time of droplets were taken from Chapter 3 using Equations 58 and 59, respectively. For Reynolds numbers higher than 4000, turbulence is computed using the k-ε turbulence model. Finally, the local thermal non-equilibrium (LTNE) model based on the volume averaging method is used to obtain the temperature distribution in the porous matrix. The LTNE model considers the energy equations for fluid and solid phases [158-160] as

$$G\left(P\frac{\partial T_f}{\partial t} + u_g \nabla \cdot T_f\right) = \nabla \cdot (k_f \cdot \nabla T_f)P + h_g(T_s - T_f) + PQ_{MW} + \rho_d M_d \delta_d \Delta H_{vap,d}\big|_{T_{boil}}, \tag{94}$$

$$(1-P)\rho_s C_{p,s}\frac{\partial T_s}{\partial t} + (1-P)\nabla \cdot (k_s \cdot \nabla T_s) + (1-P)Q_{MW} = h_g(T_s - T_f) \,, \tag{95}$$

where C_p is the heat capacity, k is the heat conductivity, h_g is the volumetric heat transfer coefficient (coupling Equation 94 and 95), T_{boil}, M_d and $\Delta H_{vap,d}$ are boiling temperature, molar mass and enthalpy of evaporation of the droplets, respectively. Using the correlation developed by Dietrich [159], h_g was calculated by incorporating the pressure gradient in open-cell ceramic foams. The correlation is valid for u_g ranging from 0.5 to 5 ms^{-1}. For the energy

equations, viscous dissipation and work done by pressure changes were assumed negligible. Moreover, an independent energy equation for the droplets was not considered, and instead, droplets were assumed to be in local thermal equilibrium with the gas phase (i.e., $T_d = T_g$). Consequently, the terms of G and k_f change according to T_f as

$$G = \begin{cases} \rho_g C_{p,g}(1 - \delta_d) + \rho_d C_{p,d}\delta_d & \text{for } T_f \leq T_b \\ \rho_g C_{p,g} & \text{for } T_f > T_b \end{cases}, \tag{96}$$

$$k_f = \begin{cases} k_g \dfrac{2\delta_d(k_d - k_g) + k_d + 2k_g}{2k_g + k_d - \delta_d(k_d - k_g)} & \text{for } T_f \leq T_b \\ k_g & \text{for } T_f > T_b \end{cases}. \tag{97}$$

As droplets are considered spherical, the Maxwell–Garnett mixing relation was used for estimating the heat conductivity of the fluid phase k_f.

6.2 Design of the microwave applicator

The governing equations and properties described above are used along with the finite element method in the commercial solver COMSOL Multiphysics (version 5.6 from Comsol Inc.) to support the design of the microwave applicator and to study the droplet flow. Boundary conditions applied in the numerical calculations are summarized in Table 6.1.

Table 6.1. Applied boundary conditions for the numerical calculations.

Flow Boundary Conditions			
Interface	Velocity	Pressure	Remarks
Inlet	$\dfrac{du}{dx} = \dfrac{du}{dy} = \dfrac{du}{dz} = 0$	Computed	
Outlet	$\dfrac{du}{dx} = \dfrac{du}{dy} = \dfrac{du}{dz} = 0$	$P = 0$	y^+ is the dimensionless wall-thickness parameter
Walls (no slip)	$u\vert_{(y^+=0)} = 0$	Computed	
Electromagnetic Boundary Conditions			
Interface	Electric Field		Remarks
Walls	$n \times E = 0$		Perfect electric conductor
Ports	Computed		
Heat Transfer Boundary Conditions			
Interface	Heat Flux		Remarks
Inlet	$-n \cdot q = (u \cdot n)\rho \displaystyle\int_{T_{ext}}^{T} C_p dT$		$T_{ext} = 25\ °C$ and n is the vector normal to the boundary
Outlet	$-n \cdot q = 0$		
Walls	$q = h(T_{ext} - T)$		

The applicator is designed for loading cylindrical samples (diameter = 54.2 mm and height = 70 mm) with linear pore densities of 30, 45 and 60 ppi with P ranging between 86.8 % and 90.6 %, as shown in Table 6.2.

Table 6.2. Porosity of SiC-based open-cell foams.

Pore Density	SBSiC			SSiC			SiSiC		
/ ppi	30	45	60	30	45	60	30	45	60
P / -	0.902	0.905	0.906	0.896	0.896	0.903	0.868	0.87	0.874

The microwave applicator is intended to concentrate the power of a microwave source working at a frequency of 2.45 GHz to the ceramic foam. A rectangular waveguide WR430 is selected as the transmission line. This waveguide works with a cutoff frequency for the lowest order mode of 1.372 GHz and an upper order mode of 2.745 GHz. As illustrated in Figure 6.3, the design concept proposes that the droplet-laden stream would cross the waveguide inside a quartz tube (microwave transparent) containing a cylindrical foam sample of 50 mm in diameter.
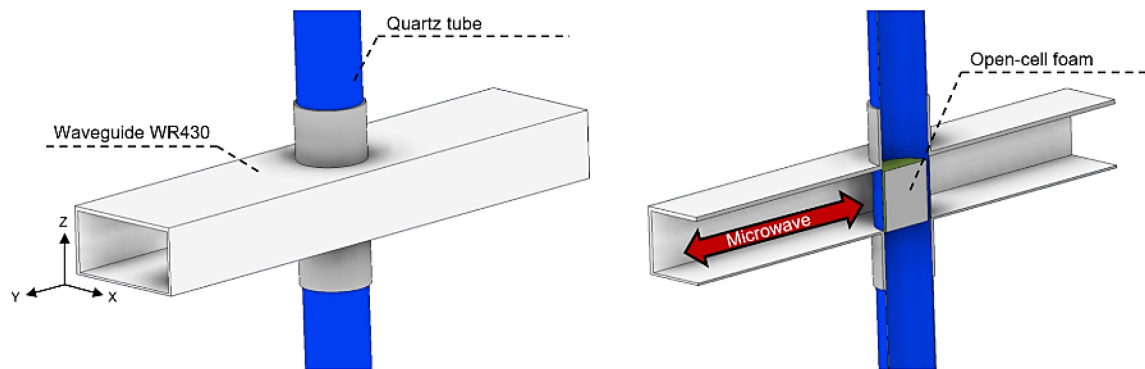
Figure 6.3. Design concept of the microwave applicator transmission line.

Simulations with different mesh element sizes were performed to ensure grid-independent results. Eventually, a mesh with a cell length ranging from 0.001 to 0.080 mm was chosen for computations. In order to modify and increase the electric field distribution within the foam, metallic components in the form of rods were incorporated into the simulation design. A parametric sweep study was conducted to enhance the confinement of the electric field within the foams. Variables such as the number of rods, rod diameter, rod disposition, and the radial distance from the foam sample were considered as independent parameters in the parametric study, as illustrated in Figure 6.4.
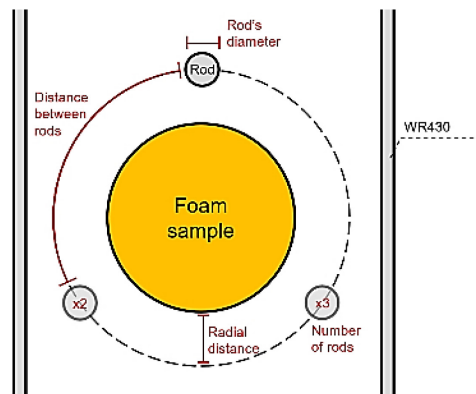
Figure 6.4. Waveguide top view schematic representation of the metallic rod's used for the numerical parametric study.

Based on the parametric study, a design with four equally spaced rods was found to enhance the electric field within the foams while being feasible and practical for construction. Each rod has a diameter of 12 mm and a radial distance to the foams of 19.8 mm. Moreover, in order to contain microwaves inside the cavity and tubes, two metallic caps made of woven wire meshes were designed. The wire diameter and pore size of the mesh are 0.52 mm and 2.0 mm (matching available commercial wire meshes), respectively. The meshes were included in the numerical calculations, allowing fluids to move through the tubes but confining microwaves within the applicator due to the cutoff frequency of the mesh holes. Foams were fixed inside the quartz tube in between two microwave transparent tube supporters, i.e. made of polyetheretherketone (PEEK). In addition, to match the connection options for the microwave applicator, linear growth ramp connectors for WR340 and WR430 waveguides were incorporated at each end of the device. The final design of the microwave applicator is depicted in Figure 6.5. The numerical boundary conditions used in the simulations are presented in Table 6.1.
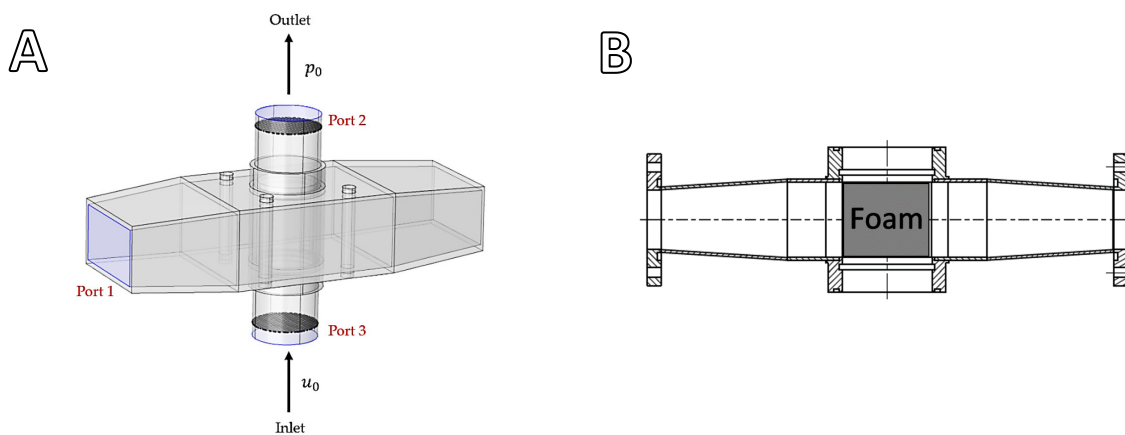
Figure 6.5. Microwave applicator design: (A) model design with boundary surfaces, (B) internal view plane displaying the foam position.

6.3 Simulated electric field distribution

Numerical calculations were used to provide insights of the electric field distribution. Computations were performed using a wave excitation in the TE10 mode and the convergence criterion for the scaled residuals was set to 10^{-4}. Figure 6.6 shows the electric field distribution in the microwave applicator simulated using COMSOL. Optimization of the electric field strength at the core of the foam was achieved by adjusting the sliding short circuit length to achieve impedance matching. The simulations have shown that the maximum electric field strength achievable in the applicator is approximately 50 kVm^{-1} (as shown in Figure 6.6, A) for an input magnetron power of 1 kW. The electric field strength at the core of the foam ranges from 14 kVm^{-1} to 30 kVm^{-1} as presented in Table 6.3 and illustrated in Figure 6.6, B.
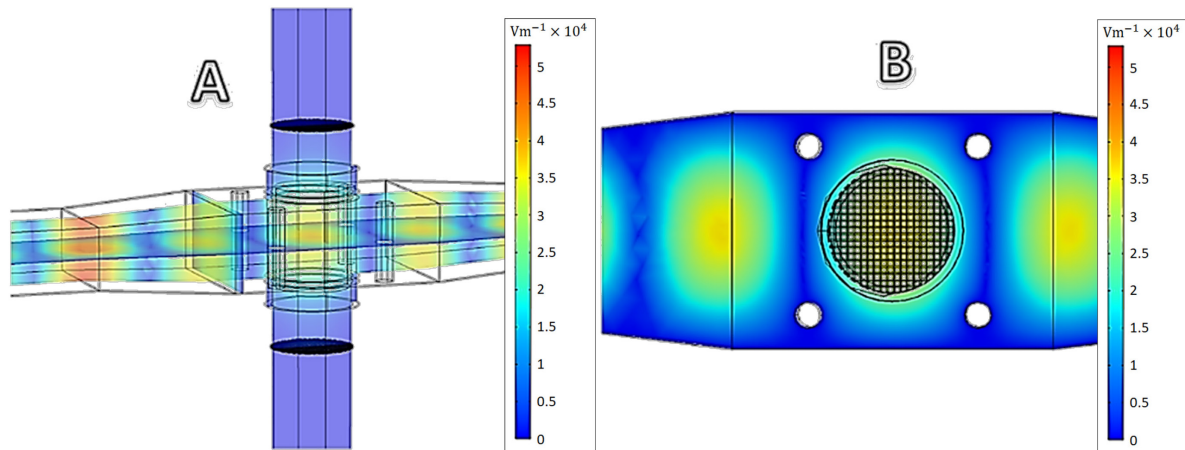
Figure 6.6. Example of the electric field distribution: (A) tube and applicator, and (B) upper cross-sectional view of the applicator using a SiSiC foam.

Table 6.3. Maximum electric field strength in the foams for concentrating the electric field distribution to the foam's core.

Foam	Maximum E-field / kVm^{-1}	P / -
SiSiC	14	0.87
SSiC	25	0.90
SBSiC	30	0.90

Moreover, the cavity provides maximum heating to the foams since the electric field is effectively focused on the core of the foam as shown in Figure 6.7, which illustrates the side-half cross-sectional view of the applicator loaded with SiSiC.
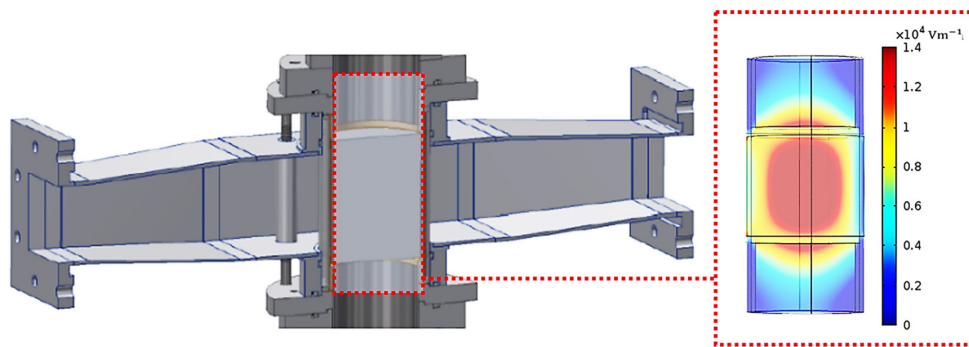
Figure 6.7. Example of the 3D maximum electric field distribution in the tube at the foam's core (SiSiC, 30 ppi).

6.4 Experimental setup

As illustrated in Figure 6.8, the microwave applicator was constructed and equipped with the following components:

- Microwave generator: the experimental setup uses a magnetron (1200049 from Muegge GmbH, Reichelsheim, Hesse, Germany) to generate microwaves at a frequency of 2.45

GHz with adjustable microwave power supply up to 2 kW (GEN2450/2.0KW2CSA from Ibf electronic GmbH and Co., Ober-Ramstadt, Hesse, Germany).

▪ Isolator: consists of a passive 3-port circulator (MW1003A-210EC from Muegge GmbH, Reichelsheim, Hesse, Germany) containing ferrite materials and magnets which control the microwave direction. Ports from the isolator are unidirectional and circulate the energy flow from each port to its clockwise adjacent port. The isolator operates at 2.45 GHz rating.

▪ Three-stub tuner: an impedance transformer (MW2009A-260ED model from Muegge GmbH in Reichelsheim, Hesse, Germany) designed to introduce a variable shunt susceptance into a transmission line to achieve load impedance matching.

▪ Dummy load: consist of a water circulator (MW1002E-260EC from Muegge GmbH, Reichelsheim, Hesse, Germany), in which the water absorbs the residual power exiting the waveguide load. Moreover, a Schottky diode-based detector (MW1001B-111AB from Muegge GmbH, Reichelsheim, Hesse, Germany) is connected to the dummy load for power detection. The diode provides a signal with an amplitude proportional to the input power level.

▪ Sliding short circuit: a low-loss device (MW2005D-260ED from Muegge GmbH, Reichelsheim, Hesse, Germany) which contains a movable short circuit within the waveguide for tuning or adjustment of the transmission line. The short circuit is adjustable for more than half a guide wavelength WR340 at the lowest frequency of operation of 2.2 GHz.
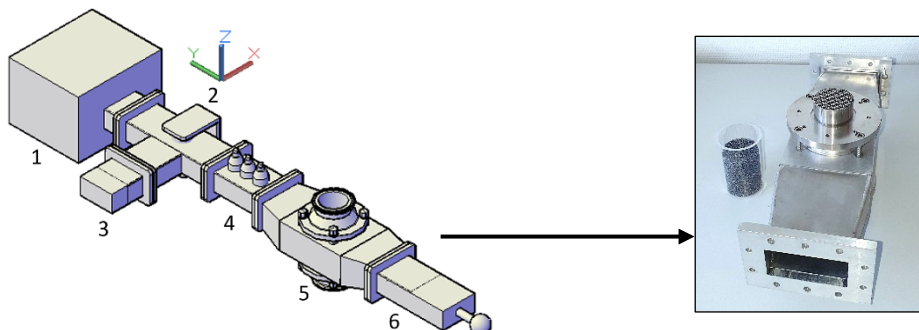
Figure 6.8. Configuration of the microwave applicator setup: (1) magnetron, (2) isolator, (3) water dummy load, (4) 3-stub tuner, (5) microwave applicator, (6) sliding short circuit. The microwave applicator is shown on the right with SiSiC ceramic foam sample and quartz tube.

The latter system enables the modification of the electric field to preferred positions. Moreover, the tuner allows impedance matching of the magnetron to the microwave applicator. This was done by analyzing the voltage amplitude of the microwave signal at the dummy load using an oscilloscope (TDS3032B from Tektronix Inc.). Additionally, an electric field meter (PCE-EM 30 from PCE Instruments) was utilized to monitor and prevent any personal exposure to electric

field strength exceeding 64 Vm^{-1}, which is the maximum electric field strength recommended for exposure of the general public to electromagnetic fields [161].

Droplets are produced by an air-driven spray-nozzle atomizer (SU1A from Spraying Systems Co.) and are carried to the microwave applicator via a humidified airflow inlet (see Figure 6.9 left, relative humidity $RH = 85 \pm 2$ %) provided from a packed column humidifier. The airflow inlet velocity is adjusted via a mass flow controller (FMA-2600A from Omega), providing a maximum liquid capacity of 2.2 Lh^{-1} for an atomizing air pressure of 4 bar. A 2D-phase Doppler interferometer (PDI, PDI-x00MD from Artium Technologies Inc.) was used to measure droplet size, velocity, number density and flux at the inlet and the outlet of the microwave applicator.
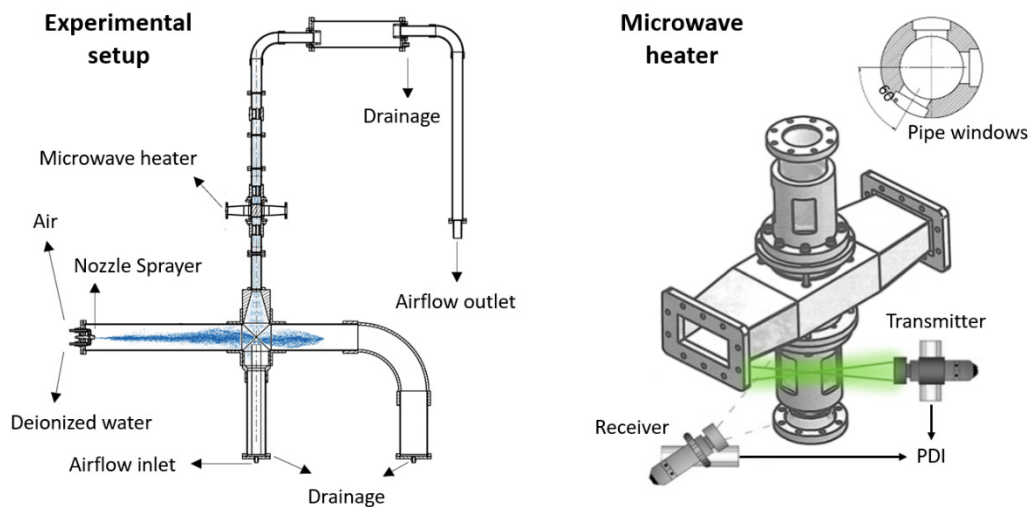
Figure 6.9. Experimental setup with details of microwave applicator and PDI measurement system.

PDI measurements were conducted at pipe components fabricated with rectangular windows. These windows were placed before and after the microwave applicator (see Figure 6.9, right) to measure the effects of foams and microwave heating on the entering droplet population. The exact measuring points (PDI probe volume) were adjusted by intersecting the two laser beams from the PDI transmitter at 6 cm below (inlet position) and above (outlet position) the foam. Dry air (RH = 0 %, $u_g = 12$ ms^{-1}, $T = 20 \pm 1$ °C) was blown for 3 min before each measurement to remove any remaining water accumulation to avoid film formation or droplet production in pipelines and foams. PDI measurements were performed at least three times per investigated parameter for each foam sample. Droplets that exceeded more than three standard deviations of the average droplet size were removed to eliminate outliers. The input gas velocity and the magnetron input power were varied from 2.5 to 14.0 ms^{-1} and from 200 to 1000 W, respectively. A droplet flow with a volume fraction < 0.1 was carried to the microwave applicator. Experiments were performed under atmospheric pressure and a controlled ambient temperature of 20 °C. Note that the microwave applicator is referred to as loaded when it contains a foam, otherwise, it is defined as unloaded. Appendix A.1 and A.2 show the technical drawings of the microwave applicator and experimental setup.

In addition, foam temperatures were measured using a high-definition fiber optic temperature sensor (HDS01LC220P from Luna innovations) and an optical distributed sensor interrogator

(OdiSI-B 5.0 Luna innovations). As illustrated in Figure 6.10, the fiber was inserted into the foam section by passing it through the holes of a metallic wire mesh, and a section of the foam was cut to a depth of 2 mm to accommodate the fiber in the resulting aperture. Finally, the volumetric flow and temperature of water at the inlet and outlet of the dummy load were measured for the microwave applicator loaded with a 30 ppi SiSiC foam sample. The reflected power was calculated and was found to be 17.2 %. It is worth noting, however, that not all experimental conditions were monitored for calculating the reflected power.
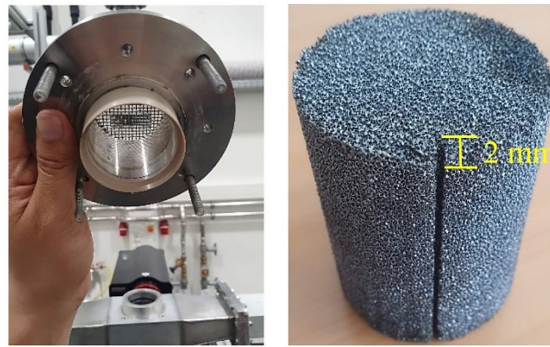
Figure 6.10. Illustration of (left) the wire metallic mesh and (right) the cut made in the samples to adjust the fibre optic.

6.5 Microwave-assisted droplet removal

The size and velocity of droplets at the inlet and outlet positions of the unloaded microwave applicator are shown in Figure 6.11. More than 20,000 droplets were considered for each measurement, where each count corresponds to a single droplet. Measurements are reported per parameter and not per measurement. Droplet size is reported in terms of the arithmetic mean diameter d_{10} and d_{V09}. The definition of d_{V09} is that 90 % of the total number of the sprayed volume is made of droplets with diameters smaller than or equal to d_{V09}. The uniformity of the droplet size is quantified through the relative span fact $RSF = (d_{V09} - d_{V01})/d_{V05}$, where d_{V01} and d_{V05} have definitions equivalent to d_{V09} but accounting for 10 % and 50 %, respectively.

Figure 6.11, A, shows that the majority of primary droplets reaching the microwave applicator are smaller than 15 µm. Droplets at the inlet are completely entrained as their velocity equals the mean gas velocity (see Figure 6.11, A). However, droplets crossing the outer position (located 1 cm above the metallic mesh) are slightly faster than those at the inlet. The increase in the average velocity corresponds to the higher gas velocity developed due to a decrease in the cross-sectional area of the metallic wire mesh, which in accordance with numerical calculations, prevails up to ~1 cm above the mesh, as shown in Figure 6.12.

The velocity distribution in Figure 6.11, B exhibits a wider spread at the outlet compared to the inlet. This can be attributed to the presence of smaller droplets that cross the foam more rapidly, as well as larger droplets that travel slower and cannot easily adjust to airflow changes within the foam. Figure 6.11, C shows an increase in RSF at the outlet, which is consistent with a significant decrease in d_{V05} and d_{V01} but not of d_{V09}. This RSF trend is likely due to the

production of smaller droplets. The higher percentage of small droplets in the flow is caused by the reduction in droplet size, which apart from being caused by droplet vaporization by diffusion, is also related to the surface filtering effect of the metallic wire mesh.
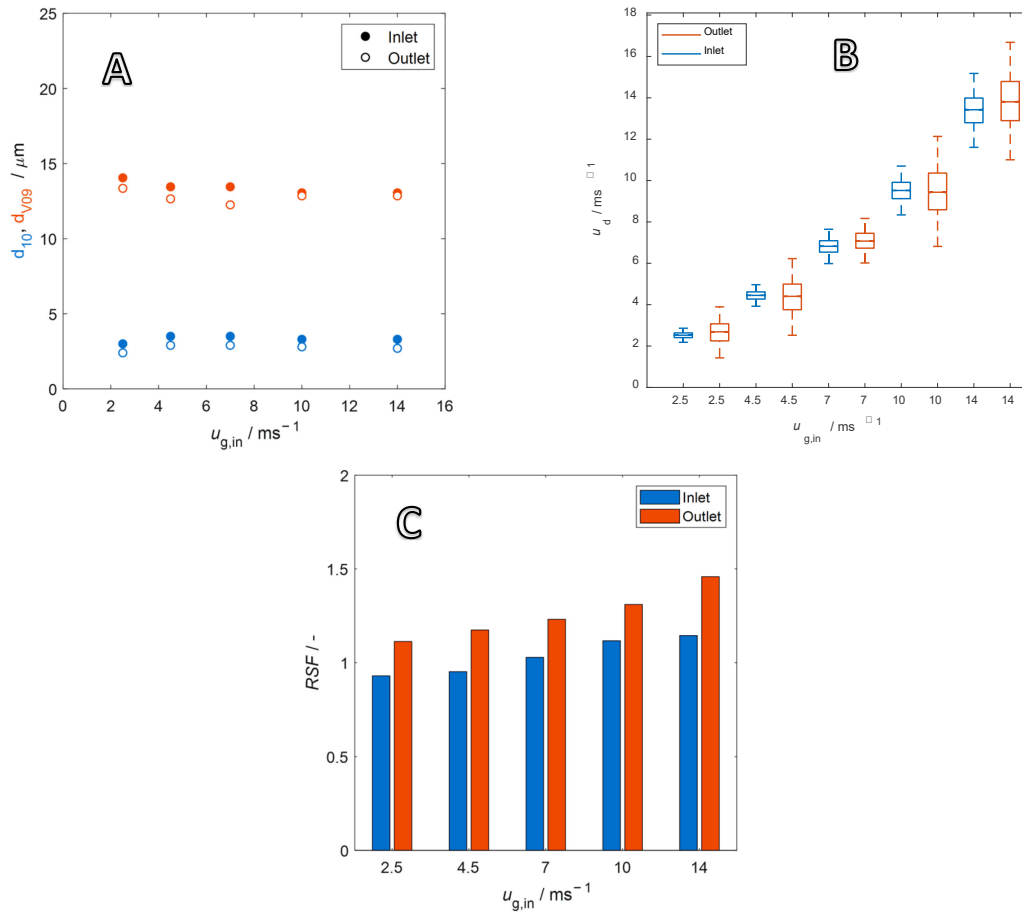
Figure 6.11. (A) diameter, (B) velocity and (C) relative span factor of the droplets at inlet and outlet of the unloaded microwave applicator for different of gas inlet velocities.
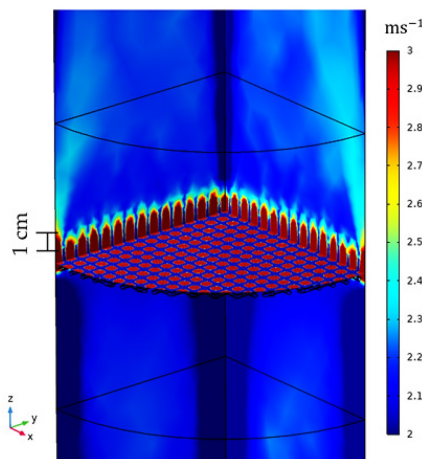
Figure 6.12. Gas velocity field for the nonheated unloaded microwave applicator using a gas flow in z-direction with an inlet velocity of $u_g = 2.5$ ms^{-1}.

Figures 6.13, 6.14 and 6.15 show velocity, size, RSF and volumetric flux Φ_{vol}, respectively, of droplets crossing the outlet position of the microwave applicator loaded with SBSiC, SSiC and SiSiC foams. Microwave heating cannot be applied to the unloaded cavity, since heating can only be applied if a microwave-absorbing material is present. In order to avoid damage to the applicator due to the occurrence of arcing, the magnetron power is only increased at higher gas velocities. The arcing breakdown voltage decreases as the temperature rises due to a decrease in air density [162]. Thus, arcing does not occur at higher flow velocities that further cool the foams.
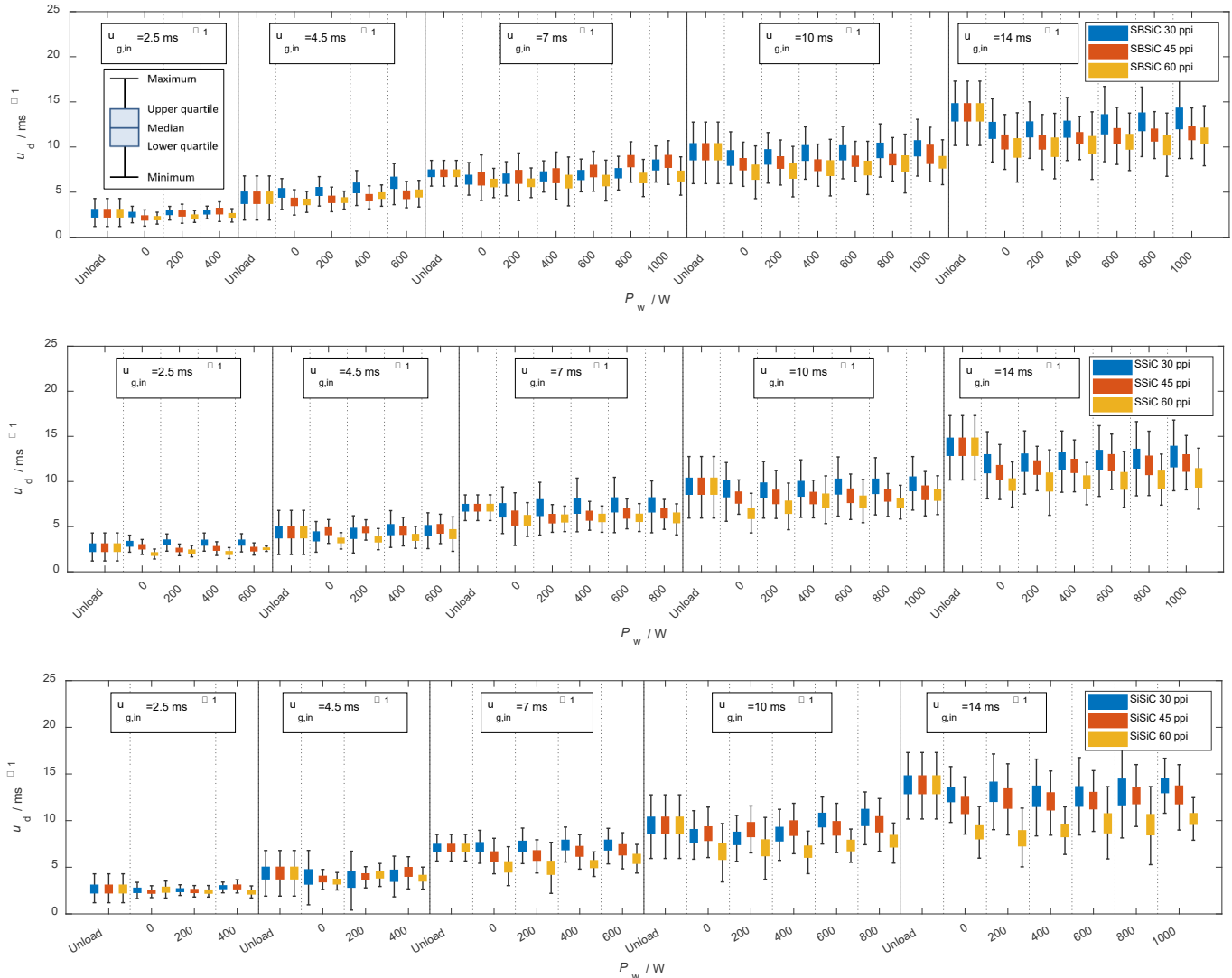
Figure 6.13. Velocity of droplets crossing the outlet position of the microwave applicator loaded with SBSiC (top), SSiC (middle) and SiSiC (bottom) foams at an input magnetron power up to 1 kW.

As shown in Figure 6.13, the average droplet velocity along the direction of the airflow decreases after impingement within the foams and, thus, decreases as the pore density increases. It should be noted that droplets have not regained the mean stream velocity at the outlet position. Additionally, as the input magnetron power increases the foam's temperature increases while

the gas density decreases. Therefore, volumetric flow and gas velocity also increase, and entrained droplets move faster as the magnetron input power increases as shown in Figure 6.13.

Figure 6.14 shows that the droplet size is reduced after passing through the loaded applicator, which is consistent with the well-known filtering effect of such foams. The size does not decrease as the input magnetron power increases. Thus, it can be concluded that most droplets are removed through interactions with the foams rather than evaporated by direct microwave radiation. This is also supported by the relative span factor shown in Figure 6.15, which does not show an increasing trend as the power increases. The porosity of the foams remains constant regardless of the pore density (see Table 6.2) and their effective permittivity is almost identical. Therefore, it can be inferred that the microwave heating rate and resulting temperature should also be similar for these foams. Therefore, the change in droplet size is caused by the filtering effect of the foams, as shown by the diameter, which decreases while the pore density increases.
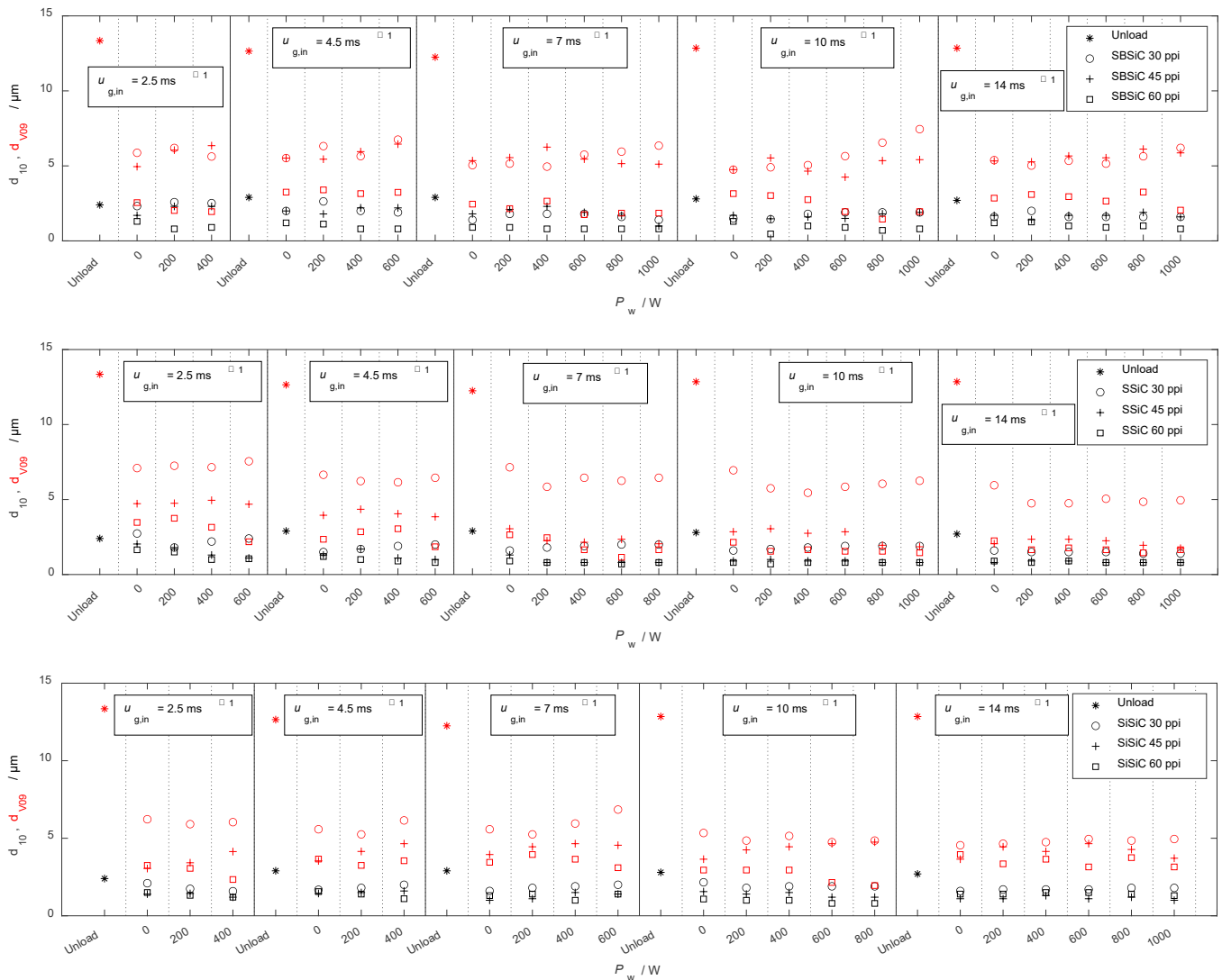
Figure 6.14. Diameters d_{10} (black symbols) and d_{V09} (red symbols) of droplets crossing the outlet position of the microwave applicator loaded with SBSiC (top), SSiC (middle) and SiSiC (bottom) foams at an input magnetron power up to 1 kW.
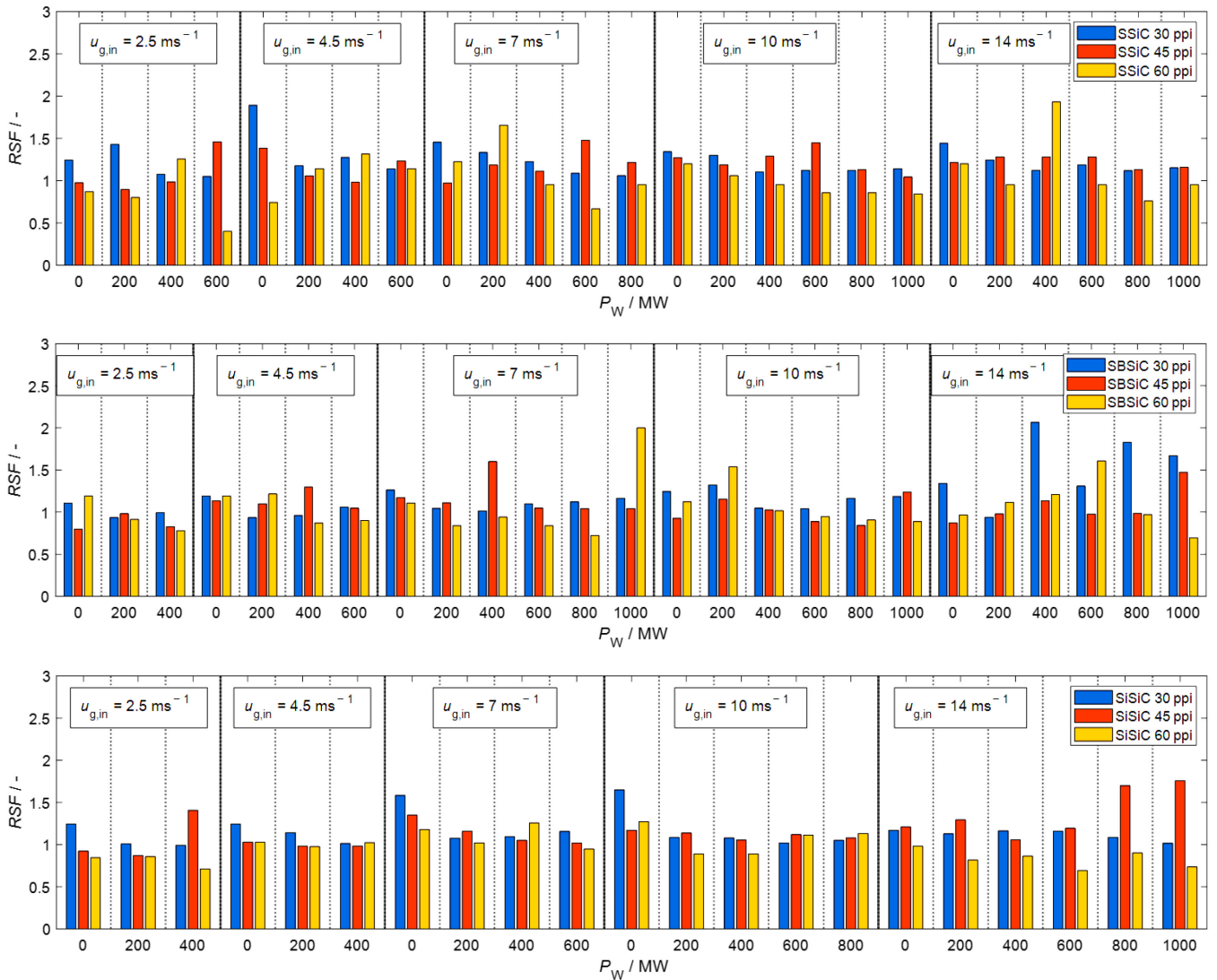
Figure 6.15. Relative span factor of droplets crossing the outlet position of the microwave applicator loaded with SBSiC (top), SSiC (middle) and SiSiC (bottom) foams at an input magnetron power up to 1 kW.

Figure 6.16 shows that the volumetric flux of the droplets is mainly reduced by the filtering effect of the foams, since there is a reduction of up to three orders of magnitude in the volumetric flux of the droplets without microwave heating. While applying microwave heating, the volumetric flux decreases further by one order of magnitude.
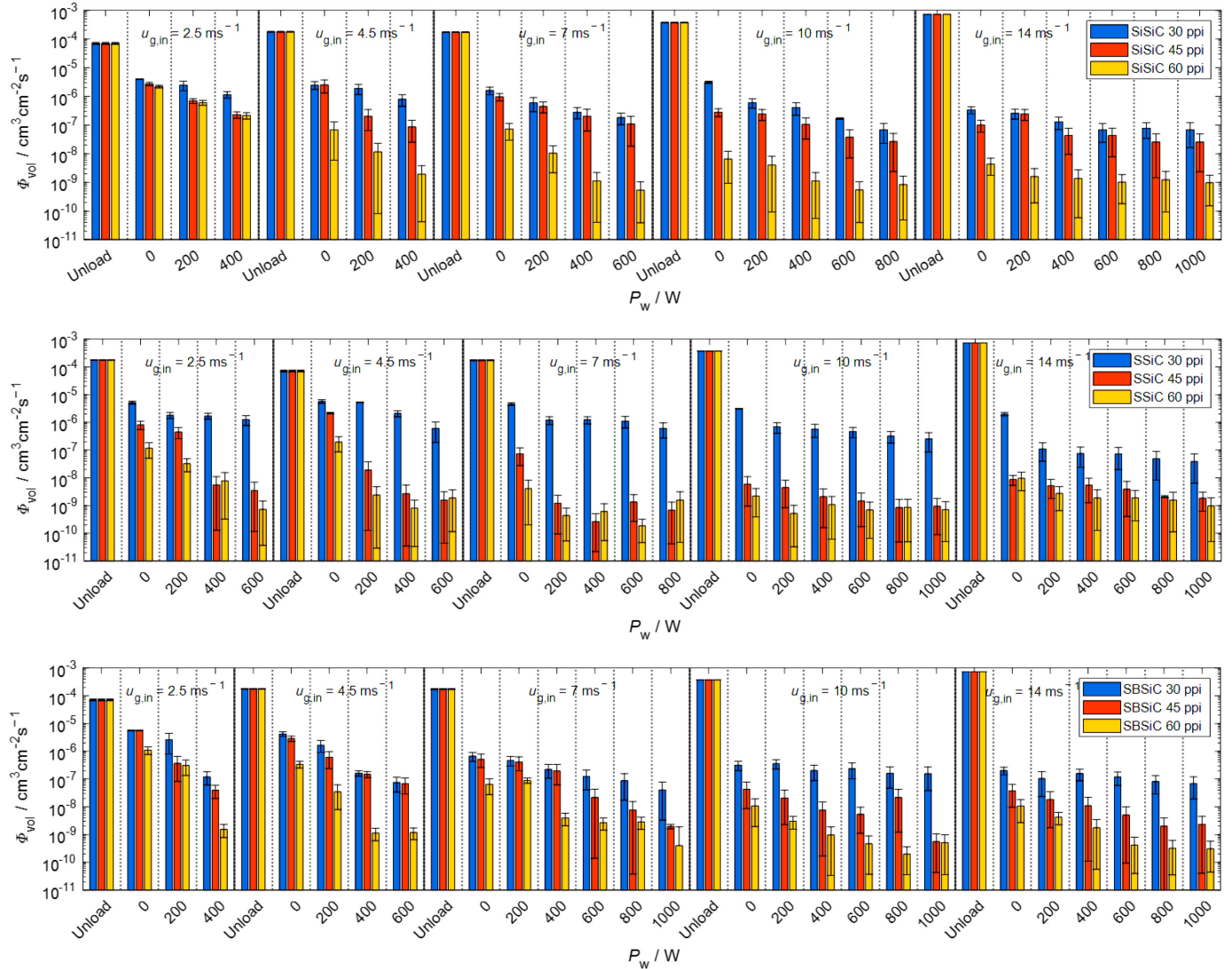
Figure 6.16. Volumetric flux of droplets crossing the outlet position of the microwave applicator loaded with SBSiC (top), SSiC (middle) and SiSiC (bottom) foams at input magnetron power up to 1 kW.

The temperature was measured with the fiber optical temperature sensor as indicated in Section 6.4. It was noted that vibrations in the foam generated a significant level of noise in the acquired signal, which prevented the fibre optical sensor from measuring an accurate temperature. Hence, the results obtained are only appropriate for qualitative comparison. Additionally, the obtained data were smoothed by applying a weighted adjacent averaging method at intervals of 4 temperature points, corresponding to 2.6 mm (fiber spatial resolution is 0.65 mm) along the length of the optical fiber. Figure 6.17 shows the temperature profile of the SiC-based foam samples along their height for $u_g = 14 \text{ ms}^{-1}$ at steady-state. As anticipated, an increase in power input resulted in a corresponding increase in temperature. The results of the experiments revealed that the temperature in certain foam samples exceeded 100 °C, which supports the hypothesis of evaporation of liquid by contact. It should be noted that although clogging and water accumulation in foams were not explicitly quantified, no water accumulation was observed even after 30 min of continuous operation for input magnetron power ratings equal to

or above 400 W. This reflects that the influence of temperature in the foams was high enough to evaporate liquid accumulations. In general, as observed from Figure 6.16, the volumetric flux is decreased according to the following order: SiSiC > SSiC > SBSiC. This order agrees with the order of the maximum electric field strength within foams (e.g. SiSiC < SSiC < SBSiC) as indicated in Table 6.3, which is consistent with an expected higher foam temperature and therefore higher evaporation rates.
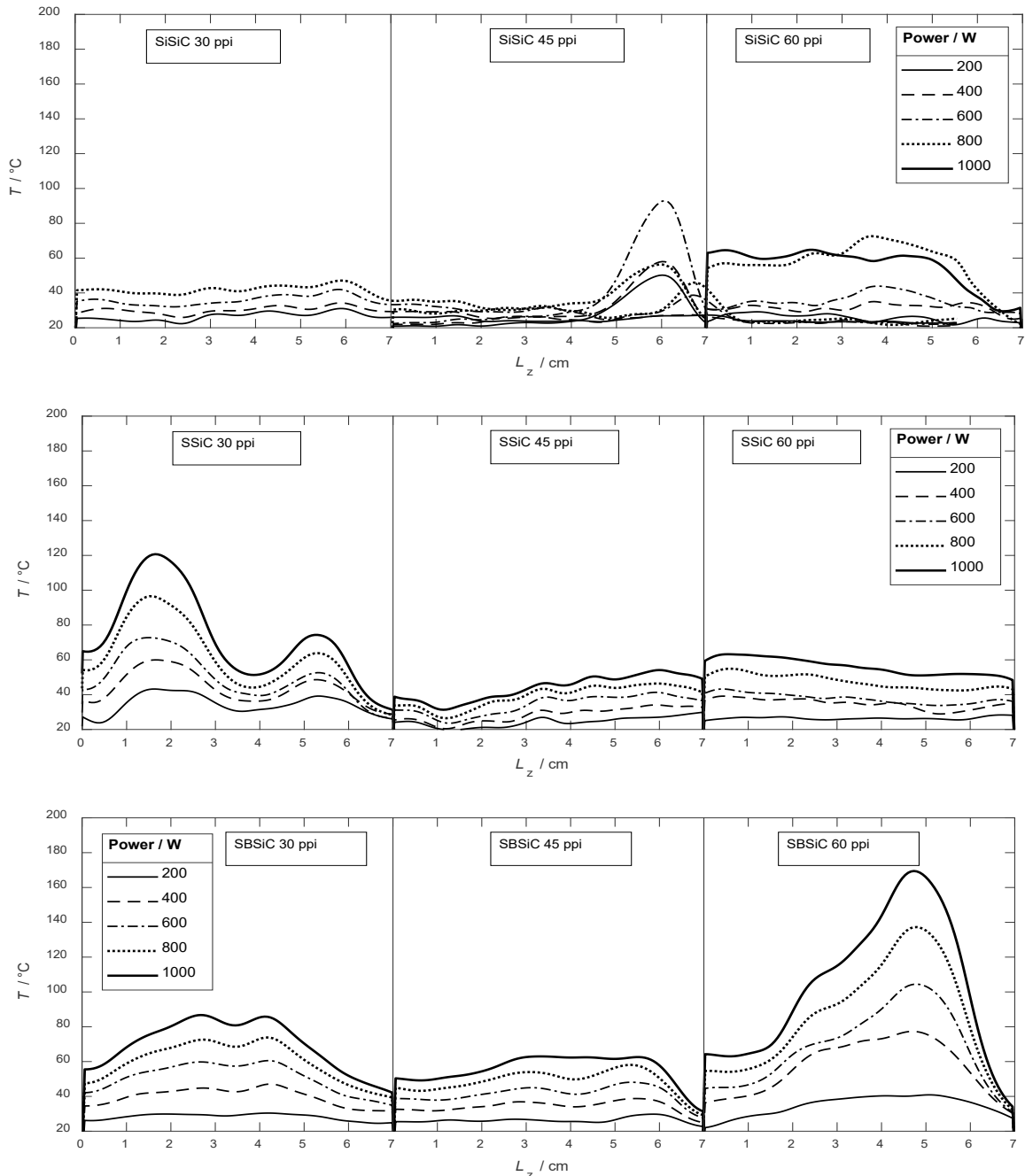
Figure 6.17. Temperature of SiSiC (top), SSiC (middle) and SBSiC (bottom) foams at input magnetron power up to 1 kW. The temperature was measured along the height (7 cm) of the cylindrical samples.

6.6 Conclusion

In this chapter, a microwave applicator was designed to experimentally evaluate droplet removal using microwave-heated open-cell foams. The experimental setup was intended to study the microwave applicator system for the removal of air-entrained droplets at room temperature and saturated airflow. A wide range of airflow conditions and varying levels of microwave input power were investigated. Experiments quantified the reduction of droplet volumetric flow rates as much as ~99.9 % when using open-cell foams as filter media, while microwave-heated foams result in a further reduction up to ~99.99 %. The results also show that the major contribution to droplet removal is due to mechanical filtration rather than microwave heating and droplet re-evaporation. Moreover, increasing the microwave input power causes a higher temperature in the open-cell foams, which in turn decreases the volumetric droplet flow within foams via evaporation. However, higher temperatures are related to arcing occurrence in the foams. High temperatures were also found to prevent structure-borne liquid accumulations. Thus, the device presented has proven to be a compact solution for droplet removal in pipeline installations that combines primary and secondary droplet separation in a single step. In addition, evaporation of liquid accumulations by microwave heating was found to prevent water clogging in open-cell ceramic foams.

Chapter 7

Conclusions and Recommendations

7.1 Conclusions

This thesis presents an investigation of the feasibility of utilizing microwave heating on open-cell ceramic foams for droplet filtration and evaporation. The relevant conclusions of each part are summarized below.

In Chapter 3, the utilization of tomography data sets to generate foam models for computational fluid dynamics calculations has been demonstrated as an advantageous method for analyzing droplet flows within open-cell foams. The numerical calculations indicate that droplet capture is mainly affected by the velocity of the gas-entraining droplets and the relative size of droplets to the foam's pore size. Moreover, the reported data on droplet residence time and percentage of removal offer means to evaluate droplet separation under specific conditions. Taken together, these findings highlight the potential of open-cell foams as fine droplet separators.

In Chapter 4, the dielectric properties of SiC-based ceramic foams were characterized using the cavity perturbation technique. The results showed that the effective permittivity of the foams varied based on the additives or dopants used during sintering, causing changes in conductivity. The porosity of the foam was found to be a significant factor in determining the permittivity, while pore density and size had no impact. This finding is relevant for droplet flow studies, as it suggests that the choice of pore density for droplet removal can be made without affecting the foam's microwave heating performance.

Chapter 5 explored the estimation of the effective permittivity of open-cell foams using mixing relations and numerical calculations. A new empirical relation was proposed, which only depends on porosity, bulk material permittivities, and geometrical parameters depending on the model structure. Cross-property estimation was performed by comparing effective thermal conductivity predictions with experimental and numerical data from the literature as well as with predictions from available mixing relations. Discrepancies between predicted and experimental values were observed, and it was found that only a few synthetic structures are morphologically consistent with real foams. These findings provide important recommendations for selecting appropriate mixing relations based on foam porosity and bulk material properties.

Chapter 6 presented the design and experimental evaluation of a microwave applicator system for droplet removal using microwave-heated open-cell foams. The experimental setup was used to investigate a wide range of operational airflow conditions and varying levels of microwave input power. The results showed that open-cell foams as filter media could reduce the droplet volumetric flow rate as much as ~99.9 %, while microwave-heated foams can further reduce it up to ~99.99 %. Mechanical filtration was found to be the major contribution to droplet removal rather than microwave heating. Note that without sufficient microwave heating, the foam may eventually become clogged. Moreover, the droplet volumetric flux results suggest that the microwave applicator is effective in evaporating liquid accumulations, likely due to the high-power density and rapid heating achieved by the applicator. In conclusion, the device presented in this study has been demonstrated to combine primary and secondary droplet separation into a single step.

7.2 Recommendations

The numerical modelling of droplet capturing requires extending the droplet impingement outcome to further account for droplet bouncing and to include a threshold criterion for re-entrainment of deposited droplets or accumulated water. Furthermore, future research should focus on investigating the impact of increased Kozeny-Carman Reynolds numbers ($Re_{KC} > 300$) at which splashing plays a major role. The work presented in this thesis serves as a preliminary CFD investigation due to its limitations in dilute flow and superficial gas velocities up to 1.7 ms^{-1}. However, higher concentrations and velocities of the droplet, as well as comparison with experimental work, needs to be further investigated.

Numerical simulations of electromagnetic wave propagation using computed tomography reconstructed foam samples were conducted to model and correlate the effective permittivity of the foams containing any fluid therein. This approach enables efficient and reliable estimations of the effective permittivity. However, further investigations are needed to extend the geometrical characterization of open-cell foams because the morphology was observed to change with the porosity. Consequently, estimations from mixing relations would be improved by appropriate consideration of the skeletal geometry at any porosity.

Open-cell foam skeletons do not induce a preferential local droplet distribution in the annular or core droplet flow. Therefore, using novel structural ceramics, such as monoliths and periodic open-cell elements, which can generate specific local flow fields, is considered a highly promising approach for developing future microwave-heated fine droplet separators.

Solid-state microwave generators are a potential alternative to traditional magnetron power systems. These generators offer the ability to generate high-power microwaves and vary the frequency during operation, leading to a more versatile operation as it enables the spatial manipulation of the low and high electric field spots within the fine droplet separator. Future research should systematically investigate the utilization of solid-state microwave generators and associated setup parameters in designing and implementing a microwave applicator. In addition, it would be beneficial to design an applicator that improves the matching between the microwave source and the load to reduce reflected power. Moreover, the power wasted to cool down the microwave source could be potentially harnessed as a heating service for other streams involved in the operation. For instance, the heat could be used to preheat ambient temperature water that is fed into the process, reducing energy usage and cost.

Finally, implementing a real-time process data acquisition in the experimental setup design would greatly enhance the understanding and evaluation of the investigated droplet removal. A comprehensive understanding of the system can be achieved by quantifying parameters such as foam liquid accumulation and temperature profile. In-situ measurements can be obtained by integrating microwave moisture measurements using the microwave resonance of the designed microwave applicator. This method is based on detecting the microwave resonance frequency of the cavity, which is sensitive to variations in the permittivity of the air/steam mixture, in the ceramic separator material, and water content. The measurement system is expected to achieve a temporal resolution that is greater than the residence time of the droplets, while maintaining a spatial resolution corresponding to the whole fine droplet separator. Furthermore, real-time determination of the temperature profile, for example, using thermal infrared sensing, would provide valuable feedback for the correlation of the electric field applied to foams.

References

[1] E.B. Woodruff, H.B. Lammers, and T.F. Lammers, "Steam plant operation," 10th Edition, McGraw-Hill Education, New York, 2017.

[2] K. Jasch, J. Schulz, H.-J. Bart, and S. Scholl, "Droplet entrainment analysis in a flash evaporator with an image-based measurement technique," Chemie Ing. Tech., vol. 93, pp. 1071–1079, 2021.

[3] Suez, Handbook of industrial water treatment – boiler water systems, viewed 3 March 2023, https://www.suezwatertechnologies.com/handbook/chapter-16-steam-purity. 2020.

[4] J.M. Haight, Handbook of loss prevention engineering, 2 Vol., first edition, Wiley-VCH Verlag GmbH & Co. KgaA, 2013.

[5] V. Vishwakarma, M. Schubert, and U. Hampel, "Assessment of separation efficiency modeling and visualization approaches pertaining to flow and mixing patterns on distillation trays," Chem. Eng. Sci., vol. 185, pp. 182–208, 2018.

[6] S. Soni, "Erosion 113ehavior of steam turbine blades of glass-epoxy," 2011.

[7] K. Rayaprolu, Boilers for power and process, CRC Press, viewed 3 March 2023, https://books.google.de/books?id=unGSfNa8wocC, 2009.

[8] Siemens Energy, "Industrial Steam Turbines: Industrial steam turbines from 2 to 250 MW," Siemens Energy, viewed 12 January 2023, https://assets.siemens-energy.com/siemens/assets/api/uuid:1957c70c-6d96-4716-b239-428a53fdff4b/se-brochure-industrial-steam-turbines-2021.pdf?ste_sid=d80bf4d164448ac95619fac6ef5f0f2c.

[9] Herzog, "Reheater for a moisture separator reheater," US Patent 3,996,897, 1976.

[10] P. Wiedemann, A. Döß, E. Schleicher, and U. Hampel, "Fuzzy flow pattern identification in horizontal air-water two-phase flow based on wire-mesh sensor data," Int. J. Multiph. Flow., vol. 117, pp. 153–162, 2019.

[11] J.M. Mandhane, G.A. Gregory, and K. Aziz, "A flow pattern map for gas—liquid flow in horizontal pipes," Int. J. Multiph. Flow, vol. 1, pp. 537–553, 1974.

[12] A. Saha, J. Lee, S. Basu, and R. Kumar, "Breakup and coalescence characteristics of a hollow cone swirling spray," Phys. Fluids, vol. 24, 2012.

[13] R.S. Volkov, G. V Kuznetsov, and P.A. Strizhak, "Criterion expressions for conditions and deceleration and subsequent entrainment of water drops by high-temperature gases," Tech. Phys., vol. 60, pp. 1310–1315, 2015.

[14] V. Terekhov and M. Pakhomov, "Numerical study of hydrodynamics and heat and mass transfer of a ducted gas–vapor-droplet flow," J. Appl. Mech. Tech. Phys., vol. 44, pp. 90–101, 2003.

[15] W.R. Carson and H.K. Williams, "Method of reducing carry-over and reducing pressure drop through steam separators," United States, 1980.

[16] Š. Šefko and B. Edin, "Analysis of droplet deposition in a vertical air-water dispersed flow," Procedia Eng., vol. 100, pp. 105–114, 2015.

[17] SULZER, Gas/liquid separation technology, SULZER Chemtech, viewed 3 March 2023, https://www.sulzer.com/-/media/files/products/separation-technology/feed-inlet-devices/gas_liquid_separation_technology.ashx?la=en. N.d.

[18] M.J. Moore, "Two-phase steam flow in turbines and separators – Theory, Instrumentation, Engineering," 1976.

[19] N.I. Kolev, "Multiphase Flow Dynamics 4," 1st ed., Springer, Berlin, Heidelberg, 2009.

[20] A.I. Jøsang and M.C. Melaaen, "Fluid flow simulations of a vane separator," Model. Identif. Control., vol. 23, no. 1, pp. 5-26, 2002.

[21] K.C. Foong, "Design concept for a more efficient steam-water separator," 2004.

[22] S.J. Zarrouk and M.H. Purnanto, "Geothermal steam-water separators: Design overview," Geothermics, vol. 53, pp. 236-254, 2015.

[23] M. Stewart and K. Arnold, "Two-phase gas-liquid separators," in Gulf Professional Publishing, Burlington, 2008, pp. 65-130.

[24] P. Griffith, "Vapor-Liquid Separation," AtoZ Encyclopedia of Chemical Engineering, n.d.

[25] Hisham T. El-Dessouky and Hisham M. Ettouney, "Fundamentals of salt water desalination," Chapter 9 – Associated Processes, Elsevier Science B.V., Amsterdam, 2002, pp. 453-502.

[26] S.B.D. N. Ren, K.V. Meredith, H.Z. Yu, Xiangyiang Zhou, and Y. Wang, "Water mist fire suppression modeling of rack storage fires in open space," in Proc. 11th Asia-Oceania Symp. Fire Sci. Technol., Springer Nature, 2019.

[27] Sulzer, Liquid-liquid separation technology, Sulzer Chemtech, viewed 3 March 2023, https://www.sulzer.com/germany/-/media/files/products/separation-technology/coalescer/liquid_liquid_separation_technology.ashx?la=en. N.d.

[28] J.N.C. Hernandez, G. Lecrivain, M. Schubert, and U. Hampel, "Droplet retention time and pressure drop in SiSiC open-cell foams used as droplet separation device – A numerical approach," Ind. Eng. Chem. Res., vol. 58, no. 19, pp. 8091-8100, 2019.

[29] J. Zalucky, M. Wagner, M. Schubert, R. Lange, and U. Hampel, "Hydrodynamics of descending gas-liquid flows in solid foams: Liquid holdup, multiphase pressure drop and radial dispersion," Chem. Eng. Sci., vol. 168, pp. 480-494, 2017.

[30] S.C. D., H.M. G., Z.J. Michael, "An experimental investigation of fluid flow resulting from the impact of a water drop with an unyielding dry surface," Proc. R. Soc. London. A. Math. Phys. Sci., vol. 373, pp. 419–441, 1981.

[31] C. Mundo, M. Sommerfeld, C. Tropea, "On the modeling of liquid sprays impinging on surfaces," At. Sprays, vol. 8, pp. 625–652, 1998.

[32] I. V Roisman, A. Lembach, C. Tropea, "Drop splashing induced by target roughness and porosity: The size plays no role," Adv. Colloid Interface Sci., vol. 222, pp. 615–621, 2015.

[33] ANSYS, "ANSYS Fluent Theory Guide," (n.d.).

[34] P.J. O'Rourke, A.A. Amsden, "A spray/wall Interaction submodel for the KIVA-3 Wall Film Model," SAE Tech. Pap., 2000.

[35] L.J. Gibson, M.F. Ashby, "Cellular solids: structure and properties," 2nd ed., Cambridge University Press, Cambridge, 1997.

[36] T.P. De Carvalho, H.P. Morvan, D. Hargreaves, "Pore-Level numerical simulation of open-cell metal Foams with application to aero engine separators," ASME Turbo Expo 2014 Turbine Tech. Conf. Expo., American Society of Mechanical Engineers (ASME), Düsseldorf, Germany, 2014.

[37] T. Uhlířová, W. Pabst, "Thermal conductivity and Young's modulus of cubic-cell metamaterials," Ceram. Int., vol. 45, pp. 954–962, 2019.

[38] P. Habisreuther, N. Djordjevic, N. Zarzalis, „Numerische simulation der mikroströmung in porösen inerten strukturen," Chemie Ing. Tech., vol. 80, pp. 327–341, 2008.

[39] A. Diani, K.K. Bodla, L. Rossetto, S. V Garimella, "Numerical analysis of air flow through metal foams," Energy Procedia, vol. 45, pp. 645–652, 2014.

[40] T.P. de Carvalho, H.P. Morvan, D.M. Hargreaves, H. Oun, A. Kennedy, "Pore-scale numerical investigation of pressure drop 115ehavior across open-cell metal foams," Transport in Porous Media, vol. 117, pp. 311-336, 2017.

[41] J. Bear, Dynamics of Fluids in Porous Media, New York: Dover Publications, 1972.

[42] D. Edouard, M. Lacroix, C.P. Huu, F. Luck, "Pressure drop modeling on SOLID foam: State-of-the art correlation," Chemical Engineering Journal, vol. 144, pp. 299-311, 2008.

[43] P.C. Carman, "Fluid flow through granular beds," Chemical Engineering Research and Design, vol. 75, pp. S32-S48, 1997.

[44] R. Chhabra, M.G. Basavaraj, "Flow of fluids through granular beds and packed columns," in Coulson and Richardson's Chemical Engineering: Particulate Systems and Particle Technology, 6th ed., Butterworth-Heinemann, vol. 2a, pp. 335-386, 2019.

[45] B. Andersson, R. Andersson, L. Håkansson, M. Mortensen, R. Sudiyo, B. van Wachem, Computational Fluid Dynamics for Engineers, Cambridge: Cambridge University Press, 2011.

[46] B.V. Antohe, J.L. Lage, "A general two-equation macroscopic turbulence model for incompressible flow in porous media," International Journal of Heat and Mass Transfer, vol. 40, pp. 3013-3024, 1997.

[47] Y.I. Wang, P.W. James, "The calculation of wave-plate demister efficiencies using numerical simulation of the flow field and droplet motion," Chemical Engineering Research and Design, vol. 76, pp. 980-985, 1998.

[48] S. Elghobashi, "On predicting particle-laden turbulent flows," Applied Scientific Research, vol. 52, pp. 309-329, 1994.

[49] F. Evrard, F. Denner, B. van Wachem, "Euler-Lagrange modelling of dilute particle-laden flows with arbitrary particle-size to mesh-spacing ratio," Journal of Computational Physics: X, vol. 8, 100078, 2020.

[50] P.W. James, B.J. Azzopardi, Y. Wang, J.P. Hughes, "A model for liquid film flow and separation in a wave-plate mist eliminator," Chemical Engineering Research and Design, vol. 83, pp. 469-477, 2005.

[51] L. Bravo, C.-B. Kweon, "A review on liquid spray models for diesel engine computational analysis," 2014.

[52] T. Beji, S.E. Zadeh, G. Maragkos, B. Merci, "Influence of the particle injection rate, droplet size distribution and volume flux angular distribution on the results and computational time of water spray CFD simulations," Fire Safety Journal, vol. 91, pp. 586-595, 2017.

[53] M. Simcik, M.C. Ruzicka, A. Mota, J.A. Teixeira, "Smart RTD for multiphase flow systems," Chemical Engineering Research and Design, vol. 90, pp. 1739-1749, 2012.

[54] Z. Zou, Y. Zhao, H. Zhao, L. Zhang, Z. Xie, H. Li, Q. Zhu, "CFD simulation of solids residence time distribution in a multi-compartment fluidized bed," Chinese J. Chem. Eng., vol. 25, pp. 1706-1713, 2017.

[55] D. Kalaga, R. Reddy, J. B. Joshi, S. V. Dalvi, K. Nandakumar, "Liquid phase axial mixing in solid–liquid circulating multistage fluidized bed: CFD modeling and RTD measurements," Chem. Eng. J., vol. 191, pp. 475-490, 2012.

[56] M.R. Cruz-Díaz, E.P. Rivero, F.J. Almazán-Ruiz, Á. Torres-Mendoza, I. González, "Design of a new FM01-LC reactor in parallel plate configuration using numerical simulation and experimental validation with residence time distribution," Chem. Eng. Process. Process Intensif., vol. 85, pp. 145-154, 2014.

[57] J. Manabe, J. Kasahara, I. Fujita, T. Kojima, "Recent moisture separator reheater design technologies," J. Eng. Gas Turbines Power, vol. 132, 2010.

[58] J. Song, X. Hu, J. Zhang, J. Chen, "Experimental study on performance of two types of corrugated plate gas-liquid separators," Energy Procedia, vol. 142, pp. 3282-3286, 2017.

[59] M. Paschetag, A. Paschetag, F. Merkel, C. Mehringer, S. Scholl, "Life cycle analysis: assessment of technologies for droplet separation – a case study," Chemie Ing. Tech., vol. 93, pp. 1058-1070, 2021.

[60] C.P.N.V.V. L. F. Chen C. K. Ong, V.K. Varadan, "Microwave electronics measurement and materials characterization," Chichester, Engl., John Wiley Sons Ltd., 2004.

[61] R. Behrend, C. Dorn, V. Uhlig, H. Krause, "Investigations on container materials in high temperature microwave applications," Energy Procedia, vol. 120, pp. 417-423, 2017.

[62] C.B. Ojeda and F.S. Rojas, "Sample dissolution for elemental analysis of microwave digestion," in Encyclopedia of Analytical Science (Second Edition), P. Worsfold, A. Townshend, and C. Poole, Eds. Elsevier, 2005, pp. 153-163.

[63] D. Herres, "Up close and personal with magnetrons," Test and Measurement Tips, 2020, viewed 11 March 2023, https://www.testandmeasurementtips.com/up-close-and-personal-with-magnetrons-faq/.

[64] H. Jeong, T. Yoon, H. Yoo, H. Jung and S. Cho, "A highly efficient and compact 6kW GaN solid-state microwave generator for CW 2.45GHz applications," 2019 IEEE MTT-S International Microwave Symposium (IMS), Boston, MA, USA, 2019, pp. 572-575

[62] R.R. Mishra, A.K. Sharma, "Microwave–material interaction phenomena: heating mechanisms, challenges and opportunities in material processing," Compos. Part A Appl. Sci. Manuf., vol. 81, pp. 78-97, 2016.

[63] D.M. Pozar, "Microwave engineering," 4th edition, Wiley, USA, 2016.

[64] Kuek Chee Yaw, "Measurement of dielectric: material properties: application note," Rohde & Schwarz, 2012.

[65] T.C. Choy, "Effective medium theory: principles and applications," 2nd Ed., Oxford University Press, 2016.

[66] R. Y.P. Liu Chao and Lee Panetta, "Inhomogeneity structure and the applicability of effective medium approximations in calculating light scattering by inhomogeneous particles," J. Quant. Spectrosc. Radiat. Transf., vol. 146, pp. 113-121, 2014.

[67] M.I. Mishchenko, J.M. Dlugach, and L. Liu, "Applicability of the effective-medium approximation to heterogeneous aerosol particles," J. Quant. Spectrosc. Radiat. Transf., vol. 178, pp. 284-294, 2016.

[68] A. Sihvola, "Dielectric polarization and particle shape effects," J. Nanomater., vol. 2007, p. 045090, 2007.

[69] A. Sihvola, P. Yla-Oijala, S. Jarvenpaa, and J. Avelin, "Polarizabilities of platonic solids," IEEE Trans. Antennas Propag., vol. 52, pp. 2226-2233, 2004.

[70] A. Sihvola and R.W. Burns, Electromagnetic mixing formulas and applications, London, UK: Institution of Electrical Engineers, 1999.

[71] E.S.M.R.D.C.W. Gunßer, "Complex polarizability as used to analyze dielectric relaxation measurements," Colloid Polym. Sci., vol. 270, pp. 905-912, 1992.

[72] J. S. Torquato and H.W. Haslach, "Random heterogeneous materials: microstructure and macroscopic properties," Appl. Mech. Rev., vol. 55, pp. B62-B63, 2002.

[73] W. Pabst and S. Hříbalová, "Describing the effective conductivity of two-phase and multiphase materials via weighted means of bounds and general power means," JOM, vol. 71, pp. 4005-4014, 2019.

[74] W. Pabst and E. Gregorová, "Critical Assessment 18: elastic and thermal properties of porous materials – rigorous bounds and cross-property relations," Mater. Sci. Technol., vol. 31, pp. 1801-1808, 2015.

[75] A.J. Pickles and M.B. Steer, "Effective permittivity of 3-D periodic composites with regular and irregular inclusions," IEEE Access, vol. 1, pp. 523-536, 2013.

[76] J. V. Balbastre, E. de los Reyes, M. C. Nuño, P. Plaza, "Design guidelines for applicators used in the microwave heating of high losses materials," in Advances in Microwave and Radio Frequency Processing, Springer Berlin Heidelberg, Berlin, Heidelberg, 2006, pp. 31–38.

[77] V. Ramopoulos, G. Link, S. Soldatov, J. Jelonnek, "Industrial scale microwave applicator for high temperature alkaline hydrolysis of PET," Int. J. Microw. Wirel. Technol., vol. 10, no. 6, pp. 709–716, 2018.

[78] M. Mehdizadeh, "Microwave/RF applicators and probes for material heating, Sensing, and Plasma Generation," 2010.

[79] E. T. Thostenson, T.-W. Chou, "Microwave processing: fundamentals and applications," Compos. Part A Appl. Sci. Manuf., vol. 30, no. 10, pp. 1055–1071, 1999.

[80] I. Dincer, "Comprehensive energy systems," 1st edition, Elsevier, Cambridge, USA, 2018.

[81] B. Purushothama, "Humidification and ventilation management in textile industry," 1st edition, Wooldhead, New Delhi, India, 2009.

[82] C.B. Ojeda and F.S. Rojas, "Sample dissolution for elemental analysis of microwave digestion," in Encyclopedia of Analytical Science (Second Edition), P. Worsfold, A. Townshend, and C. Poole, Eds. Elsevier, 2005, pp. 153-163.

[83] D. Herres, "Up close and personal with magnetrons," Test and Measurement Tips, 2020, viewed 11 March 2023, https://www.testandmeasurementtips.com/up-close-and-personal-with-magnetrons-faq/.

[84] R. Williams, "Solid-State RF Power Generators," in RF Power Semiconductor Generator Application in Heating and Energy Utilization, Springer, Singapore, 2020.

[85] V. V. Fedotov, A. N. Kargin, G. P. Savenco, and O. A. Morozov, "The magnetron 3 kW at a frequency of 915 MHz for promising systems of heating," in 2014 International Conference on Actual Problems of Electron Devices Engineering (APEDE), Saratov, Russia, 2014, pp. 41-44.

[86] H. Jeong, T. Yoon, H. Yoo, H. Jung and S. Cho, "A highly efficient and compact 6kW GaN solid-state microwave generator for CW 2.45GHz applications," 2019 IEEE MTT-S International Microwave Symposium (IMS), Boston, MA, USA, 2019, pp. 572-575

[87] Muegge, "Magnetron-Head - MH100KS-510BU," viewed 28 April 2023, https://muegge.de/en/product/magnetron-head-mh100ks-510bu/.

[88] J. Adler, G. Standke, "Open-celled foam ceramics" Keramische Zeitschrift, vol. 55, no. 11, pp. 694–703, 2003.

[89] W. Pabst, E. Gregorová, T. Uhlířová, "Microstructure characterization via stereological relations — a shortcut for beginners," Mater. Char., vol. 105, pp. 1–12, 2015.

[90] M. Scheffler, P. Colombo, Cellular ceramics: structure, manufacturing, properties and applications, 2005.

[91] C. T. Rueden, J. Schindelin, M. C. Hiner, B. E. DeZonia, A. E. Walter, E. T. Arena, K. W. Eliceiri, "ImageJ2: ImageJ for the next generation of scientific image data," BMC Bioinformatics, vol. 18, no. 1, p. 529, 2017.

[92] N. Otsu, "A threshold selection method from gray-level histograms," IEEE Trans. Syst. Man. Cybern., vol. 9, no. 1, pp. 62–66, 1979.

[88] T. Hildebrand, P. Rüegsegger, "A new method for the model-independent assessment of thickness in three-dimensional images," J. Microsc., vol. 185, no. 1, pp. 67–75, 1997.

[89] A. Rabbani, S. Jamshidi, S. Salehi, "An automated simple algorithm for realistic pore network extraction from micro-tomography images," J. Pet. Sci. Eng., vol. 123, pp. 164–171, 2014.

[90] M. Doube, M.M. Kłosowski, I. Arganda-Carreras, F.P. Cordelières, R.P. Dougherty, J.S. Jackson, B. Schmid, J.R. Hutchinson, S.J. Shefelbine, "BoneJ: free and extensible bone image analysis in ImageJ," Bone, vol. 47, pp. 1076-1079, 2010.

[91] W. Lorensen, H.E. Cline, "Marching cubes: a high resolution 3d surface construction algorithm," ACM SIGGRAPH Comput. Graph., vol. 21, pp. 163, 1987.

[92] D. Cabiddu, M. Attene, "Large mesh simplification for distributed environments," Comput. Graph., vol. 51, pp. N/A, 2015.

[93] L.A. Freitag, "On combining Laplacian and optimization-based mesh smoothing techniques," Am. Soc. Mech. Eng. Appl. Mech. Div., vol. 220, pp. 37-43, 1997.

[94] T.P. de Carvalho, "Two-phase flow in open-cell metal foams with application to aero-engine separators," Ph.D. Thesis, University of Nottingham, Nottingham, U.K., 2016.

[95] S.A. Morsi, A.J. Alexander, "An investigation of particle trajectories in two-phase flow systems," J. Fluid Mech., vol. 55, pp. 193-208, 1972.

[96] G. Lecrivain, U. Hampel, "Influence of the Lagrangian integral time scale estimation in the near wall region on particle deposition," J. Fluids Eng., vol. 134, pp. 074502, 2012.

[97] A. Gipperich, A.N. Lembach, C. Tropea, "On the splashing threshold of a single droplet impacting onto rough and porous surfaces," in Proceedings of the 23rd Annual Conference on Liquid Atomization and Spray Systems (ILASS - Eur 2010), Brno, Czech Republic, 2010.

[98] C. Mundo, M. Sommerfeld, C. Tropea, "Droplet-wall collisions: experimental studies of the deformation and breakup process," Int. J. Multiphase Flow, vol. 21, pp. 151, 1995.

[99] G. Li, A. Mukhopadhyay, C.-Y. Cheng, Y. Dai, "Various approaches to compute fluid residence time in mixing systems," in Proceedings of the 3rd Joint US-European Fluids Engineering Summer Meeting collocated with the 8th International Conference on Nanochannels, Microchannels, and Minichannels, Montreal, Quebec, Canada, Aug 1–5, 2010, vol. 1, pp. 295-304.

[100] S. Abishek, R. Mead-Hunter, A.J.C. King, B.J. Mullins, "Capture and re-entrainment of microdroplets on fibers," Phys. Rev. E, vol. 100, pp. 042803, 2019.

[101] K. Raju, D.-H. Yoon, "Sintering additives for SiC based on the reactivity: a review," Ceram. Int., vol. 42, pp. 17947-17962, 2016.

[102] J.-H. Eom, Y.-W. Kim, S. Raju, "Processing and properties of macroporous silicon carbide ceramics: a review," J. Asian Ceram. Soc., vol. 1, pp. 220–242, 2013.

[103] Goldlucke GmbH. PORE!SCAN SYSTEMS Furth, Germany, viewed 22 June 2020, https://www.giib.de/en/products-services. n.d.

[104] O. V. Tereshchenko, F. J. K. Buesink, and F. B. J. Leferink, "An overview of the techniques for measuring the dielectric properties of materials," in 2011 30th URSI General Assembly and Scientific Symposium, 2011, pp. 1–4.

[105] L. F. Chen, C. K. Ong, C. P. Neo, V. V. Varadan, and V. K. Varadan, Microwave Electronics measurement and materials characterization, Chichester, England: John Wiley & Sons Ltd., 2004.

[106] S. Soldatov, T. Kayser, G. Link, T. Seitz, S. Layer, and J. Jelonnek, "Microwave cavity perturbation technique for high-temperature dielectric measurements," in IEEE MTTS International Microwave Symposium, 2013, pp. 1–4.

[107] S. Varadan, G. Pan, Z. Zhao, and T. Alford, "As-doped Si's complex permittivity and its effects on heating curve at 2.45 GHz frequency," in Joint Conference of the IEEE International Frequency Control Symposium & the European Frequency and Time Forum, 2015, pp. 111–116.

[108] Y. Taki, M. Kitiwan, H. Katsui, and T. Goto, "Electrical and thermal properties of off-stoichiometric SiC prepared by spark plasma sintering," J. Asian Ceram. Soc., vol. 6, pp. 95–101, 2018.

[109] R. A. Buerschaper, "Thermal and electrical conductivity of graphite and carbon at low temperatures," J. Appl. Phys., vol. 15, pp. 452–454, 1944.

[110] P. Sarafis and A. G. Nassiopoulou, "Dielectric properties of porous silicon for use as a substrate for the on-chip integration of millimeter-wave devices in the frequency range 140 to 210 GHz," Nanoscale Res. Lett., vol. 9, p. 418, 2014.

[111] R. G. Geyer, Dielectric characterization and reference materials, 1st ed. Washington: U.S. Dept. of Commerce, National Institute of Standards and Technology, 1990.

[112] J. Fayos-Fernandez, I. Pérez-Conesa, J. Monzó-Cabrera, S. Del Pino-De León, and J. Carlos Albaladejo-González, "Temperature-dependent complex permittivity of several electromagnetic susceptors at 2.45 GHz," AMPERE Newsl., vol. 1, 2018.

[113] I. Zivkovic and A. Murk, "Characterization of open cell SiC foam material," Prog. Electromagn. Res. B, vol. 38, pp. 225–239, 2012.

[114] Y. Takeuchi, T. Abe, T. Kageyama, H. Sakai, "RF dielectric properties of SIC ceramics and their application to design of HOM absorbers," in Proceedings of the 2005 Particle Accelerator Conference, Knoxville, TN, USA, 2005, pp. 1195-1197.

[115] D.C. Dube, "Study of Landau-Lifshitz-Looyenga's formula for dielectric correlation between powder and bulk," J. Phys. D Appl. Phys., vol. 3, pp. 1648, 1970.

[116] G. Bánhegyi, "Comparison of electrical mixture rules for composites," Colloid Polym. Sci., vol. 264, pp. 1030–1050, 1986.

[117] P. Cignoni, M. Callieri, M. Corsini, M. Dellepiane, F. Ganovelli, G. Ranzuglia, "MeshLab: an open-source mesh processing tool," in Sixth Eurographics Italian Chapter Conference, 2008, pp. 129–136.

[118]   J. Schindelin, I. Arganda-Carreras, E. Frise, V. Kaynig, M. Longair, T. Pietzsch, S. Preibisch, C. Rueden, S. Saalfeld, B. Schmid, J.-Y. Tinevez, D.J. White, V. Hartenstein, K. Eliceiri, P. Tomancak, A. Cardona, "Fiji: an open-source platform for biological-image analysis," Nat. Methods, vol. 9, pp. 676–682, 2012.

[119]   J. Ollion, J. Cochennec, F. Loll, C. Escudé, T. Boudier, "TANGO: A generic tool for high-throughput 3D image analysis for studying nuclear organization," Bioinformatics, vol. 29, pp. 1840-141, 2013.

[120]   W. Dougherty, Robert & Kunzelmann, Karl-Heinz, "Computing local thickness of 3D structures with ImageJ," Microscopy and Microanalysis, vol. 13, pp. 1678-1679, 2007.

[121]   M. Atiyah, P. Sutcliffe, "Polyhedra in physics, chemistry and geometry," Milan j. math., vol. 71, pp. 33–58, 2003.

[122]   A.B. Numna, M.S. Sharawi, "Extraction of material parameters for metamaterials using a full-wave simulator," IEEE Antennas Propag. Mag., vol. 55, pp. 202-211, 2013.

[123]   J. Baker-Jarvis, M. Janezic, B. Riddle, R. Johnk, C. Holloway, R. Geyer, C. Grosvenor, "Measuring the permittivity and permeability of lossy materials: solids, liquids, metals, and negative-index materials," 1st ed., National Institute of Standards and Technology, Technology Administration, U.S. Department of Commerce, NIST: Boulder, CO, USA, 2005, pp. 1–160.

[124]   E.S. Martínez, R.D. Calleja, and W. Gunßer, "Complex polarizability as used to analyze dielectric relaxation measurements," Colloid. Polym. Sci., vol. 270, pp. 146-153, 1992.

[125]   J.N.C. Hernandez, G. Link, S. Soldatov, A. Füssel, M. Schubert, and U. Hampel, "Experimental and numerical analysis of the complex permittivity of open-cell ceramic foams," Ceram. Int., vol. 46, pp. 26829-26840, 2020.

[126]   W. Westphal and A. Sils, "Dielectric constant and loss data," MIT Technical Report AFML TR 72, Wright Patterson, Dayton, OH, USA, vol. 39, pp. 1-71, 1972.

[127]   M.A. Camerucci, G. Urretavizcaya, M. Castro, and A. Cavalieri, "Electrical properties and thermal expansion of cordierite and cordierite-mullite materials," J. Eur. Ceram. Soc., vol. 21, pp. 2917-2923, 2001.

[128]   P. Ratanadecho, K. Aoki, and M. Akahori, "The characteristics of microwave melting of frozen packed beds using a rectangular waveguide," IEEE Trans. Microw. Theory Tech., vol. 50, pp. 1495-1502, 2002.

[129]   X. He, J. Zhou, L. Jin, X. Long, H. Wu, L. Xu, Y. Gong, and W. Zhou, "Improved dielectric properties of thermoplastic polyurethane elastomer filled with core–shell structured PDA/TiC particles," Materials, vol. 13, p. 3341, 2020.

[130]   L.W. McKeen, "Chapter 1—Introduction to plastics and polymers," in Plastics Design Library, Film Properties of Plastics and Elastomers, 3rd ed., Norwich, NY, USA: William Andrew Publishing, 2012, pp. 1-18. ISBN 9781455725519.

[131]   L.M. Schwartz, N. Martys, D.P. Bentz, E.J. Garboczi, and S. Torquato, "Cross-property relations and permeability estimation in model porous media," Phys. Rev. E, vol. 6, pp. 4584-4591, 1993.

[132]   M. Kachanov and I. Sevostianov, "Chapter 6. Connections between elastic and conductive properties of heterogeneous materials," in Micromechanics of Materials, with Applications, 1st ed., J.R. Barber and A. Klarbring, Eds. Cham, Switzerland: Springer International Publishing, 2018, vol. 249, pp. 469-548.

[133]   P. Pietrak and T.S. Wisniewski, "A review of models for effective thermal conductivity of composite materials," J. Power Technol., vol. 95, pp. 14-24, 2014.

[134] V.V. Calmidi and R.L. Mahajan, "The effective thermal conductivity of high porosity fibrous metal foams," J. Heat Transfer, vol. 121, pp. 466-471, 1999.

[135] M. Bracconi, M. Ambrosetti, M. Maestri, G. Groppi, and E. Tronconi, "A fundamental analysis of the influence of the geometrical properties on the effective thermal conductivity of open-cell foams," Chem. Eng. Process.-Process Intensif., vol. 129, pp. 181-189, 2018.

[136] Z. Dai, K. Nawaz, Y. G. Park, J. Bock, and A. M. Jacobi, "Correcting and extending the Boomsma–Poulikakos effective thermal conductivity model for three-dimensional fluid-saturated metal foams," Int. Commun. Heat Mass Transf., vol. 37, pp. 575-580, 2010.

[137] Y. Yao, H. Wu, and Z. Liu, "A new prediction model for the effective thermal conductivity of high porosity open-cell metal foams," Int. J. Therm. Sci., vol. 97, pp. 56-67, 2015.

[138] E. Solórzano, J. Reglero Ruiz, M. Rodríguez-Pérez, D. Lehmhus, M. Wichmann, and J. A. De Saja, "An experimental study on the thermal conductivity of aluminium foams by using the transient plane source method," Int. J. Heat Mass Transf., vol. 51, pp. 6259-6267, 2008.

[139] M. Iasiello, C. Savarese, P. Damian, N. Bianco, A. Andreozzi, W. Chiu, and V. Naso, "Modeling heat conduction in open-cell metal foams by means of the three-dimensional thermal fin theory," J. Phys. Conf. Ser., vol. 1224, p. 12009, 2019.

[140] B. Dietrich, G. Schell, E. C. Bucharsky, R. Oberacker, M. J. Hoffmann, W. Schabel, M. Kind, and H. Martin, "Determination of the thermal properties of ceramic sponges," Int. J. Heat Mass Transf., vol. 53, pp. 198-205, 2010.

[141] A. Bhattacharya, V. Calmidi, and R. L. Mahajan, "Thermophysical properties of high porosity metal foams," Int. J. Heat Mass Transf., vol. 45, pp. 1017-1031, 2002.

[142] A. August, A. Reiter, A. Kneer, M. Selzer, and B. Nestler, "Effective thermal conductivity of composite materials based on open cell foams," Heat Mass Transf. Res. J., vol. 2, pp. 33-45, 2018.

[143] M. S. Phanikumar and R. L. Mahajan, "Non-Darcy natural convection in high porosity metal foams," Int. J. Heat Mass Transf., vol. 45, pp. 3781-3793, 2002.

[144] J. W. Paek, B. H. Kang, S. Y. Kim, and J. M. Hyun, "Effective thermal conductivity and permeability of aluminum foam materials," Int. J. Thermophys, vol. 21, pp. 453-464, 2000.

[145] K. Boomsma and D. Poulikakos, "On the effective thermal conductivity of a three-dimensionally structured fluid-saturated metal foam," Int. J. Heat Mass Transf., vol. 44, pp. 827–836, 2001.

[146] E. Schmierer and A. Razani, "Self-consistent open-celled metal foam model for thermal applications," J. Heat Transf., vol. 128, pp. 194–203, 2006.

[147] E. Sadeghi, S. Hsieh, and M. Bahrami, "Thermal conductivity and contact resistance of metal foams," J. Phys. D. Appl. Phys., vol. 44, p. 125406, 2011.

[148] X. Xiao, P. Zhang, and M. Li, "Effective thermal conductivity of open-cell metal foams impregnated with pure paraffin for latent heat storage," Int. J. Therm. Sci., vol. 81, pp. 94–105, 2014.

[149] R. Coquard, D. Rochais, and D. Baillis, "Experimental investigations of the coupled conductive and radiative heat transfer in metallic/ceramic foams," Int. J. Heat Mass Transf., vol. 52, pp. 4907–4918, 2009.

[150] X. Xiao, P. Zhang, and M. Li, "Preparation and thermal characterization of paraffin/metal foam composite phase change material," Appl. Energy, vol. 112, pp. 1357–1366, 2013.

[151] R. Coquard, M. Loretz, and D. Baillis, "Conductive heat transfer in metallic/ceramic open-cell foams," Adv. Eng. Mater., vol. 10, pp. 323–337, 2008.

[152] A. August et al., "Prediction of heat conduction in open-cell foams via the diffuse interface representation of the phase-field method," Int. J. Heat Mass Transf., vol. 84, pp. 800–808, 2015.

[153] V. Raizer, "Microwave emission of the ocean," in Advances in Passive Microwave Remote Sensing of Oceans, 1st ed., CRC Press Taylor & Francis Group, Boca Raton, FL, USA, 2017, vol. 1, pp. 120–122.

[154] A. Ellison, "Permittivity of pure water, at standard atmospheric pressure, over the frequency range 0–25 THz and the temperature range 0–100 °C," J. Phys. Chem. Ref. Data, vol. 36, pp. 1–18, 2007.

[155] A. D. Chistyakov, "The Permittivity of water and water vapor in saturation states," Russ. J. Phys. Chem. A, vol. 81, pp. 5–8, 2005.

[156] D.P. Fernández, A.R.H. Goodwin, E.W. Lemmon, J.M.H. Levelt Sengers, and R.C. Williams, "A formulation for the static permittivity of water and steam at temperatures from 238 K to 873 K at pressures up to 1200 MPa, Including Derivatives and Debye–Hückel Coefficients," J. Phys. Chem. Ref. Data, vol. 26, pp. 1125-1166, 1997.

[157] J. Qian, Q. Gu, H. Yao, and W. Zeng, "Dielectric properties of wet steam based on a double relaxation time model," Eur. Phys. J., vol. 42, p. 22, 2019.

[158] J. Zhao, M. Sun, L. Zhang, C. Hu, D. Tang, L. Yang, and Y. Song, "Forced convection heat transfer in porous structure: effect of morphology on pressure drop and heat transfer coefficient," J. Therm. Sci., vol. 30, pp. 363-393, 2021.

[159] B. Dietrich, "Heat transfer coefficients for solid ceramic sponges—experimental results and correlation," Int. J. Heat Mass Transf., vol. 61, pp. 627-637, 2013.

[160] Y. Mahmoudi, K. Hooman, and K. Vafai, Convective heat transfer in porous media, 1st ed.; CRC Press: Boca Raton, FL, USA, 2020; pp. 37–52.

[161] R. Stam, "Comparison of international policies on electromagnetic fields (power frequency and radio frequency fields)," National Institute for Public Health and the Environment, Bilthoven, The Netherlands, 2011.

[162] E. Sili and J. Cambronne, "A new empirical expression of the breakdown voltage for combined variations of temperature and pressure," Int. J. Aerosp. Eng., vol. 6, pp. 611-616, 2012.

List of figures

List of tables

Appendix A

A.1. Microwave applicator technical drawing

Pos.	Menge	Benennung	Bemerkung	Bauteilnummer
1	1	Mikrowellenkanal		A29_02.00
2	1	Quarzglas	Dim. 56,3/65,0 - L=95	A29_05
3	2	O-Ring_65x3		A29_Norm_O-Ring1
4	2	Glasfixierflansch		A29_03.00
5	2	Abstandshalter_PTFE	Rund Dim. 56,0 x 17,5 - PTFE	A29_06
6	2	O-Ring_56,5x4		A29_07_O-Sonderring
7	8	Innensechskantschraube ISO 4762 - M6 x 40		A29_Norm_Schraube1
8	2	LDA-Fenster		A29_04.00
9	16	Unterlegscheibe DIN 125 - A 6,4		A29_Norm_U-Scheibe1
10	1	SiSiC-Schaum	Dim. 54,3 x 70,0 mm	A29_08
11	4	O-Ring_70x3		A29_Norm_O-Ring2
12	16	Innensechskantschraube ISO 4762 - M6 x 25		A29_Norm_Schraube2
13	1	Innensechskantschraube		ISO 4762 - M6 x 35
17	1	Lochblende		A29_10
18	2	Einlaufstrecke_DN50		A29_06.00
22	1			A29_10.00_Einspeisesystem
23	1			A29_11.00_Abflußsystem
25	4	O-Ring_70x3		A29_Norm_O-Ring3
26	1	LDA-Fenster		A29_04.00a_LDA-Fenster2_DN50
27	1	Sechskantmutter		ISO 4032 - M6

Detail B (1 : 2)

A-A (1 : 10)

Pos.	Menge	Benennung	Bemerkung	Bauteil-Nr.
1	1	Kanal		A29_02.01
2	2	Diffusor		A29_02.02.00
3	2	Mikrowellenflansch_WR340		A29_02.04
4	2	Blockflansch		A29_02.05
5	4	Rohreinsatz		A29_02.06

E-E (1 : 2)

Ø90

G-G (1 : 2)

F-F (1 : 2)

Heiko Pietruske, +49 (351) 260 - 3226, h.pietruske@hzdr.de

Anzahl: 1 Stück

	Zul. Abw.	Oberfläche	Werkstoff, Halbzeug:	Gesamtgewicht: 0 kg
	ISO 2768 - m	Maßstab: 1:2	siehe Stückliste	
	ISO 13920 - B			
	ISO 13920 - F			

	Datum	Name
Bear.	13.02.2020	H. Pietruske
Gepr.		

Datei: A29_00_Adriana.idw

Institut für Fluiddynamik

Abteilung Experimentelle Thermofluiddynamik

Benennung: ADRIANA

Zeichnungsnummer: A29_00

Ers. für: Ers. durch:

Zust.	Änderung	Datum	Nam.	Ursprung:

Blatt: 2 /3a
A3

Scientific Publications and Contributions

During the time as a researcher at the Helmholtz-Zentrum Dresden-Rossendorf, the following scientific and supervisory contributions were made.

B1 Peer-reviewed publications

J. N. Camacho Hernandez, G. Lecrivain, M. Schubert, and U. Hampel, "Droplet retention time and pressure drop in SiSiC open-cell foams used as droplet separation devices: a numerical approach," Ind. Eng. Chem. Res., vol. 59, pp. 4093-4107, 2019.

J. N. Camacho Hernandez, G. Link, S. Soldatov, A. Füssel, M. Schubert, and U. Hampel, "Experimental and numerical analysis of the complex permittivity of open-cell ceramic foams," Ceram. Int., vol. 46, pp. 26829-26840, 2020.

J. N. Camacho Hernandez, G. Link, M. Schubert, and U. Hampel, "Modeling of the effective permittivity of open-cell ceramic foams inspired by platonic solids," Materials, vol. 14, pp. 7446, 2021.

J. N. Camacho Hernandez, G. Link, M. Schubert, and U. Hampel, "Novel mixing relations for determining the effective thermal conductivity of open-cell foams," Materials, vol. 15, pp. 2168, 2022.

J. N. Camacho Hernandez, G. Link, M. Schubert, and U. Hampel, "Experimental study of a compact microwave applicator for evaporation of airflow-entrained droplets," Materials, vol. 15, pp. 6765, 2022.

The information provided in the above articles are partially reused/adapted in this thesis with prior permission from the respective publishers.

B2 Oral presentations

J. N. Camacho Hernandez, G. Link, "Microwave dielectric properties of open-cell solid foams based on silicon carbide ceramics" 17th International Conference on Microwave and High-Frequency Heating (AMPERE 2019), 9-12 September 2019, Valencia (Spain).

B3 Poster presentations

J. N. Camacho Hernandez, M. Schubert, and U. Hampel, "Numerical Simulations of the Pore-Scale Flow in Ceramic Open-Cell Foams," Proceedings of the 4th World Congress on Momentum, Heat and Mass Transfer (MHMT'19), ICMFHT 124-1, 10–12 April 2019, Rome (Italy).

B4 Data availability

Journal publication and supplementary data are provided with proper indexing in the RODARE repository. All these data are intended for non-commercial use only.

Selbständigkeitserklärung

Hiermit versichere ich an Eides statt, die vorliegende Arbeit selbstständig, ohne fremde Hilfe und ohne Benutzung anderer als der von mir angegebenen Quellen angefertigt zu haben. Alle aus fremden Quellen direkt oder indirekt übernommenen Gedanken sind als solche gekennzeichnet.

Die Arbeit wurde noch keiner Prüfungsbehörde in gleicher oder ähnlicher Form vorgelegt.

Jesus Nain Camacho Hernandez   Dresden, den 04.07.2023